CHARACTERIZATION OF FLUIDS AND THERMAL PERFORMANCE OF TAB-INDUCED COUNTER-ROTATING VORTEX PAIRS ON SURFACE COOLING

A Dissertation

by

JEONGMOON PARK

Submitted to the Office of Graduate and Professional Studies of
Texas A&M University
in partial fulfillment of the requirements for the degree of

DOCTOR OF PHILOSOPHY

Chair of Committee,	Jorge L. Alvarado
Co-Chair of Committee,	Sai C. Lau
Committee Members,	Michael Pate
	Edward White
Head of Department,	Andreas A. Polycarpou

August 2018

Major Subject: Mechanical Engineering

ABSTRACT

Characterization of the flow field generated by vortex generators (VGs) has been a matter of intense research in a host of applications ranging from aerodynamic efficiency to mixing for heat transfer. Recently, trapezoidal VGs have considered due to the distinctive coherent flow structure induced in the wake of VGs. In the present study, experimental investigations were carried out to study the effects of geometric factors and configuration of the trapezoidal VGs on flow dynamics and heat transfer when using air as heat transfer fluid.

The flow structures induced by trapezoidal VGs and their effects on heat transfer were characterized using smoke visualization, particle image velocimetry (PIV), and infrared (IR) thermography, respectively. Experiments were performed in a region where the counter-rotating vortex pair (CVP) was dominant in the wake of VGs. For single VG, taper angle and inclination angle of VG were varied to understand their role on flow and heat transfer characteristics. For multiple VGs, a spacing-to-width ratio (STW) of VGs, streamwise spacing between rows of VGs (S), and streamwise spacing between clusters of VGs (B) were varied to understand the role of those configuration factors on flow and heat transfer characteristics. Results reveal that the geometric factors of VGs have a distinct effect on the coherent flow and local convective heat transfer phenomena. Furthermore, specific values of configuration factors of multiple VGs are also suggested for better heat transfer. The PIV and heat transfer experiments indicate that convective heat transfer on the surface is greatly influenced by the mean velocities of the flow when CVPs are coherent. However, as CVPs become less coherent, fluctuations in the flow play a more important role in the heat transfer process. In summary, the coherent flows induced by single and multiple trapezoidal VGs were characterized and their effects on heat transfer were explored and elucidated.

DEDICATION

To Dr. Jorge L. Alvarado for his inspiration and support

To my family for their unconditional love

ACKNOWLEDGEMENTS

First and foremost, I praise and thank Jesus Christ for his guidance and giving me the best at all times. With the faith I have in Jesus, my personal responsibility through the faith journey is to seek His will in which I stand.

I would like to thank my wife, Yunyoung Kang, for her support, sacrifice and love. I also thank my parents and parents-in-law for strong supports and all the prayers for me and my family.

I would like to thank my chair advisory committee, Dr. Jorge L. Alvarado for his patience and continual help and advice. I thank him for giving me this great opportunity to work on this research project. I also thank my co-chair advisory committee, Dr. Sai C. Lau, and my advisory committee members, Dr. Michael Pate and Dr. Edward White for their guidance and support throughout the course of this research. I would like to thank Dr. Leonardo P. Chamorro of the Department of Mechanical Sciences and Engineering at the University of Illinois Urbana-Champaign for all his comments on Fluid dynamics in this research.

CONTRIBUTORS AND FUNDING SOURCES

Contributors

This work was supervised by a dissertation committee consisting of Professor Jorge L. Alvarado [advisor], Professor Sai C. Lau, and Professor Michael Pate of the Department of Mechanical Engineering and Professor Edward White of the Department of Aerospace Engineering.

Dr. Charles P. Marsh at U.S. Army Construction Engineering Research Laboratory (CERL) served as a project leader. Advice in the fluid dynamics area was provided by Professor Leonardo P. Chamorro of the Department of Mechanical Sciences and Engineering at the University of Illinois Urbana-Champaign.

All other work conducted for the dissertation was completed by the student independently.

Funding Sources

This work was supported by the U.S. Army Corps of Engineers, Engineer Research and Development Center, under U.S. Army Research, Development, Test, and Evaluation Program Element T23, Basic Research/Military Construction, contract No. W9132T-14-2-0022, Experimental Characterization of Multiscale Vortical Flow Structure.

.

NOMENCLATURE

a	Vertical coordinate of vortex core
AR	Aspect ratio of vortex generator $\left(l/c\right)$
b	Horizontal coordinate of vortex core
B	Streamwise spacing of clusters of vortex generators
c	Chord length of vortex generator
CVP	Counter-rotating vortex pair
D	Distance of counter-rotating vortex pairs in the inviscid potential model
D_h	Hydraulic diameter
f	Lens focal length
F	Complex potential function
h	Heat transfer coefficient
H	Spanwise spacing of vortex generators
k	Thermal conductivity
l	Base width of vortex generator
l_{50}	Width of vortex generator at 50% of chord
Nu	Nusselt number based on hydraulic diameter $\left(\frac{h_0 D_h}{k}\right)$
q''	Heat flux
Re	Reynolds number based on the hydraulic diameter $\left(\rho U D_h/\mu\right)$
s	Complex coordinate of vortex core $\left(b/2 + a\right)$
S	Streamwise spacing of rows of vortex generators
u	Streamwise velocity $(U + u')$

u_h	Free stream velocity at the trailing edge of vortex generator
u_{rms}	Root-mean-square of streamwise velocity fluctuation
u_τ	Friction velocity $\left(\sqrt{\tau_w/\rho}\right)$
u'	Streamwise velocity fluctuation
$-\overline{u'v'}$	Primary Reynolds stress
u^+	Axial coordinate scaled with u_τ
STW	Spacing-to-width ratio of VGs in a single row
T_b	Bulk fluid temperature
T_w	Surface temperature with vortex generator
T_{w0}	Surface temperature without vortex generator
T_{in}	Fluid temperature at the entrance of the test section
T_{out}	Fluid temperature at the exit of the test section
U	Time-averaged streamwise velocity
U_0	Time-averaged streamwise velocity of free stream at the center of the duct
v	Vertical velocity $(V + v')$
v_{rms}	Root-mean-square of vertical velocity fluctuation
v'	Vertical velocity fluctuation
V	Time-averaged vertical velocity
VF	Radiation view factor
VG	Vortex generator
w	Uncertainty quantity
W	Complex velocity of potential function F

y^+	y coordinate scaled with u_τ and ν $\left(y^+ = \frac{yu_\tau}{\nu}\right)$
α	Heater length
β	Height of vortex generator
ρ	Density of fluid
μ	Dynamics viscosity of fluid
ν	Kinematic viscosity of fluid
ψ	Scaling magnification factor in PIV calibration
ε	Emissivity
θ	inclination angle of vortex generator
ϕ	Taper angle of vortex generator
Γ	vortex circulation
ζ	Dimensionless vertical coordinate of vortex core $\left({}^{2\pi a}/_{D}\right)$
ξ	Dimensionless horizontal coordinate of vortex core $\left({}^{2\pi b}/_{D}\right)$
δ	Dimensionless axial coordinate of vortex core $\left({}^{2\pi x}/_{D}\right)$
$\dot{\gamma}_w$	Local wall shear rate with vortex generator
$\dot{\gamma}_{w0}$	Local wall shear rate without vortex generator
λ	Local shear rate ratio $\left({}^{\dot{\gamma}_w}/_{\dot{\gamma}_{w_0}}\right)$
τ_w	Wall shear stress $\left(\mu \frac{\partial U}{\partial y}\Big\vert_w\right)$
ω	Vorticity
ω_i	Streamwise vorticity $\left(\frac{\partial W}{\partial y} - \frac{\partial V}{\partial z}\right)$

TABLE OF CONTENTS

Page

Page

LIST OF FIGURES

LIST OF TABLES

CHAPTER I

INTRODUCTION

Large amounts of heat are released in power generating or refrigeration systems in chemical and power plant cycles, internal combustion engines, computers and electronic systems. Water-cooled (or wet-cooling) heat transfer method has been used in numerous thermal management and power generation systems due to their excellent heat transfer capability of water either as heat transfer fluid or evaporating medium. Wherever there is an adequate supply of water, the use of water as cooling medium has been considered as the easiest and least expensive cooling method. However, in an era when water resource challenges and scarcity have come to the forefront, there have been numerous efforts to develop alternative cooling techniques to replace water-cooled methods. The development of alternative technologies is not only due to the dwindling supplies of water but also due to the environmental considerations, such as particulate matter pollution (PM_{10} and $PM_{2.5}$) involved when water is used as medium [1].

Air-cooled (or dry-cooling) method has the potential to lead to significant savings of water usage by employing air as cooling medium. However, air-cooled methods exhibit poor thermal efficiency inherently due to the low specific heat and density of air. Therefore, numerous techniques have been developed to improve mixing and heat transfer characteristics of air-cooled systems. Especially, passive methods have attracted more attention than active methods in heat exchanger applications [2] due to their low operating cost. Passive methods drive heat transfer enhancement naturally by using special structural configurations. On the other hand, active methods tend to be more expensive and cumbersome because of the increased manufacturing and operating costs and potential operating problems associated with any active approach.

One of the common passive methods with low pressure drop characteristics is the use of vortex generators (VGs) [3, 4]. Vortex generators can be easily incorporated inside compact channels or into pipes of heat exchangers and their self-induced vortical structures can enhance mixing and heat transfer in a host of applications [2, 5-7]. Therefore, a well-designed air-cooled system consisting of VGs can have a significant positive impact on saving water and energy as well as company profitability.

1.1 Motivation

Most of disadvantages of air-cooled systems, such as cooling towers, entail large structures including large fans to meet a required heat transfer duty [1]. Such systems also generate noise and demand greater energy as part of the cooling systems, which stem from their low thermal efficiency [1]. Therefore, the present work is motivated by the need to make air-cooled heat exchangers more efficient.

One effective way to enhance the convective heat transfer process is the use of vortex generators (VGs). The most frequently used VGs for the aerodynamics and heat transfer applications are the winglet-type and wing-type with rectangular or delta (triangular) shapes. Those VGs generates longitudinal vortices and destabilize the flow field, thereby enhancing turbulence mixing and heat transfer [2, 8, 9]. In recent years, a trapezoidal VG (wing type) has been introduced, which generates a counter-rotating vortex pair (CVP) and also a sequence of periodic hairpin vortex structures.

It has been found that the coherent flow structures and heat transfer performances of the VGs highly depend on their unique structural geometries [2, 8-11]. However, only few articles have investigated about the effects of the trapezoidal VGs on fluid dynamics and heat transfer.

Moreover, little is known about how the structural parameters of VGs including taper angle and inclination angle affect fluid dynamics and heat transfer. In addition, none of the studies has considered the effects of spacing when multiple trapezoidal VGs are employed. Therefore, the effects of single and multiple VGs on fluid dynamics and heat transfer have to be studied to develop more efficient air-cooled heat exchangers.

1.2 Objectives

The objectives of this study are to understand the fluid dynamics and heat transfer characteristics of the coherent flow induced by trapezoidal VGs, when using air as heat transfer fluid. To fulfil these objectives, numerous experimental activities were conducted for the single trapezoidal VG cases with different geometries as well as multiple trapezoidal VGs cases with different configurations.

In the study of single VGs, the effects of taper angle and inclination angle of the trapezoidal VGs on flow structure, velocity and surface temperature distribution were characterized by using smoke visualization, particle image velocimetry (PIV) and infrared (IR) camera thermography. In the study of multiple VGs, the effects of the streamwise and spanwise spacings of the trapezoidal VGs on fluid dynamics and heat transfer were studied. In addition, the streamwise spacing of clusters of VGs were varied to optimize the configuration of the trapezoidal VG system as heat transfer system.

In summary, this study attempts to increase the overall understanding of the coherent flows induced by single and multiple trapezoidal VGs and their effects on heat transfer. This study can be applied in industry in the design, development and implementation of the next generation of heat and mass transfer systems using air as cooling medium.

1.3 Overview

This dissertation has six chapters. Chapter II presents a review of literature survey in the field of experimental and numerical work on fluid dynamics and heat transfer of vortex generator systems. Identification of knowledge gaps in the present literature is also discussed in Chapter II. Chapter III describes the experimental setup and techniques used in this work. Chapter IV includes the experimental results. Chapter IV also explains about the relationship between fluid dynamics and heat transfer. Chapter V includes all the concluding remarks and recommendations for potential new studies.

CHAPTER II

LITERATURE REVIEW

Active and passive methods have been developed to enhance the performance of heat transfer systems. In heat exchanger applications, the passive methods are more frequently used than the active methods [2], such as the use of the vortex generators (VGs). Therefore, different geometries and configurations of VGs have been proposed and examined to understand flow structures in the wake and their corresponding effects on heat transfer.

2.1 Literature Review of a Longitudinal Vortex Induced by a Vortex Generator

The basic objectives of the use of any VG are the creation of a longitudinal vortex and flow destabilization [8]. A longitudinal vortex is generated by the pressure difference between the windward and leeward regions of the VG, having its axis along the streamwise direction. The longitudinal vortex improves the convective process by entraining the high-momentum fluid in the free stream toward the wall and ejecting the low-momentum fluid to the freestream [2, 8, 9, 12, 13]. In addition, it induces inflection points in the velocity profiles, which is necessary condition for flow destabilization. The instability also leads to local turbulence behavior, which reduces the critical Reynolds number for the on-set of turbulence and in turn contributes to global heat and mass transfer in the downstream region [8, 14].

It has been found that the up-flow region and the down-flow region of the longitudinal vortex contribute to the overall convective thermal transport mechanism near the wall [8]. However, the streamwise velocity is accelerated in the down-flow region, resulting in enhanced thermal transport [8, 13]. Therefore, better convective heat transfer occurs in the down-flow region of the vortex. This has been observed in many studies. For instance, Eibeck and Eton [10]

investigated the characteristics of a longitudinal vortex induced by a single delta winglet VG in turbulent flow ($1026 < Re_\theta < 3654$, Re_θ based on momentum thickness). They observed the increase of boundary-layer thickness on the up-flow side of the vortex. On the other hand, on the down-flow side of the vortex, the boundary layer thickness decreased to less than half of the value associated with the undisturbed flow (no VG) case. In their heat transfer results, the maximum increase of local heat transfer was 25% and it occurred in the down-flow region, where the boundary layer thickness was at its minimum. They also observed a decrease of local heat transfer in the up-flow region by as much as 15%.

Torii and Yanagihara [14] also studied the effects of using a single delta winglet VG. Before the onset of transition from laminar to turbulence, they observed high and low heat transfer in the down-flow and the up-flow regions of a longitudinal vortex, respectively. However, after transition to turbulence was achieved, the instability of the coherent flow became larger and the heat transfer coefficient increased when compared to the laminar flow case due to an increase in fluid mixing. At the location of the onset of transition to turbulence, the local heat transfer rate increased by up to 40%.

2.2 Literature Review of Single Pair of Longitudinal Vortices Induced by Vortex Generators

A single pair of longitudinal vortices can be generated by using two winglet-type VGs or a single wing-type VG. Based on the configurations of the VGs, a counter-rotating vortex pair or a co-rotating vortex pair can be generated. Counter-rotating vortices can have either the common-up flow or the common-down flow in between of the vortices depending on the direction of vortex rotation. Depending on the initial spacing, height, and direction of rotation of

the longitudinal vortices, each vortex pair displays a unique path along the downstream direction. The path of the longitudinal vortices can be estimated by using potential flow theory [15-19].

In the co-rotating vortex systems, Pearcey [12] found that the initial spanwise spacing of the vortices had to be greater than 3β (β is the VG height) to keep the vortices energetic in the downstream. For spacings smaller than 3β, the vortices damped out one another and failed to maintain a high velocity field in the downstream region. When the spacing was larger than 3β, the vortices were found to behave independently.

In counter-rotating systems with common-down flow, a vortex pair moves apart along the downstream direction and produces a wide region of boundary layer thinning [12, 20, 21]. Pauley *et al.* [20] and Westphal *et al.* [21] found that the vortices with the common-down flow did not interact strongly with each other but interacted more with the wall. The vortices were completely independent when spanwise spacing between the vortices was larger than 2β [20]. As the spanwise spacing of the VGs was increased, the thickness of the boundary layer between the vortices increased as well [21].

In the counter-rotating systems with common-up flow, the vortices tend to move closer together and lift away from the surface as they develop along the downstream direction [12, 16, 18-20]. However, as vortex pair rises from the surface, its range of effectiveness on boundary layer control and convective heat transfer [12] diminishes. Research findings also reveal that common-up flow vortices interact strongly with each other and weakly with the flow near the wall [20]. Pauley *et al.* [20] observed that the vortices with smaller spacing in between, had stronger interactions with one another. In their study, the vortices remained within the boundary layer and produced a significant boundary layer perturbation when the spanwise spacing was 5β or larger.

Fiebig *et al.* [22] and Tiggelbeck *et al.* [23] studied the effects of counter-rotating vortex pair (CVP) on flow structures and heat transfer for laminar flow ($1000 < Re < 2000$, with Re based on the channel height) and turbulent flow ($2000 < Re < 9000$, with Re based on the hydraulic diameter), respectively. Experiments were conducted for a delta wing VG, a rectangular wing VG, a delta winglet VG pair, and a rectangular winglet VG pair in both studies. Fiebig *et al.* [22] found that the cross-sections of the longitudinal vortices generated by the wing-type VGs were elliptical, but those by winglet-type VGs were circular. The wing-type VGs produced more stable longitudinal vortices than the winglet-type VGs. In the heat transfer results from both studies [22, 23], delta (triangular) shape VGs were more effective on heat transfer enhancement than rectangular shape VGs. Although rectangular VGs led to lower heat transfer enhancement, their effects varied widely along the spanwise direction. For laminar flow [22], delta wing VG was the most effective from the heat transfer point of view. On the other hand, for turbulent flow [23], delta winglet VG was the most effective in terms of heat transfer. In general, heat transfer was enhanced or increased with angle of attack and Reynolds number [22, 23].

Liou *et al.* [24] studied the effects of vortex generators on local Nusselt number distribution with 12 different VG configurations in a square channel under turbulent flow ($Re = 12000$, with Re based on the hydraulic diameter). The 12 vortex generators included ribs, V-shaped ribs, delta wing VGs, and delta winglet VGs with different topologies. They found that a 45° V-shaped rib led to greater heat transfer among the 12 test samples with a maximum heat transfer enhancement of 270%. However, the friction loss could be as high as 280%. A delta wing VG led to the second highest heat transfer enhancement (170%) but with 30% increase in friction loss. They also observed that the vertical velocity distribution of the flow were most consistent with the local Nusselt number (Nu/Nu_0) distribution, with the highest and lowest

Nu/Nu_0 values in the down-flow and up-flow regions, respectively. In addition, their results showed that turbulent kinetic energy was less related with the local Nusselt number distribution.

2.3 Literature Review of Single Trapezoidal Vortex Generators

Recently many researchers have considered the use of trapezoidal vortex generators (wing-type) due to their ability to induce distinctive vortical structures. Unlike the conventional VGs, the trapezoidal VGs face downstream and generate a counter-rotating vortex pair (CVP) with the common-up flow located in between the two vortices. CVP also leads to the formation of periodic hairpin vortex structures [18, 19, 25-30]. In the near wake of the VG, the flow is dominated by the CVP ($x/\beta < 1.5 - 2$, β is the VG height) [18, 19, 25-27]. In the further downstream region, the CVP breaks down and the flow is dominated by hairpin vortices ($2 < x/\beta < 10$) [25-27].

Counter-rotating vortices originate from the two sides of the VG due to the pressure difference between the windward and leeward regions of the VG [25-28]. For the hairpin vortices, the shear layer separates at the trailing edge of the trapezoidal VG, which becomes unstable downstream (i.e. onset of Kelvin-Helmholtz instability). The shear flow rolls up into a vortex and evolves into a hairpin-like structure in the downstream region [27, 32]. The CVP and hairpin structures may lead to efficient transport of low-momentum fluid near the surface to the outer flow, and also entrain the outer flow toward the wall [25-28, 32].

Yang *et al.* [26] and Dong and Meng [27] investigated the vortical structures induced by a single trapezoidal VG. Yang *et al.* [26] conducted planar particle image velocimetry (PIV) and correlated the location of the hairpin vortex heads and hairpin legs with the inflection points in the mean streamwise and spanwise velocity profiles, respectively. Dong and Meng [27]

numerically simulated the coherent flow induced by a trapezoidal VG with the same geometry used in [26] using Direct Numerical Simulation (DNS). They revealed that the CVP in the wake of the VG evolved into hairpin vortex legs through a deformation and splitting process. According to both of the studies [26, 27], the turbulence production and the turbulent kinetic energy were mostly associated with formation of the hairpin vortex heads and hairpin legs.

Hamed *et al.* [30] compared a trapezoidal VG with rectangular, triangular, and ellipsoidal VGs at two different Reynolds numbers under laminar flow and turbulent flow conditions. They performed 2D and 3D particle image velocimetry (PIV) analysis to investigate the coherent flow structure induced by the VGs. They found that the trapezoidal VG generated stronger CVP than the rectangular VG at low Reynolds number even though it has a smaller flow-facing area. However, the trapezoidal and rectangular VGs generated CVP with similar circulation strengths at high Reynolds number. At lower Reynolds number, the CVP lasted longer along the duct and reached greater elevation at steeper inclination angles.

Habchi *et al.* [33] investigated the turbulent field generated by a single perforated trapezoidal VG (Re = 7000 and 42000, with Re based on the VG height). The idea of having a perforation was to introduce the high-velocity fluid into the wake and reduce the recirculation zone behind the trapezoidal VG. Laser doppler velocimetry was used to characterize the flow field in the wake of the VG. They observed a high-momentum fluid flow coming out of the perforation. However, the effect of a perforation became insignificant at the axial distance of $x/\beta > 2$. Furthermore, the sheared flows from the trailing edge and the perforation of the trapezoidal VG led to high turbulent kinetic energy (TKE), which are known to enhance meso-mixing. However, there was no significant effect of the VG on the TKE profile at $x/\beta > 1$. Therefore,

they suggested that rows of VGs should be used with streamwise spacing of $x/\beta = 1$ in order to provide good meso-mixing.

Habchi *et al.* [29] proposed and postulated a quantitative expression capable of relating vorticity flux (Ω) to Nusselt number (Nu), when using a single trapezoidal VG. They numerically simulated the coherent flow induced by a trapezoidal VG using RANS under turbulent flow condition (Re = 12200, with Re based on hydraulic diameter). In general, the conventional turbulence model is known for not being able to predict the Reynolds stress field accurately but can adequately predict the overall development of the flow [34]. The simulation results were compared with the PIV and DNS results in Yang *et al.* [26] and Dong and Meng [27]. They postulated a correlation between cross-area averaged vorticity flux (Ω) and spanwise-averaged Nusselt number (Nu) as follows:

$$\frac{\mathrm{Nu}}{\mathrm{Nu}_0} = \alpha(\Omega - C_1)^{\beta} + C_2 \tag{1}$$

where α, β, C_1 and C_2 are constants, which are obtained by curve fitting their simulation results. However, they concluded that the Nusselt number correlation could not be a single function of vorticity and must take into account other topological characteristics of the vortical structure as well.

Lemenand *et al.* [35] extended the study in [29] and computed vorticity flux (Ω) of the CVP induced by a single trapezoidal VG and determined the associated Nusselt number (Nu) along the duct using RMS-RANS under turbulent flow condition (Re = 2080 with Re based on the VG height). In their study, the vorticity flux (Ω) was cross-area averaged and Nusselt number (Nu) was spanwise-averaged. They observed that the profiles of both Ω and Nu along the axial direction peaked near the tip or edge of the trapezoidal VG. However, vorticity decayed at a much slower rate than Nusselt number along the axial distance. Conversely, Nusselt number

rapidly decreased right after the VG, while the strength of vorticity persisted far downstream from the VG and decayed slowly.

Khanjian *et al.* [36] numerically studied the heat transfer and fluid flow behavior induced by a VG in a parallel plate channel. In the study, the VG with a taper angle of 0° (rectangular) faced downstream under laminar flow condition (Re = 456, with Re based on the VG height). However, the VG inclination angle was varied from 10° to 30° to determine the effect of inclination angle on the heat transfer enhancement. They found that the CVP generated by the VG was more energetic at higher inclination angles. In general, the spanwise-averaged Nusselt number (Nu) increased with inclination angle. However, a maximum enhancement (4.3%) was found at inclination angle of 25°. They concluded that the optimum inclination angle of the VG under the given operating conditions was 25°.

2.4 Literature Review of Multiple Vortex Generators

The path followed by the vortices determines if they remain energetically in the downstream region, which is governed by the configurations of the vortex generators [12]. It has been found that arrays of counter-rotating vortices are more suitable for heat-transfer enhancement than arrays of co-rotating vortices [8, 12, 14, 37, 38]. Therefore, literature and findings on co-rotating vortex systems are not considered in this study.

In the study done by Pearcey [12], it was found that the elevation of the vortices in the counter-rotating vortex system limited their range of effectiveness in terms of boundary layer separation control. Therefore, he suggested a "Bi-plane" system that was essentially a combination of two rows of CVPs. In a nutshell, the first row VGs generated the CVPs with the common-down flow and the second row VGs generated the CVPs with the common-up flow. It

was designed to accelerate and improve mixing within the boundary layer and to keep the vortices adjacent to the surface further downstream. He indicated that the VGs in the second row had to be placed with enough spanwise spacing to allow the vortices from the front row to pass between them or placed far enough downstream to allow the vortices from the front row to pass over the top. If this was not done, the vortices from both rows became weaker as the vortices from the first row begin to interact with the ones from the second row.

A combination of rows of VGs and tubes has been often applied to fin-tube heat exchangers. The configuration of VGs and tubes had to be designed to accelerate the flow by the constricted passage between the tube and VGs (i.e. the venturi effect) [39]. The accelerated flow delays separation from the tube and finally mitigates the zones of poor heat transfer [12, 39, 40]. For instance, Torii *et al.* [39] combined the common-up flow vortex system with round tubes by locating winglet VGs symmetrically behind the tubes. Their system led to heat transfer enhancement of 20% but also increased the pressure loss penalty by 15% for the in-line tube arrangement. In the case of staggered tube arrangement, heat transfer increased by 30% but increased pressure drop by 55%. Fiebig *et al.* [40] used the common-down flow vortex system with round tubes. They observed enhancement in heat transfer of 65% with an increase in the friction factor by 45% for the in-line tube arrangement. The staggered tube arrangement also led to lower heat transfer and lower friction penalty than the in-line arrangement case.

Kaci *et al.* [41] performed a numerical study (RANS) investigating the effects of the coherent flow induced by rows of the trapezoidal VGs on heat transfer in a circular pipe. The VGs were equally arranged at every 90° in the radial direction and every 5β in the streamwise direction. The reasons for the axial and radial spacings of the arrangement were not clear in the study. They indicated that heat transfer was increased mainly by the counter-rotating vortex pairs

(CVPs). Hairpin vortices also increased heat transfer and were responsible for the uniform temperature distribution in the main stream. They obtained about 500% enhancement of heat transfer from the proposed VG configuration. Based on the Colburn factor and friction factor data, they showed that their proposed design had better heat transfer performance when compared to other commercial heat exchangers.

Habchi *et al.* [42] also numerically studied the heat transfer when using multiple trapezoidal VGs in a circular pipe. Seven successive rows of trapezoidal VGs with 12 different configurations were simulated under turbulent flow condition ($7500 < Re < 15000$ with Re based on the hydraulic diameter). They found that the hemispherical protrusions placed between the trapezoidal VG rows greatly enhanced the heat transfer with a small increase in pressure drop. They indicated that protrusions increased the temperature gradients and vorticity close to the heated wall. Based on the results, configurations with combination of inverted trapezoidal VGs and protrusions provided the highest Nusselt number among the tested cases.

2.5 Literature Review of Other Heat Transfer Enhancement Methods in Heat Exchanger Applications

Numerous methods have been developed to enhance mixing and heat transfer performance. The enhancement methods can be classified as active, passive, or compound [2]. Active methods require external power, such as electric or acoustic fields, mechanical devices, or surface vibration, whereas passive methods use a special surface geometry embedded within the system without external power requirement.

Active methods have the advantage of inducing greater or lower heat transfer and pressure drop, depending on fluid velocity. However, when the prime mover in the heating or

cooling system is activated, it inherently generates increased pressure drop. On the other hand, by lowering the fluid velocity, pressure drop reduces but heat transfer rate deteriorates. Most active methods involve increased operating costs, and other issues that are not well understood given the dependence on fluid velocity and heat exchanger configuration [2].

In heat exchanger applications, passive methods have been more frequently used because of their simplicity [2, 43, 44, 45, 46]. For instance, the use of extended surface, such as wavy fins, strip fins, and louvered fins, have widely been studied and used in heat exchangers. Those structures provide greater effective surface area for heat transfer as well as a decrease in the volume of the system due to an increase in thermal conduction and a better convection process [45]. In addition, surface protuberances, such as vortex generators, ribs, cubes, and tubes, are also frequently used. Those can be easily incorporated inside compact channels or into pipes of heat exchangers. In addition, the vortical structures induced by protrusions and other passive devices do enhance turbulence mixing and convective heat transfer [2, 5-7]. Coiled wires are also widely utilized in various heat transfer applications, such as chemical process plants, refrigeration and air conditioning systems, and heat recovery processes, due to their low cost and ease of installation in existing systems [46]. Coiled wires also enhance heat transfer by promoting turbulence and generating swirling motion in flow, which leads to a boundary layer thinning effect. However, pressure drop also increases considerably by introducing coiled wires in pipes [46].

2.6 Knowledge Gaps in the Literature

Overall, the work related to longitudinal vortices by conventional VGs is considerable as there are many applications across several disciplines. However, few studies have been done for

the trapezoidal VGs, especially how they affect heat transfer. Most of the work on single trapezoidal VGs has been conducted by considering the fluid dynamics of the coherent flow. Only few studies involving VGs have considered heat transfer phenomena. Therefore, there is a need to study the effects of geometric factors of trapezoidal VGs on the induced coherent flow and heat transfer process. Furthermore, there has been a lack of understanding of the effects of multiple trapezoidal VGs spacing on heat transfer and surface cooling. Therefore, in-depth heat transfer and fluid dynamics analyses considering the effects of multiple trapezoidal VGs spacing should be done.

In summary, characterization of the coherent flow induced by single and multiple trapezoidal VGs and their effects on heat transfer should be undertaken. For multiple trapezoidal VGs system, the effects of spanwise VGs spacing in a single row and streamwise spacing between successive rows of VGs need to be investigated. Finally, an optimal configuration of the VG system needs be identified by studying the effect of spacing between cluster of rows of VGs. Furthermore, the relationship between fluid dynamics and heat transfer phenomena in the wake of trapezoidal VGs is of interest as well.

CHAPTER III

DESCRIPTION OF EXPERIMENTAL SETUP

In order to achieve the aforementioned objectives, an experimental setup was developed and used to conduct smoke visualization, particle image velocimetry (PIV) and infrared (IR) thermography experiments. Those experiments share the same air duct but have different subsystems. Detailed descriptions of the air channel and each subsystem are provided below.

3.1 General System Description

Figure 1 shows a schematic representation apparatus, which has a 3.6 m long square Plexiglas duct with 0.1 m sides. Photographs of the apparatus are shown in Fig. 2. The duct's entrance (after the honeycomb structures), test section, and exit are 2.75 m, 0.3 m, and 0.6 m in length, respectively. A 12V DC brushless fan was used to blow air through the duct at room temperature. The flow velocity in the channel was controlled by a fan connected to a DC power supply and measured using a thermo-anemometer with an accuracy of ± 3%. The air settling chamber and two honeycomb structures were used to distribute air uniformly at the inlet of the test section. Smoke visualization, particle image velocimetry (PIV), and infrared (IR) thermography experiments were conducted using the common air duct but different subsystems were used as well, as described in the following sections.

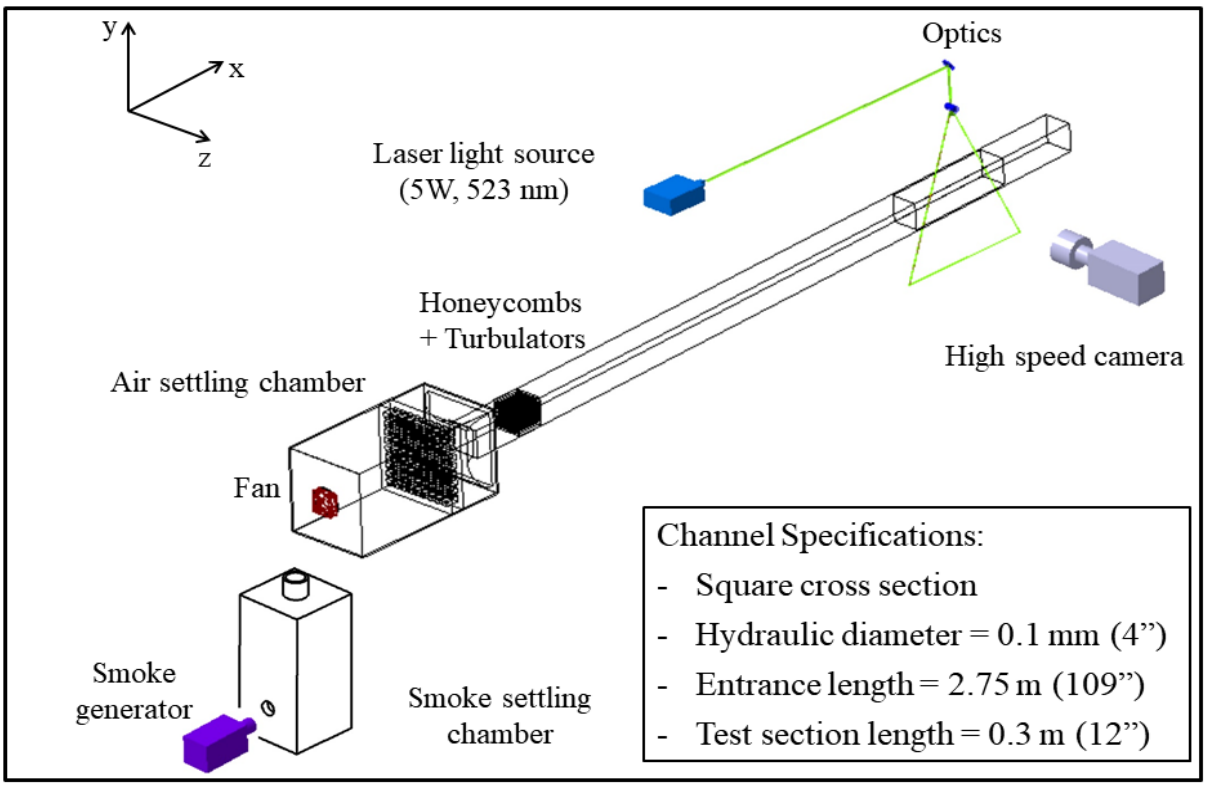

Fig. 1. Schematic of the experimental setup

The smoke settling chamber was built to remove any undesirable momentums generated by the smoke machine, as shown in Fig. 2b. The outlet of the smoke settling chamber was located close to a DC fan having a 150 mm spacing between the outlet and the fan. Smoke is passively entrained into the air settling chamber while a DC fan draws air from the atmosphere into the air settling chamber.

The air settling chamber was built to promote the flow to be uniform, as shown in Fig. 2c. The air settling chamber was 0.6 m long, 0.3 m high, 0.3 m wide. A bank of straws with diameter of 10 mm and length of 70 mm was employed inside of the chamber for flow uniformity. A ratio of the cross-sectional area of the chamber to the cross-sectional area of the duct was 9:1. Therefore, a gradual contraction section from the air settling chamber to the entrance of the duct

was made having a curvature radius of 60 mm to minimize entrance losses and suppress the increases of the level of turbulence of the flow [47], as shown in Fig. 2c.

At the entrance of the duct, two banks of small straws with diameter of 3 mm and length of 0.15 m were employed, as shown in Fig. 2d. The main purposes of a bank of straws were to straighten out the flow by reducing the transversal components of the flow velocity and to reduce the level of anisotropic turbulence [47]. Two banks of small straws used to ensure the inlet velocity profile was homogeneous.

Rectangular ribs with height of 6 mm and sandpapers (60 grit) were placed around the walls after the two banks of small straws to trip the flow and promote fully developed turbulent flow conditions for PIV and IR thermography experiments, as shown in Fig. 2e. However, smoke visualization experiments were conducted in the absence of the turbulators. Smoke visualization study was done under laminar flow condition at Reynolds number of 1965 without using the turbulators since smoke dissipated and dispersed quickly under turbulent flow condition.

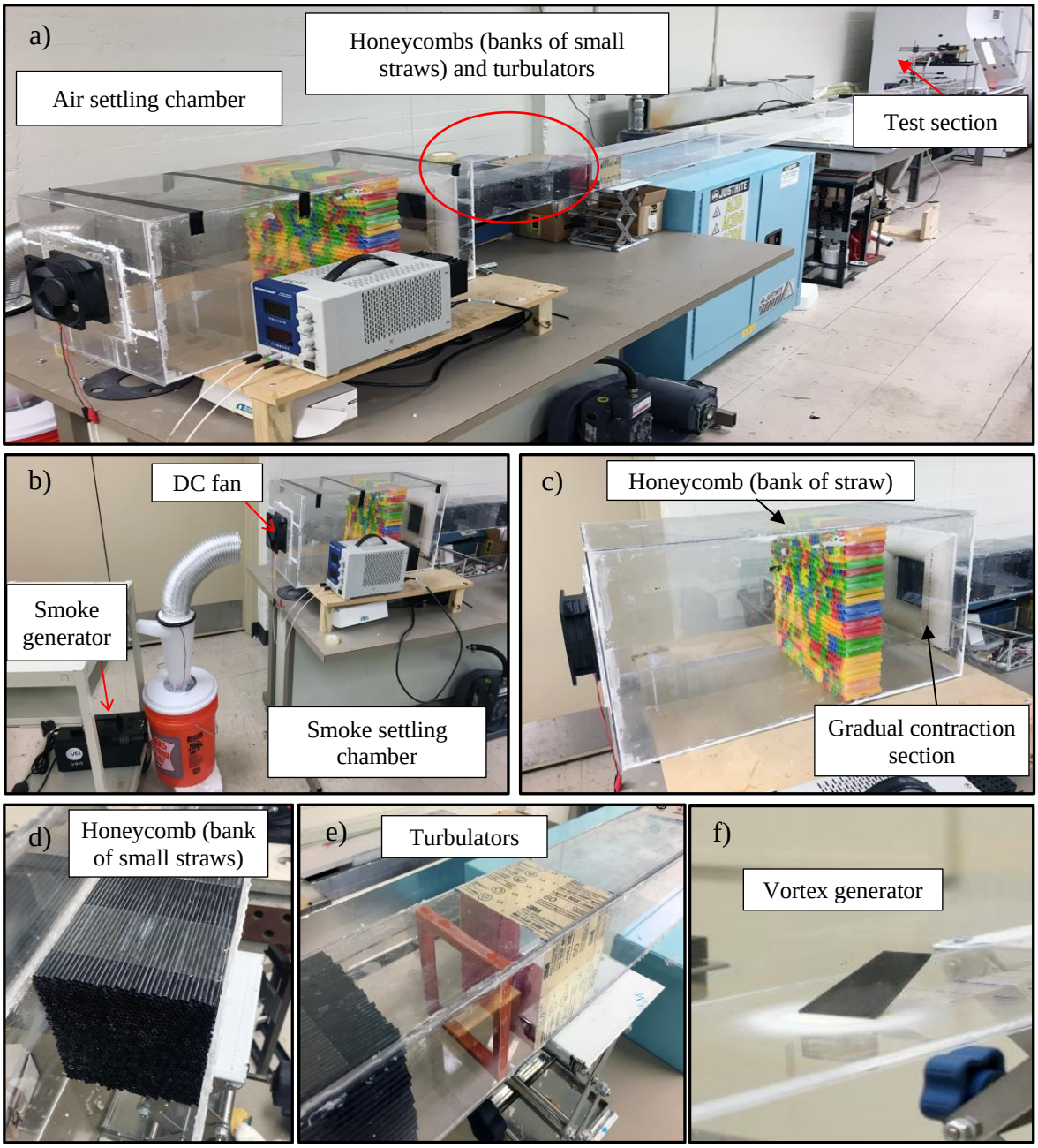

Fig. 2. Photographs of the a) experimental setup, b) smoke generator with the smoke settling chamber, c) air settling chamber, d) honeycomb (bank of small straws), e) turbulators, and f) vortex generator in the test section

3.2 Smoke Visualization System

Flow fields were qualitatively investigated via smoke visualization to understand the role of taper angle of trapezoidal VGs on formation of coherent structures in the wake of the tabs. In the smoke visualization study, the smoke-screen method was used [48]. Smoke was introduced at the inlet of the air duct so that broad, uniform smoke streaks flow over the entire test section [48]. The uniform smoke streaks then interacted with the corresponding tabs, which led to the formation of counter-rotating vortex pair (CVP). The resulting flow field was visualized by illuminating the flow field along the spanwise and streamwise planes.

The smoke visualization system in the present study is shown in Fig. 3. A 750 mW laser was used to generate a 3 mm thick light sheet, as shown in Fig. 3b. The vortical structures were captured with a digital camera at a rate of 30 frames per second (fps) with a resolution of 2 MP (1920 × 1080 pixels). The camera was positioned along the duct using a 50 mm single axis translation stage, with an accuracy of ± 10 μm. Water-based glycol was used to generate the smoke, where the smoke particles had Stokes number less than 10^{-4} for a flow velocity of 0.3 m/s (Re = 1965, with Re based on the hydraulic diameter). For smoke visualization, the turbulators after the honeycombs (or banks of straws) were removed for the laminar flow condition. Smoke was sprayed into the settling chamber and evenly distributed by the honeycomb structures. Smoke streaks were captured in the spanwise and streamwise planes illuminated by the laser. Representative views of the CVPs induced by a VG are shown in Fig. 4, including the coordinate system.

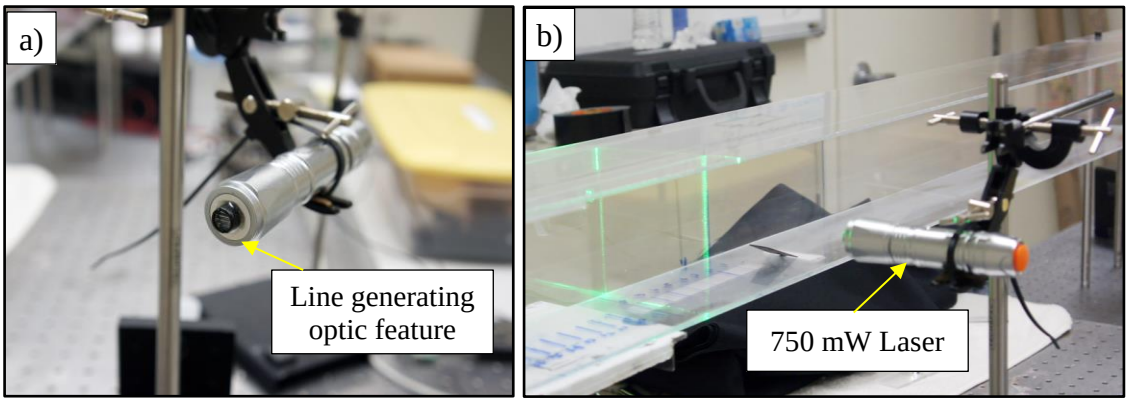

Fig. 3. a) A 750 mW laser with a line generating optic feature and b) sample image of use of 750 mW laser

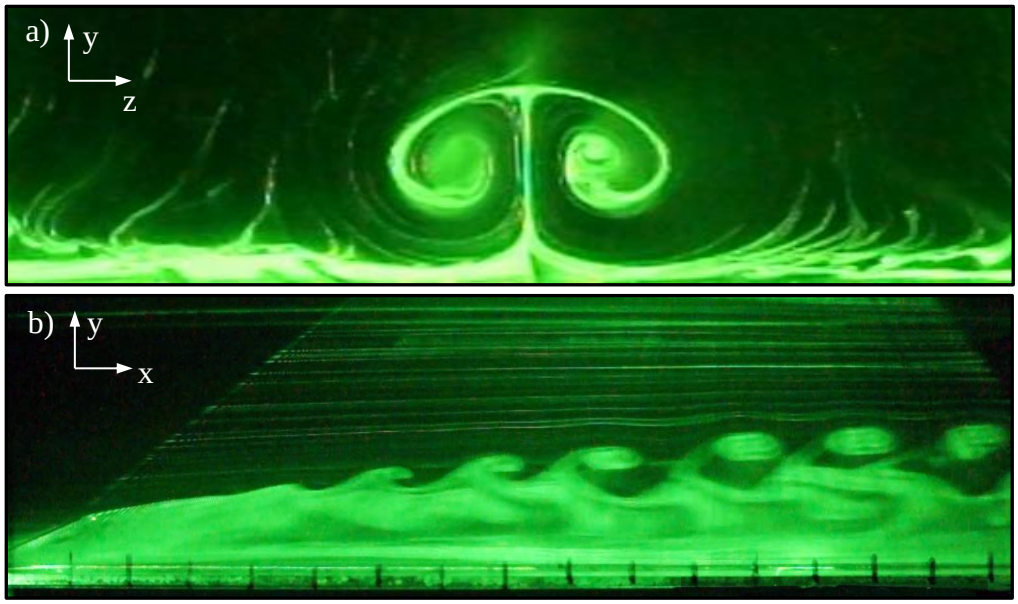

Fig. 4. Sample smoke visualization images taken in the a) spanwise plane, and b) streamwise plane

The frames from each video recording were extracted digitally, and pixel counts in each image were used to determine the horizontal and vertical coordinates (*a* and *b*) of the vortex cores as shown in Fig. 5a and 5b. The standard deviations associated with the *a* and *b*

measurements converged to 2 - 3% of the corresponding averaged values when using over 60 movie frames, as shown in Fig. 6. Therefore, 60 frames were considered adequate for estimating *a* and *b*.

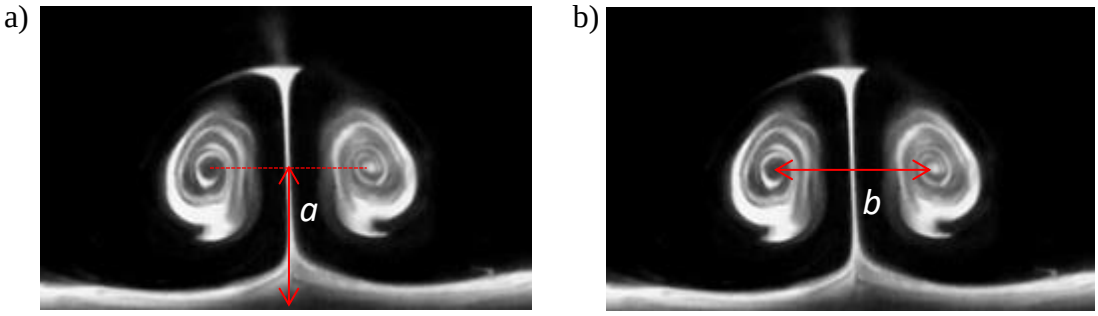

Fig. 5. a) CVP vertical core distance, *a*, and *b*) CVP horizontal separation distance, *b*

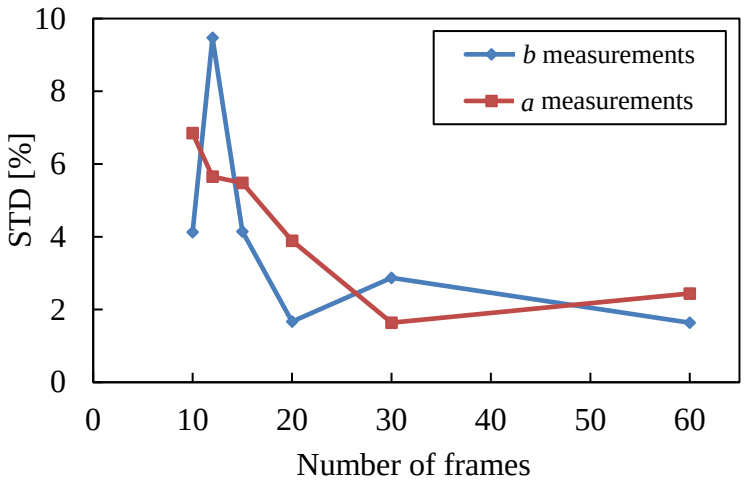

Fig. 6. Standard deviations associated with the *a* and *b* measurements using different number of frames, recorded for the VG-B case at x/β = 1.8

3.3 Particle Image Velocimetry (PIV) System

Particle Image Velocimetry (PIV) was used to obtain velocity of the flow fields induced by trapezoidal VGs. For PIV analysis, the flow was seeded with tracer particles and the particles were illuminated in a plane within a short time interval. The light scattered by the particles were

recorded on a sequence of frames. Then, displacement of the particles between the consecutive frames was determined through evaluation of the PIV recordings using a cross-correlation algorithm [49]. The cross-correlation algorithm can be found in Appendix A. Based on displacement and associated time interval, velocity values at discrete points were obtained.

For PIV experiments in this work, the air flow was seeded with smoke particles (water-based glycol), where the associated Stokes number was less than 10^{-3} for a 0.75 m/s of air flow velocity. Stokes number much less than 1.0 was recommended to ensure seeding particles followed the fluid flow accurately [49]. A field of view (FOV) 25 mm x 25 mm was illuminated using a 5W Diode-Pumped Solid State (DPSS) laser (continuous, wavelength of 532 nm). Figure 7 shows the laser and optical system, which generates a sheet of light illumination with a 1 mm thickness. A 2 mm beam diameter from the laser was reduced to 1 mm by using two concave lenses with different focal lengths (f_1 = 100 mm and f_2 = 50 mm). Powell lens was used to generate a light sheet from a laser beam.

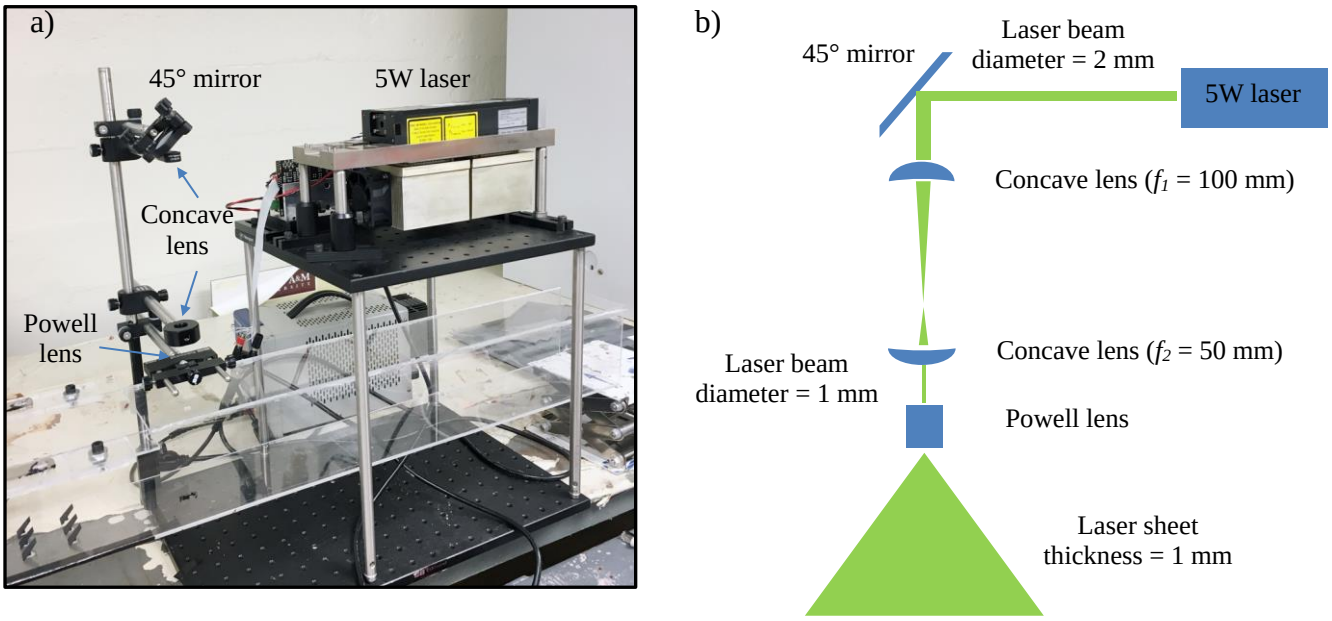

Fig. 7. a) Photograph and b) schematic of the laser and optical system for PIV analysis

The illuminated particles were captured with a high-speed camera (Photron SA3) and a Micro-NIKKOR 105mm *f*/2.8 lens. The image sampling rate was adjusted according to the flow velocity and set at 3000 frames per second (fps). Typical resolution of the particle image used in the present study was 45μm/px. The maximum displacement of the particles associated with the frame rate was 10 px approximately, which is recommended to minimize the number of pairing losses from the first frame and the second frame [49, 50]. The camera was placed perpendicular to the light sheet and was positioned along the channel using a 50 mm single axis translation stage, with an accuracy of ± 10 μm. A sample of the particle images in PIV analysis is shown in Fig. 8.

a) b)

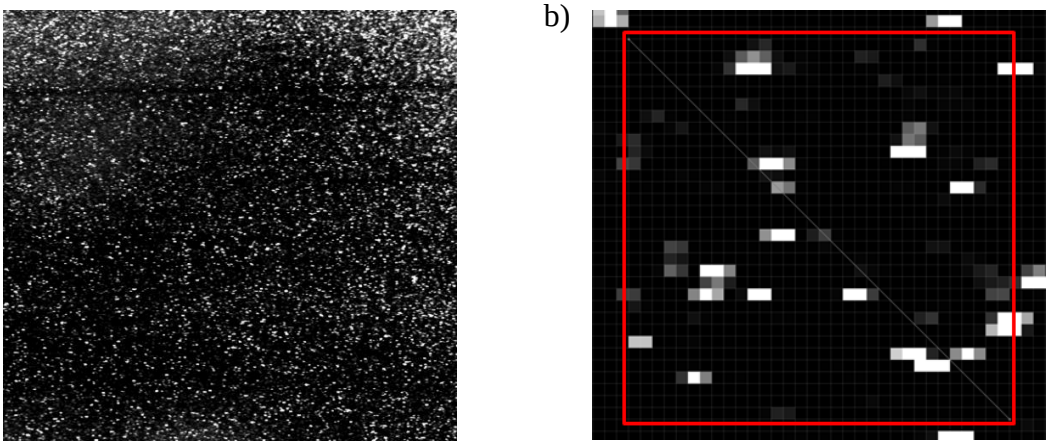

Fig. 8. Sample images for smoke particles in PIV analysis a) in the field of view and b) in the interrogation window (10 -15 smoke particles in the interrogation window)

The cross-correlation of the PIV recordings was performed using PIVLab. PIVLab is an open source Matlab-base package developed by Thielicke and Stamhuis [51] and has been verified by several investigators [52-56], see Appendix A. Two interrogation windows of sizes 64 x 64 and 32 x 32 pixels were used for data processing with a 50% overlap with the neighboring interrogation regions. After calculating the velocity vectors for each image pair, PIVlab runs an algorithm that identifies erroneous vectors using the standard deviation threshold value. Then, the algorithm eliminates the erroneous vectors and replace them using the mean velocity values, based on the neighboring vectors. The details of the algorithm can be found in [51].

The accuracy of PIV data depends on the ability of the seeding particles to follow the flow (particle dynamics), the precision of imaging system (equipment), and the particle image analysis procedure [57]. Among the PIV uncertainty sources, uncertainty associated with particle dynamics was neglected due to the low flow velocity (U = 0.75 m/s) and the low Stokes number

(Stk = 10^{-3}) [49, 57]. Therefore, the uncertainty associated with the equipment and sampling of the image pairs were considered in this work [57].

To estimate uncertainties from the equipment, uncertainties of scaling magnification and the timing accuracy were considered [57]. The scaling magnification relates physical length units to pixel units, and timing accuracy is based on the accuracy of the separation time between PIV image pairs. The scaling magnification is calculated by taking images of a calibration scale target of known length under the same conditions as those encountered by the trace particles during the imaging process. Then the scaling magnification factor (ψ) can be calculated as follows [58]:

$$\Psi = {}^{d}/_{D} \tag{2}$$

where d is the length of the calibration scale target in a physical scale (mm or μm) and D is the length on the imaged plane in pixels. In the present study, a calibration scale target with 100 μm-thick lines was used. Therefore, the uncertainty of the length on the calibration scale target (d) was 100 μm at most (w_d = ±100 μm). For the length of the calibration scale on the image (D), two sources of error were considered [57]. First, when the length on the image plane was measured from two points on the image, the uncertainty band for each point was 0.5 pixels (w_{D1} = 1 pixel) [57]. Secondly, the image distortions by lens aberrations cause the uncertainty to be approximately 0.5% of the total length of the calibration scale [57, 58]. As the total length of the calibration scale was set to 627 px, the image distortion by the lens was then 3 px (w_{D2} = 3 pixels). In summary, both w_{D1} and w_{D2} represent uncertainty of D [57].

The PIV system uses a continuous laser and the accuracy in separation time of the PIV image pairs is dictated by the accuracy of sampling rates of the high-speed camera. The accuracy of the camera's sampling rates is based on the crystal oscillator in the camera itself. From the

manufacturer specifications, Photron SA3 uses a 30 PPM oscillator and the uncertainty of the sampling rate is 10 ns (w_t = 10 ns) for 3000 fps.

To apply the uncertainty analysis described above in the velocity measurements, the flow velocity when using the PIV system is expressed as follows [57, 58]:

$$u = \psi\tilde{u} = \psi\left[\frac{mm}{px}\right]\frac{\Delta x}{\Delta t}\left[\frac{px}{sec}\right] \tag{3}$$

where $\tilde{u}$ is PIV velocity measurement in a pixel-time reference frame, Δx the pixel displacement between PIV image pairs, and ψ and Δt are the scaling magnification factor (Eq. 2) and separation time of the PIV image pairs, respectively. Therefore, using the second order method of Kline and McClintock [58], the uncertainty of PIV velocity measurement due to equipment errors can be expressed as follows.

$$w_u = \sqrt{\left(\frac{\partial u}{\partial d}w_d\right)^2 + \left(\frac{\partial u}{\partial D}w_{D1}\right)^2 + \left(\frac{\partial u}{\partial D}w_{D2}\right)^2 + \left(\frac{\partial u}{\partial t}w_t\right)^2} \tag{4}$$

$$= \sqrt{\tilde{u}^2\left[\left(\frac{1}{D}w_d\right)^2 + \left(\frac{-d}{D^2}w_{D1}\right)^2 + \left(\frac{-d}{D^2}w_{D2}\right)^2\right] + \left(\frac{-\tilde{u}}{\Delta t}\frac{l}{L}w_t\right)^2}$$

Associated values for uncertainties analysis are summarized in Table 1. The results of solving Eq. 4 suggested that the uncertainty of velocity measurements (w_u) due to the equipment errors (w_u/u) was 0.48%.

Table 1. Summary of equipment uncertainty parameters

Source of uncertainty	Parameter	Description	Value	Uncertainty
Calibration	d	Calibration scale physical length	25.4 mm	100 μm
	D_1	Calibration scale image plane length	627 px	1 px
	D_2	Image distortion due to aberrations	627 px	3 px
Timing	t	Accuracy of high speed camera	0.0005 sec	15ns

In order to accurately measure velocity by PIV, a sufficient number of image pairs is required. Given a set of samples $m = \{m_1, m_2, \ldots, m_N\}$ recorded over time, the temporal mean value of m is defined as follows:

$$\bar{m} = \frac{1}{N}\sum_1^N m_i \tag{5}$$

In addition, the standard deviation for a sample of the population can be expressed as follows:

$$\sigma = \sqrt{\frac{1}{N-1}\sum_{i=1}^{N}(m_i - \bar{m})^2} \tag{6}$$

Then, the standard deviation of the mean (or standard error, w_s) can conveniently be expressed as follows [57, 58, 60]:

$$w_s = \frac{\sigma}{\sqrt{N}} \tag{7}$$

In order to compute uncertainty from image sampling as described above, PIV experiments were conducted in the absence of vortex generator (baseline case). The sampling rate was set to 3000 fps and the field of view was 25 mm by 25 mm with a resolution of 45 μm/px. The flow field was recorded for 3.6 seconds and the corresponding 5000 frames of the PIV recording were used for data processing by using PIVLab. The streamwise velocity data (U) from the PIV experiments were used to solve Eqs. 5-7. As a result, the maximum uncertainty of the streamwise velocity (U) due to sampling errors was ~0.6% near the wall, as shown in Fig. 9.

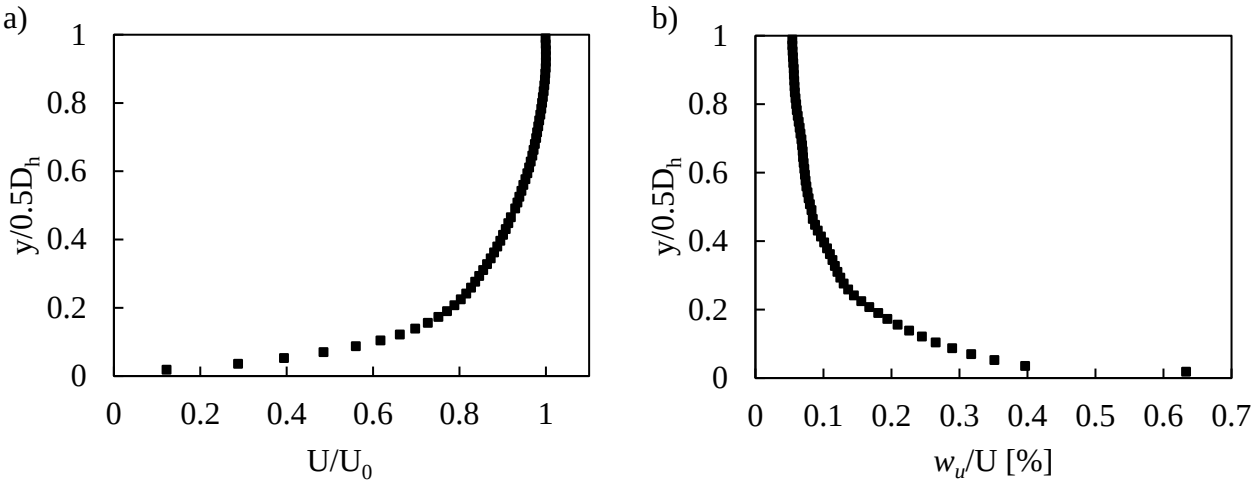

Fig. 9. a) The mean streamwise velocity distribution and b) uncertainties associated with image sampling for the baseline (no VG) case

3.4 Infrared (IR) Thermography System

Infrared (IR) thermography was used to obtain the surface temperature distributions in the wake of trapezoidal VGs. The IR system consists of a camera sensor (radiometer) that detects infrared energy emitted from any surface and converts it to apparent temperature. The temperature measurement is presented in a digitized image rendering, with a specific temperature value per pixel.

In the present study, the infrared (IR) thermography system used the same air duct as shown in Fig. 1. However, a 12.7 mm (0.5 in) thick Plexiglass was used as thermal insulator on the top and side walls of the test section to minimize heat losses. A customized heater (0.6 m in length) was developed to provide uniform, constant heat flux condition, as shown in Fig. 10. Insulated Nichrome wires (24-gauge wire with resistance of 5.2 Ω/m) were wound around two of Ultem Polyetherimide (PEI) plastic sheets with thermal conductivity, *k*, of 0.22 W/m·K. Two independent nichrome wire sections were fabricated having same resistance (390 Ω) per section.

The nichrome wire sections were connected in parallel to a variable voltage transformer so the heat fluxes from the two sections were identical. A 0.5 mm thin stainless-steel sheet coated with black paint (emissivity, $\varepsilon = 0.92$) was attached on the heat transfer surface to ensure uniform heat flux coming from the nichrome wires. Furthermore, the stainless-steel plate was used as smooth surface [61-63]. Sample IR images for the baseline case (no VG) and the single VG case (trapezoidal $\theta = 60°$, top view) taken from the test section are shown in Fig. 10.

The infrared camera (FLIR A325) with a 10 mm lens was placed on a translation stage to measure surface temperature of the test surface. The test section was viewed through an infrared window consisting of a Zinc Selenide substrate (Fig. 10c). The transmissivity of the anti-reflective (AR) IR window (ZnSe) was 98% in the IR wavelength range of 8 μm - 12 μm. The field of view through the IR window was 43.5 mm x 90 mm. The top side of the heat transfer section was made of fourteen of 38 mm (1.5") Plexiglass blocks and the IR window. The IR window was moved in the axial direction by swapping its position with each Plexiglass block. As it moved in the axial direction by a 38 mm step, only 12% of the IR images overlapped.

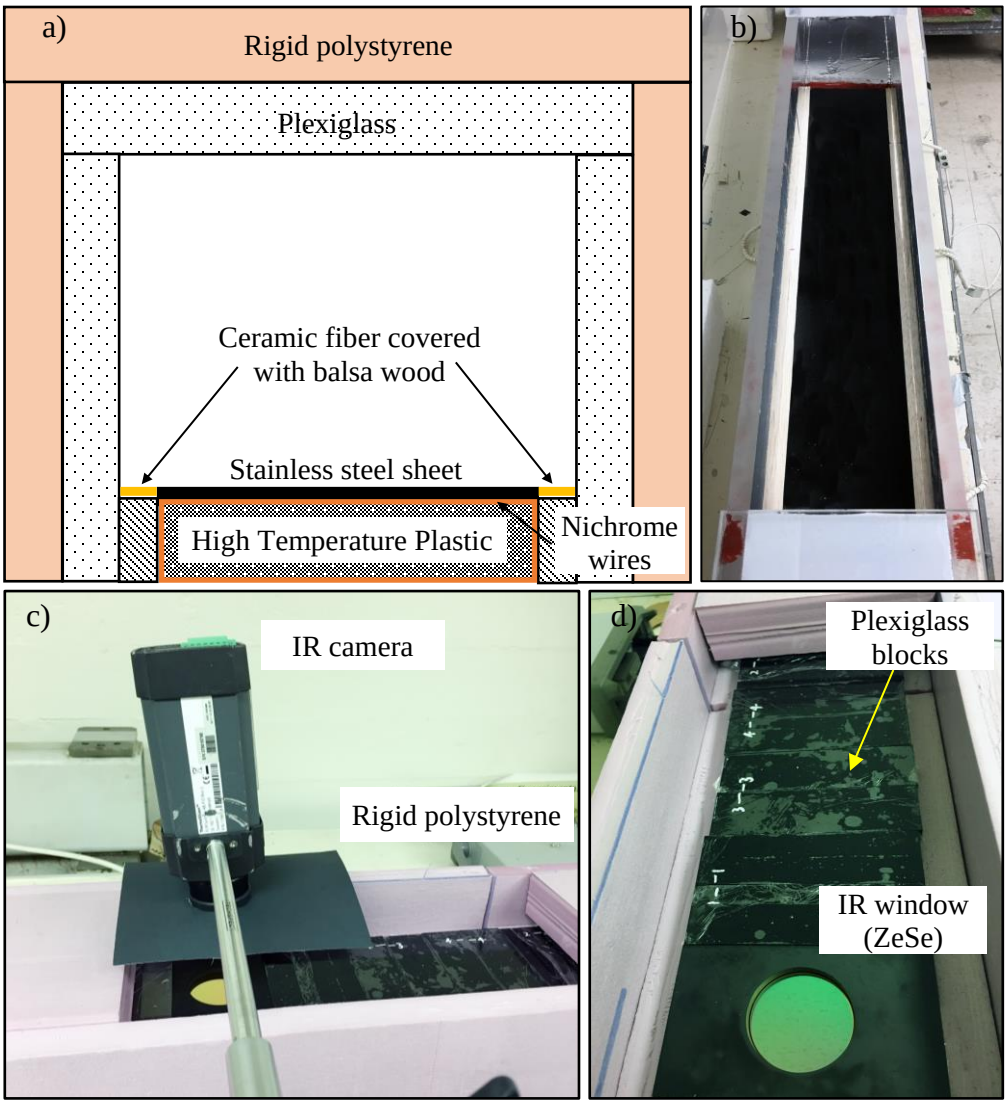

Fig. 10. a) Schematic of the heating system (cross-section view), b) photographs of heater with a stainless-steel sheet painted black (top view), c) IR camera with the test section covered using rigid polystyrene insulation, and d) top of the test section with IR window

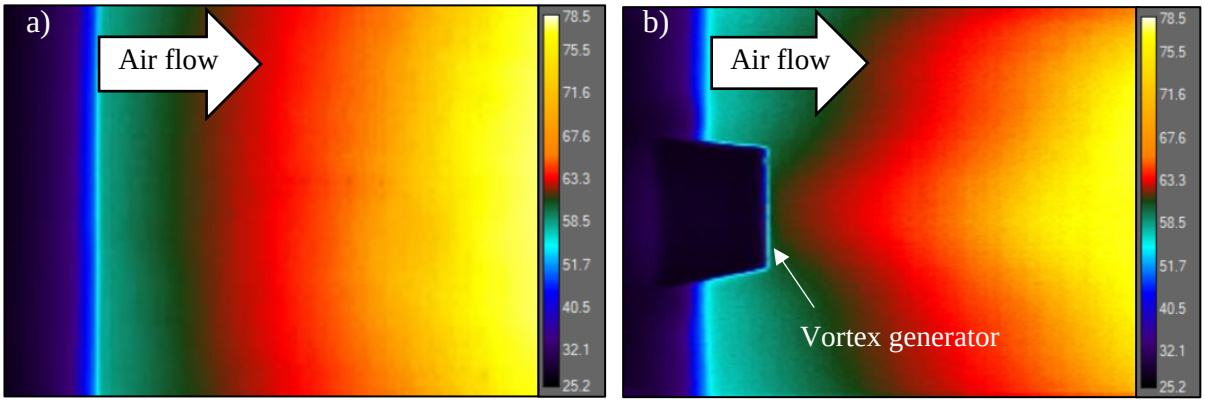

Fig. 11. Sample IR images of the (a) baseline (no VG) case (top view), and b) single VG case (trapezoidal θ = 60°, top view)

The IR emissivity of the heater surface with the stainless-steel sheet was measured following the process and recommendations described in Driggers [64]. The setup used for emissivity measurement is shown in Fig. 12. A reference tape of known emissivity (3M vinyl tape Supper 88, ε_{ref} =0.95) was used in the experiments.

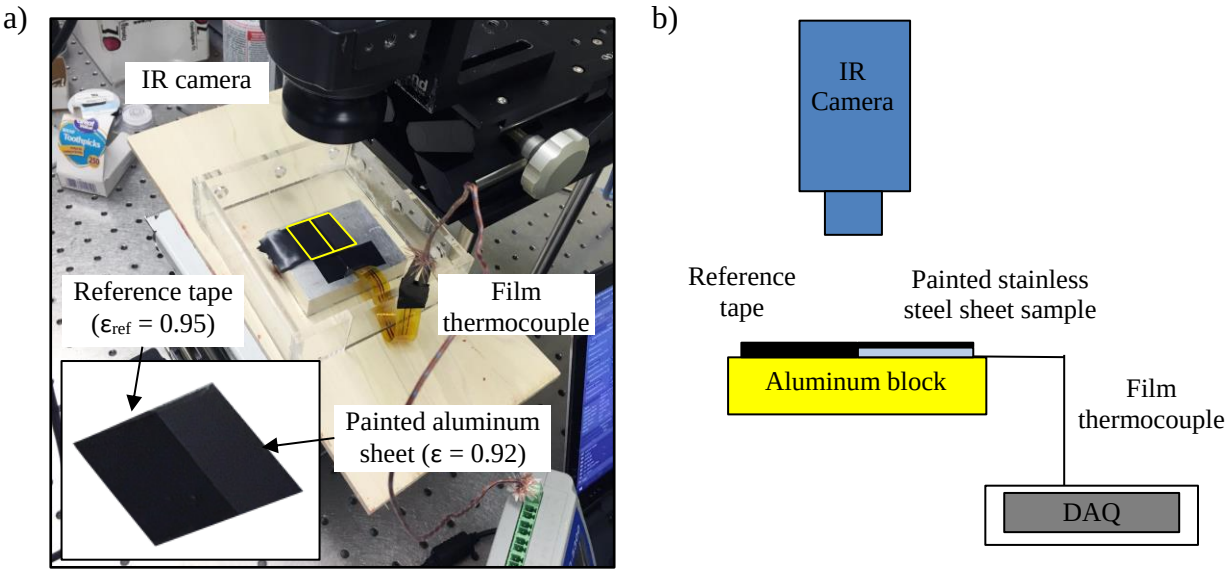

Fig. 12. Emissivity measurement setup

The specific steps for emissivity measurements are summarized as follows [64]:

1. Measure the IR digital counts from the surroundings (D_{sur}). This was done by placing a reflective aluminum foil within the field of view of the IR camera and capturing an IR image of the foil.
2. Attach the reference tape to an aluminum block and place the stainless-steel sheet sample adjacent to the tape. Heat the aluminum block, tape and sample in an oven so their temperature is at least 35°C higher than the ambient temperature.
3. Take the sample, together with the tape and aluminum block out of the oven quickly. Place the sample and the tape within the field of view of the IR camera and capture an IR image of the sample and the tape. Measure the IR digital counts from the sample (D_{sample}) and the reference tape (D_{ref}).

By using the methodologies described above, IR emissivity of the stainless-steel sheet (ε_{sample}) can be calculated using Eq. 8 [64], as follows:

$$\varepsilon_{sample} = \frac{D_{sample} - D_{sur}}{D_{ref} - D_{sur}} \varepsilon_{ref} \quad (8)$$

The calculated emissivity of the stainless-steel sheet is shown in Fig. 13. The averaged emissivity was 0.916 with standard deviation of 0.004.

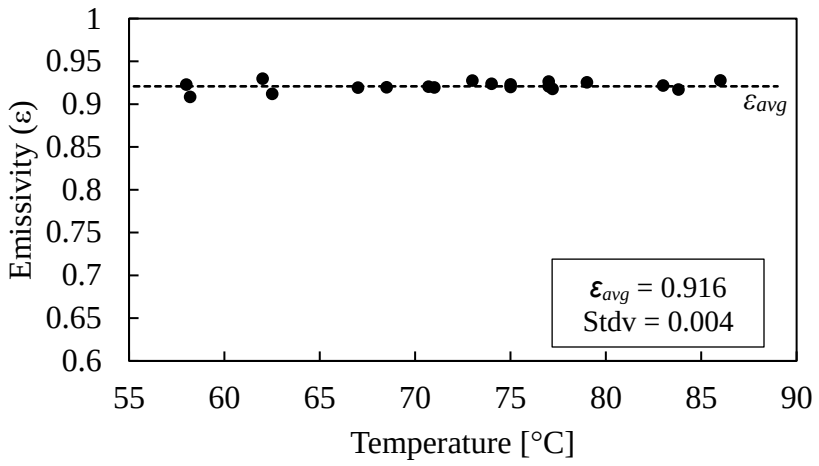

Fig. 13. Emissivity measurement of the painted stainless-steel sheet

As shown in Fig. 13, the measured emissivity of the heater is almost constant within the temperature range of 55 – 90 °C. Emissivity of the heater at lower temperatures (30 – 55 °C) were not measured due to the limitations of the emissivity measurement methodology [64]. Since the target for emissivity measurements should be at least 35 °C higher than the ambient temperature, it is assumed that the emissivity of the heater is a constant (ε = 0.92) within the temperature range of interest.

IR temperature measurement validation experiments were also conducted using a thin film thermocouple (OMEGA Type T Cement-On Surface Thermocouple, thickness = 13 μm, accuracy ± 1°C). As shown in Fig. 12, a film thermocouple was placed between the stainless-steel sheet sample and the aluminum block. Both of the sample and aluminum block were heated in an oven to a desired temperature range (60 - 100°C). Temperatures measured by using the film thermocouple and IR camera are shown in Fig. 14. The averaged emissivity of 0.916 was used for IR camera measurement, which was obtained from the emissivity measurement experiments (Fig. 13). As shown in Fig. 14, the agreement of the IR camera measurement and thermocouple measurement was excellent. The largest differences between temperature measurements by IR

camera and thermocouple were 0.7°C within a temperature range of 60 – 90°C, which was within the uncertainties of both instruments (± 1 °C). Therefore, temperature measurements by the IR camera may be regarded as accurate.

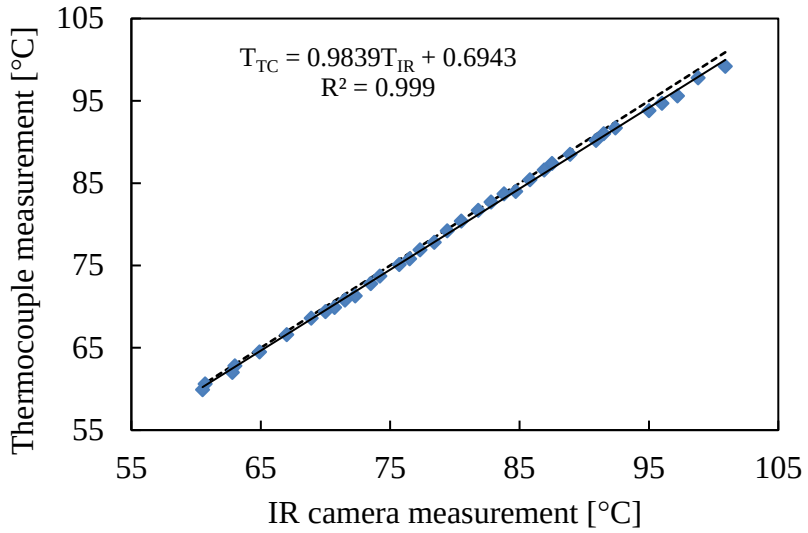

Fig. 14. Comparison of IR and film thermocouple temperatures

Three thermocouples (T-type) with uncertainty of ± 1°C and six thermocouples (T-type) were installed before and after the heat transfer section to measure bulk air temperature. After the heat transfer section, three thermocouples (T-type) were mounted near the top wall and the other three thermocouples (T-type) were mounted near the bottom wall as shown in Fig. 15. In addition, two plastic meshes were installed after the heater to promote uniformly distributed bulk air temperature at the exit. Typical readings of the six thermocouples at the exit are shown in Fig. 16. All the data from the thermocouples were recorded using a data logger and the power input to the nichrome wire sections was measured using a voltmeter and an ammeter.

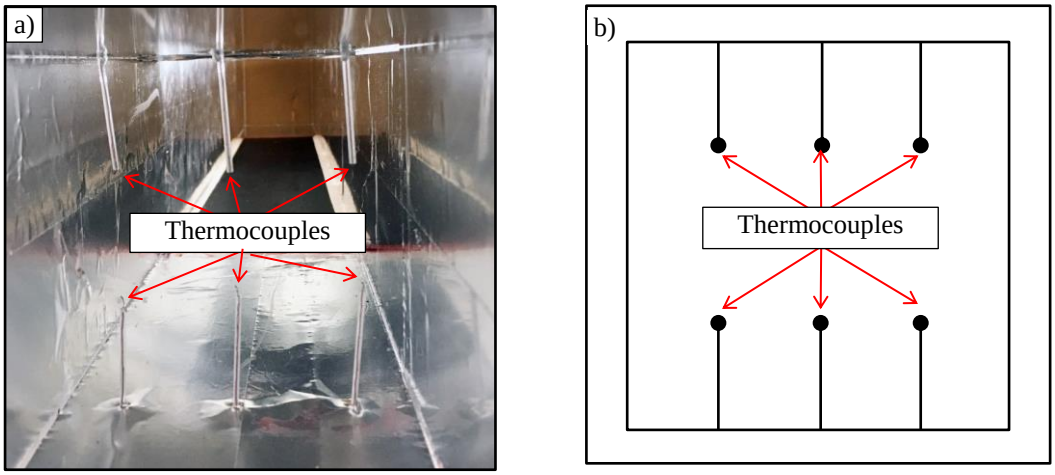

Fig. 15. a) Photograph and b) schematic of six thermocouples located at the exit: three near the top wall and the other three near the bottom wall

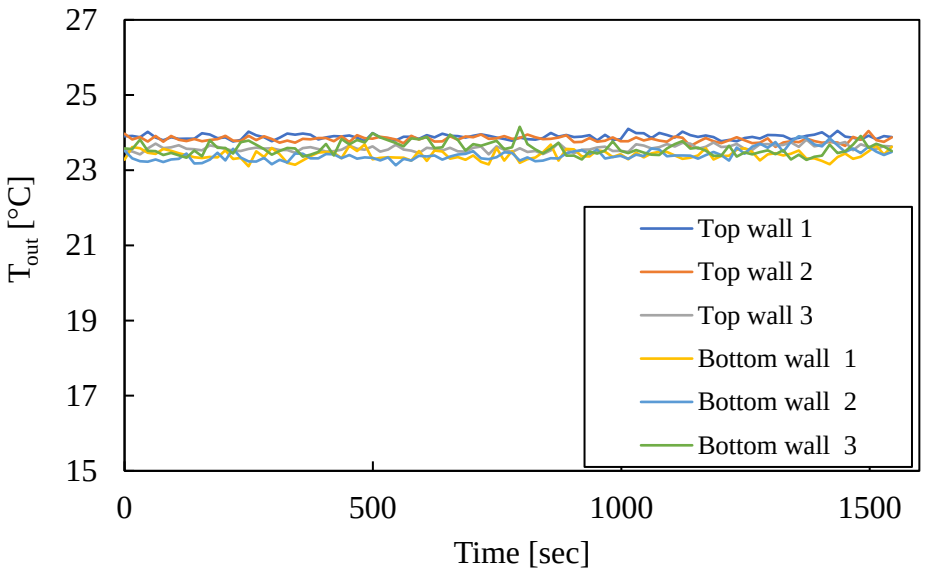

Fig. 16. Typical thermocouple readings at the exit

Due to the high emissivity of the heater surface, radiative heat losses could be significant in the plexiglass channel due to the high emissivity of the plate ($\varepsilon = 0.92$) and plexiglass ($\varepsilon = 0.65$). Therefore, the walls were covered using a thin aluminum foil ($\varepsilon = 0.09$) to minimize radiative heat losses. The radiative heat loss from the heater system was estimated by

considering the radiation view factor (*VF*) from the heated bottom surface to the top wall and to the two side walls [65, 66].

$$Q_{loss,rad}=\sigma VF_{heater\rightarrow top}A_{heater}\left(T_{heater}^4-T_{top}^4\right)+2\times\sigma VF_{heater\rightarrow side}A_{heater}\left(T_{heater}^4-T_{side}^4\right) \quad (9)$$

where σ is the Stefan-Boltzmann constant, $VF_{heater \rightarrow top} = 0.32$, $VF_{heater \rightarrow side} = 0.25$ [67]. The mean temperature of the heated surface (T_{heater}) was measured directly by using the IR camera. Wall temperatures (T_{top} and T_{side}) were assumed to be equal to the mean air temperature [68]. By solving Eq. 9, radiation losses from the bottom surface to the other surfaces was estimated as ~5% of the total flux.

3.5 Geometric Factors of Vortex Generators

Several vortex generator (VG) designs were considered in this study. The VGs were fabricated by using a 3D printer. The resolution of 3D printing was 100 microns per layer. The 3D printed VGs were used for both PIV experiments and heat transfer experiments. For heat transfer experiments, the VGs were placed directly on top of the heater. Therefore, the VGs were fabricated with Polycarbonate so that those could resist to high temperature condition (55 – 90 °C). 3D printed polycarbonate used in this study had a high heat deflection temperature of 138°C [69].

In the smoke visualization study, four vortex generators (VGs) with taper angles (ϕ) of 0˚ (rectangular), 7.6˚ (trapezoidal), 13.5˚ (trapezoidal) and 19.3˚ (triangular) with a common inclination angle (θ) of 24.5°, a base width (*l*) of 28.7 mm, a chord length (*c*) of 40.8 mm and height (β) of 17.3 mm were fabricated and placed pointing downstream in a square duct. The case of ϕ = 7.6° and θ = 24.5° was based on those used in other studies [26, 27, 29] for validation purposes. Furthermore, the taper angles used in the study take into account the two limiting cases

(rectangular VG and triangular VG). Table 2 summarizes the main geometric characteristics of the VGs used in smoke visualization experiments and Fig. 17 (a-c) shows different views of the VG.

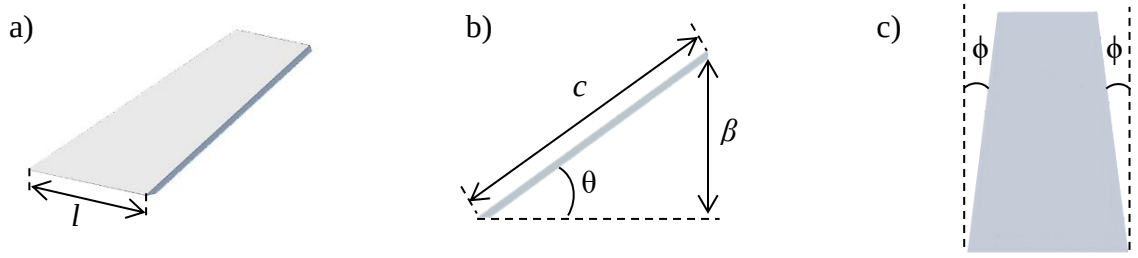

Fig. 17. Physical variables of vortex generator: a) isometric view, b) side view, and c) top view

Table 2. Geometric factors of the VGs in smoke visualization study

VG Type	Taper angle (ϕ) [°]	VG width at 50% chord (l_{50}) [mm]	Aspect ratio (*AR*), $\left(l/c\right)$
VG-A	0	28.7	0.70
VG-B	7.6	23.3	0.57
VG-C	13.5	18.9	0.46
VG-D	19.3	14.4	0.35

In particle image velocimetry (PIV) and infrared (IR) thermography experiments, inclination angle (θ) of the VG was varied as 24.5°, 45° and 60° for the single VG cases. At each inclination angle, taper angles (ϕ) of 0˚ (rectangular) and 7.6˚ (trapezoidal) were also considered. The chord length (*c*) and the base width (*l*) were fixed as 41 mm and 28.7 mm, respectively (Fig. 17). However, for the multiple VG cases, the size of the VGs were reduced by 55% of those used in the single VG cases so that three VGs can be employed within the limited width of the duct. The chord length (*c*) and the base width (*l*) were reduced to 18.5 mm and 13 mm, respectively.

Inclination angle of the VGs (θ) was set at 45° and the corresponding height of the VG (β) was 13 mm for all of the multiple VG cases. Taper angle (ϕ) of the VGs were also fixed at 7.6˚ so all the VGs were trapezoidal in shape. Table 3 summarize the details of geometrical characteristics of the VGs used during the PIV and IR thermography experiments.

Table 3. Geometric factors of the VGs in particle image velocimetry (PIV) and infrared (IR) thermography experiments

Case	Inclination angle (θ) [°]	Height (β) [mm]	Base width (l) [mm]	Chord length (c) [mm]
Single VG (Rectangular and Trapezoidal shapes)	24.5	17	28.7	40.8
	45	29		
	60	35.5		
Multiple VGs (Trapezoidal shape)	45	13	13	18.5

CHAPTER IV

RESULTS AND DISCUSSIONS

In this chapter, experimental results are presented and discussed for single and multiple vortex generators. Smoke visualization results of the coherent flow induced by single trapezoidal vortex generators (VGs) with different taper angle are presented first. The vortex path was measured using smoke images and compared with analytical models, which were developed based on potential flow theory. Furthermore, mean velocities and their local or fluctuating components were obtained using particle image velocimetry (PIV). Also, surface temperature distributions were obtained using infrared (IR) thermography for single VG cases and multiple VG cases.

4.1 Smoke Visualization and Determination of CVP Stability Range for Single Vortex Generators*

The effects of VG taper angle on CVP flow behavior was observed experimentally with smoke visualization. Reynolds number of 1965 based on the hydraulic diameter was used so that the flow was laminar during the experiments. Figure 18 shows the smoke images of the coherent structures induced by trapezoidal VGs. The images were taken in the spanwise plane at $x/\beta = 1$, where the CVPs were stable. As shown in Fig. 18, the trapezoidal VGs with different taper angle generated distinctive CVPs. The cross-section of the vortices generated by trapezoidal VGs were elliptical. In addition, it was qualitatively observed that the horizontal separation distance (*b*, Fig. 5) decreased as taper angle (ϕ) increased.

*Part of the data reported in this chapter is reprinted with permission from "Experimental and Numerical Visualization of Counter Rotating Vortices" by Park *et al.*, 2016, *Journal of Heat Transfer*, 138(8), 080908, Copyright [2016] by ASME

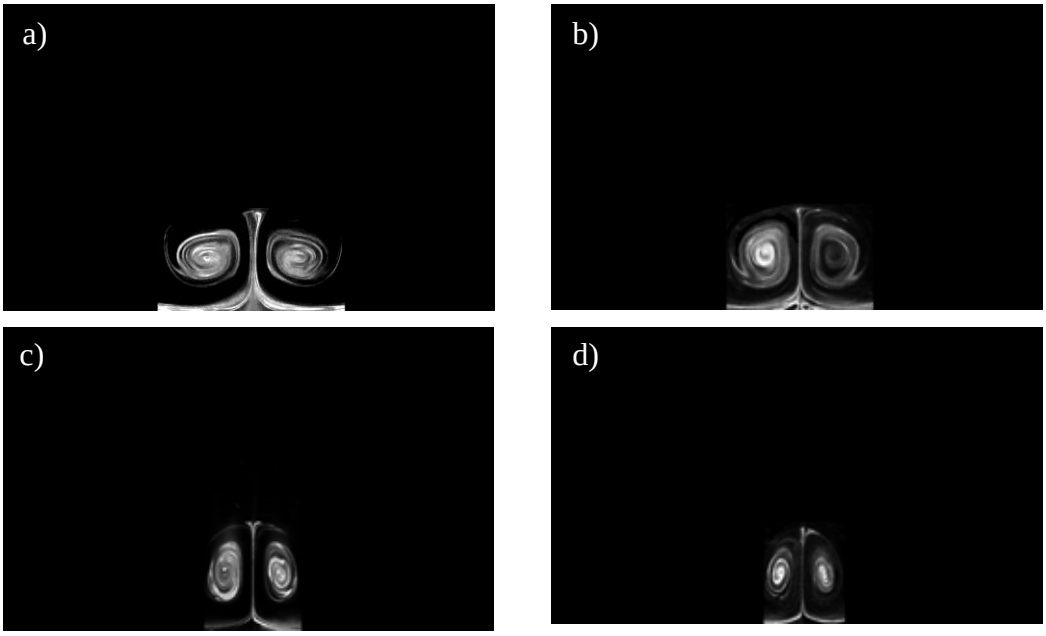

Fig. 18. Instantaneous counter-rotating vortex pair (CVP) images by smoke visualization at x/β of 1 and Re = 1965 a) VG-A (ϕ = 0°), b) VG-B (ϕ = 7.6°), c) VG-C (ϕ = 13.5°), and d) VG-D (ϕ = 19.3°)

The smoke images of the flow in the wake of trapezoidal VGs were taken in the streamwise plane. It was observed that the flow induced by all tested VGs experienced Kelvin-Helmholtz instability and potentially evolved into periodical hairpin vortex (Fig. 19). Hamed *et al.* [30] also observed K-H instability and hairpin vortices regardless of the width of the trailing edge of VGs for both laminar flow and turbulent flow conditions, which is consistent with the result of the present study.

The location of the onset of K-H instability was determined from 15 overlaid frames recorded during each smoke test, as shown in Fig. 20a, where two tangential lines were drawn following the maximum spread of the smoke streaks. The onset location of instability was estimated at the intersection of the two lines. Figure 20b shows the location of the onset of K-H instability as a function of taper angle (ϕ) of the corresponding VGs. The trend suggests a linear relation between taper angle and the onset of instability. The rectangular tab (VG-A, ϕ = 0°) led

to K-H instability at a shorter axial distance of x/β. Based on the results shown in Fig. 20b, the stability region of the coherent flow was identified as x/β < 2. Beyond the stability region, the CVP was subject to flow instability and began to fluctuate. Therefore, the coordinates of the vortex cores (*a* and *b* in Fig. 5) were measured only within the stability region.

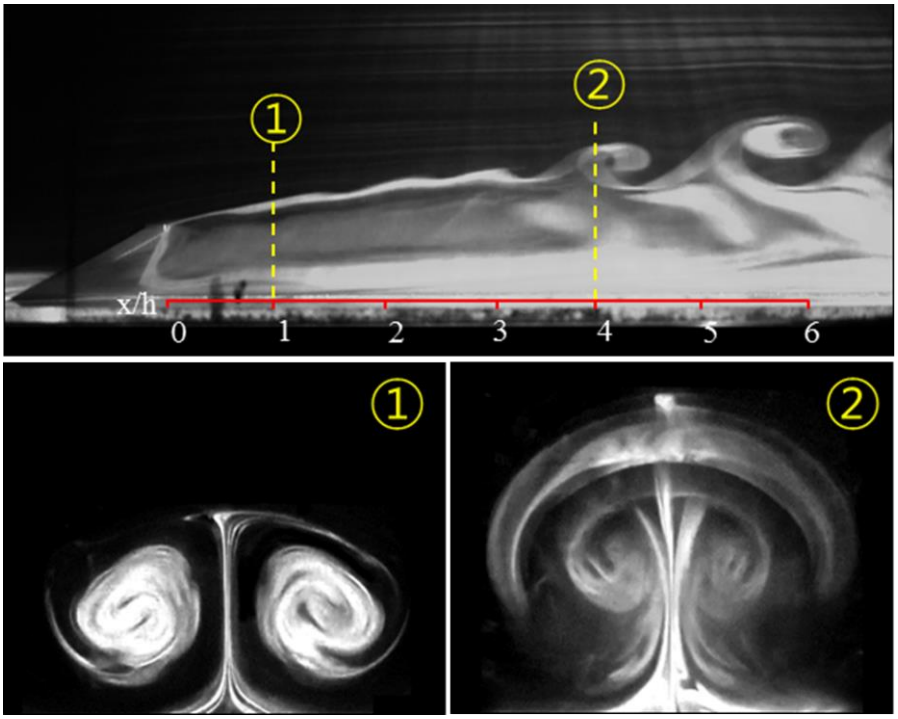

Fig. 19. Visualization of the coherent flow structures in the wake of VG-A at Re = 1965, reprinted with permission from ASME

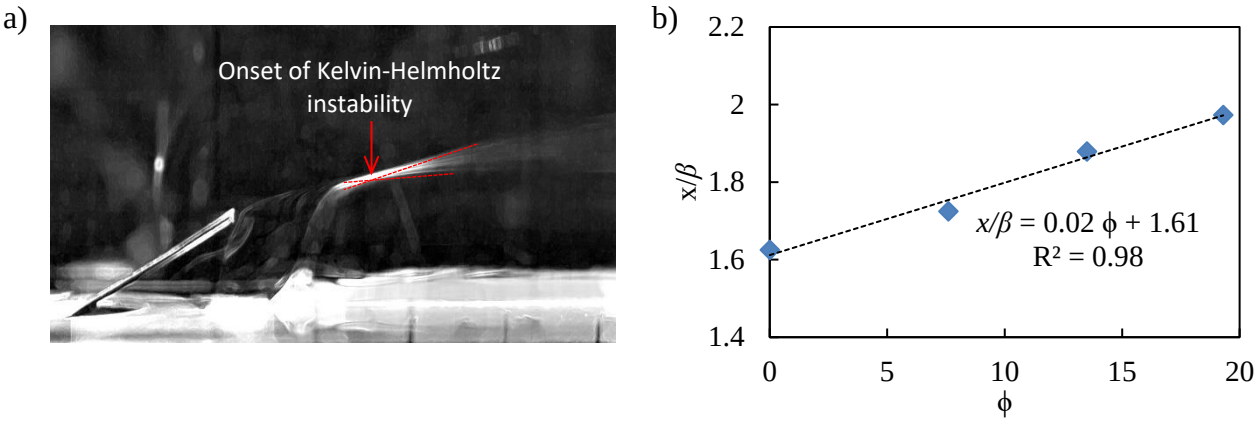

Fig. 20. a) Determination of the location of the onset of Kelvin-Helmholtz instabilities by overlaying 15 consecutive images and b) streamwise location of the onset of Kelvin-Helmholtz instability for different taper angles of trapezoidal VGs, reprinted with permission from ASME

4.2 CVP Paths Predictions by Analytical Models*

Bulk behavior of CVP induced by the trapezoidal VGs can be estimated analytically using 2D potential flow theory [15-19]. In this study, the location of CVP cores along the axial direction was predicted by using the inviscid potential flow model and pseudo-viscous flow models. The ability of the analytical models on predicting the path of CVP was assessed by comparing the analytical solutions with the smoke visualization results within the stability region ($x/\beta < 2$) as shown below.

CVP path based on inviscid potential flow model

Jones [15] developed an analytical model to predict the location of CVP cores (*a* and *b*) along the axial distance when multiple CVPs were present as predicted based on potential flow theory. Figure 21a shows a schematic of potential counter-rotating vortex pairs (CVPs) on a flat wall in a real plane and in an imaginary plane.

*Part of the data reported in this chapter is reprinted with permission from "Characterization of Tab-Induced Counter-Rotating Vortex Pair for Mixing Applications" by Park *et al.*, 2016, *Journal of Basic Engineering*, 139(3), 031102, Copyright [2016] by ASME

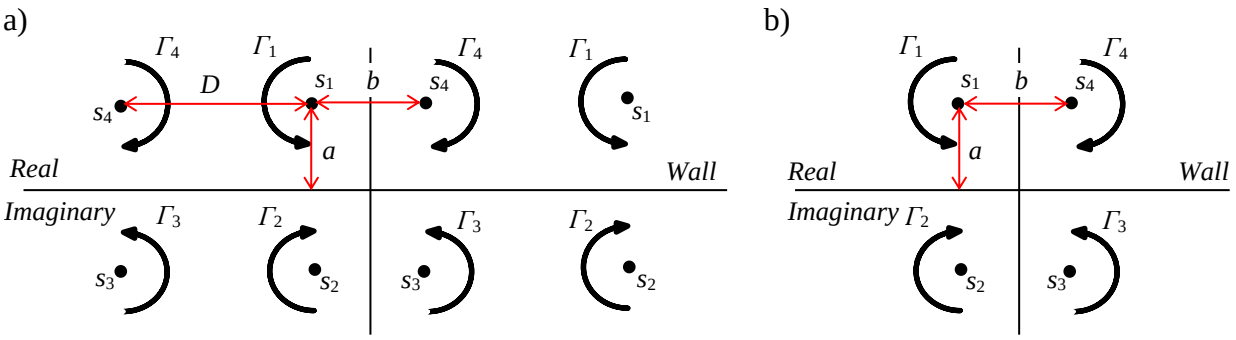

Fig. 21. Conceptual description of a) multiple CVPs and b) single CVP on a flat wall. The dashed lines indicate periodic boundary condition, reprinted with permission from ASME

For multiple CVPs at an equidistance of D as shown in Fig. 21a, the complex potential function, F(s), and its complex velocity, W(s), can be expressed as follows:

$$F(s) = \frac{-i\Gamma}{2\pi} log\left[sin\frac{\pi}{D}(s-s_1)\right] + \frac{i\Gamma}{2\pi} log\left[sin\frac{\pi}{D}(s-s_2)\right] \quad (10)$$
$$+ \frac{-i\Gamma}{2\pi} log\left[sin\frac{\pi}{D}(s-s_3)\right] + \frac{i\Gamma}{2\pi} log\left[sin\frac{\pi}{D}(s-s_4)\right]$$

$$F'(s) = \frac{dF}{ds} = \frac{-i\Gamma}{2D} cot\frac{\pi}{D}(s-s_1) + \frac{i\Gamma}{2D} cot\frac{\pi}{D}(s-s_2) \quad (11)$$
$$+ \frac{-i\Gamma}{2D} cot\frac{\pi}{D}(s-s_3) + \frac{i\Gamma}{2D} cot\frac{\pi}{D}(s-s_4)$$

where i is the imaginary unit, s is the complex coordinate ($s = b/2 + ia$), and Γ is vortex circulation. To simplify Eq. 11, $\zeta = {}^{2\pi a}/_{D}$ and $\xi = {}^{\pi b}/_{D}$ are introduced to replace a and b, respectively. By dividing the real part by the imaginary part of F'(s) in Eq. 11, the ratio of $d\xi$ and $d\zeta$ can be obtained as follows:

$$\frac{d\xi}{d\zeta} = -\frac{sin^2\xi}{\sinh^2\zeta} \quad (12)$$

where $\zeta = {}^{2\pi a}/_{D}$ and $\xi = {}^{\pi b}/_{D}$. By integrating the Eq. 12, the following equation can be obtained:

$$\text{cosec}^2\xi + \text{cosech}^2\zeta = C \quad (13)$$

where C is a constant. Equation 13 is used to determine the location of the CVP core coordinates.

The variations of ζ and ξ along the downstream were estimated by the equations derived by Jones [15] for multiple CVPs, as follows:

$$\frac{d\xi}{d\delta} = -\frac{\Gamma_0 tan^2\xi}{\sinh(2\zeta)\cdot(\tan^2\xi+\tanh^2\zeta)} \tag{14}$$

$$\frac{d\zeta}{d\delta} = -\frac{\Gamma_0 tanh^2\zeta}{\sinh(2\xi)\cdot(\tan^2\xi+\tanh^2\zeta)} \tag{15}$$

where, $\delta = {2\pi x}/{D}$, and $\Gamma_0 = {\Gamma}/{u_h D}$. u_h is the velocity of the undisturbed stream at the trailing edge of the VG at $y/\beta = 1$ and Γ_0 is dimensionless circulation. In the Jones model, Eqs.14 and 15 can be used to predict the path of the VG vortex along the streamwise direction.

The vortex strength, Γ_0, is estimated analytically based on the *lifting line theory* [15, 71]. Assuming a vortex is shed from the tip of the trailing edge of the VG, Γ_0 can be expressed as a function of inclination angle and coordinates of the trailing edge tip of the corresponding VG, as follows [15]:

$$\Gamma_0 = \frac{a_0}{\left(\frac{2}{c_L \cdot c_0}+A\right)} \tag{16a}$$

$$A = \frac{-\tanh^2\zeta_1}{sin\xi_1\left(\tan^2\frac{\xi_1}{2}+\tanh^2\zeta_1\right)} \tag{16b}$$

where a_0 is the inclination angle of the VG, c_L is the lift slope, c_0 is the dimensionless chord of the VG ($c = c/D$, L is a chord of the VG, D is an equidistance between potential vortices), ξ_1 and ζ_1 are the dimensionless coordinates of y and z for the trailing edge tip of a VG. However, the assumption that a vortex could be shed from the trailing edge tip (ξ_1 and ζ_1) is not applicable for the triangular VG due to the zero width of the trailing edge ($\xi_1 = 0$). Therefore, the initial locations of the vortices (ξ_1 and ζ_1) were obtained from experimental data, which were measured at $x/\beta = 0.2$. Table 4 shows the experimental results of a and b measured at $x/\beta = 0.5$ for

$\zeta_1 = {2\pi a}/{D}$ and $\xi_1 = {\pi b}/{D}$ in Eq. 16b. It is important to note that the trailing edge of the VGs always pointed downstream and, as a result, the vortices rotated in the opposite direction, when compared to the cases considered by Jones [15] because of the VGs azimuthal orientation.

Table 4. Vortex core locations measured via smoke visualization, reprinted with permission from ASME

VG Type	Initial vertical location from the wall, *a* [mm](1)	Initial horizontal separation distance, *b* [mm](1)	Final horizontal separation distance, b [mm](2)	Asymptotic solution of *b*, b_∞ [mm](3)
VG-A	10.4	21.2	17.81	15.74
VG-B	9.6	16	13.32	12.39
VG-C	10.1	12.3	11.35	11
VG-D	8	9.7	8.93	8.64

Notes:
(1) Experimental value found at x/β of 0.2
(2) Experimental value found at x/β of 2.0
(3) At x/β of 2.0 using Eq. 22

In order to estimate the paths of CVP cores induced by a single VG, an analytical solution was also developed for single potential CVP based on 2D potential flow theory, as shown in Fig. 20b. For a single CVP, the complex potential function, *F*(s), and its complex velocity, *W*(s), are expressed as follows [70, 71]:

$$F(s) = \frac{-i\Gamma}{2\pi}\log(s - s_1) + \frac{i\Gamma}{2\pi}\log(s - s_2) + \frac{-i\Gamma}{2\pi}\log(s - s_3) + \frac{i\Gamma}{2\pi}\log(s - s_4) \quad (17)$$

$$F'(s) = \frac{dF}{ds} = \frac{-i\Gamma}{2\pi}\frac{1}{s-s_1} + \frac{i\Gamma}{2\pi}\frac{1}{s-s_2} + \frac{-i\Gamma}{2\pi}\frac{1}{s-s_3} + \frac{i\Gamma}{2\pi}\frac{1}{s-s_4} \quad (18)$$

The location of the induced vortex as a function of time is obtained as follows:

$$\frac{ds}{dt} = \overline{u - iv} = \overline{F'(s)} \tag{19a}$$

$$\frac{ds}{dt} = \frac{d}{dt}\left(\frac{b}{2} + ia\right) = \frac{d}{dt}\left(\frac{b}{2}\right) + i\frac{da}{dt} \tag{19b}$$

where $\overline{F'}$ is the complex conjugate of F'. The path of a single CVP along the downstream is obtained in terms of coordinates a and b by solving Eq. 19.

CVP path based on Pseudo-Viscous Flow Model

The Jones' approach neglects viscous effects and vortex circulation (Γ_0 in Eq. 16a) is assumed to be constant as the vortices develop along the axial distance. Therefore, Habchi *et al.* [16] used the pseudo-viscous model proposed by Lögdberg *et al.* [17] for an array of trapezoidal VGs in a circular pipe to predict the path of CVP. Lögdberg *et al.* basically modified Jones model [15] based on their own experimental results measured at Re ≈ 1.7x10^6. Habchi *et al.* changed the values of the parameters in the Lögdberg model based on their own numerical results at Re = 15,000.

The approach postulated by Lögdberg *et al.* [17] takes into account the exponential decay of circulation of vortex (Γ_0 in Eq. 16a) along the axial direction. Furthermore, they found that the value of C converges to an asymptotic value based on three-component hot-wire experiments. Therefore, the pseudo-viscous model [17] takes into account the variation of the value of C (Eq. 13) along the axial direction. In the present study of smoke visualization, the incoming flow was laminar (Re = 1965, with Re based on the hydraulic diameter) and the dimensions and shapes of the VGs were different from the ones in other studies [16, 17]. Therefore, the Γ_0 and C equations in the pseudo-viscous model were modified, as follows:

$$A(\delta) = A_0 exp[-\sigma_1(\delta - \delta_0)] \quad (20)$$

$$C(\delta) = C_\infty + (C_0 - C_\infty) exp[-\sigma_2(\delta - \delta_0)] \quad (21)$$

where σ_1 and σ_2 are exponential decay constants, C_0 and δ_0 are the initial values of C and $\delta = {}^{2\pi x}/_{D}$, respectively. C_∞ is the parameter C determined at x/β = 2.0. Table 5 shows the values of the VG parameters for Eqs. 20 and 21 for each VG. The initial and final values of a and b in the modified pseudo-viscous model (Eqs. 20 and 21) were obtained from the experimental data at x/β = 0.2 and x/β = 2.0, as shown in Table 5. In summary, the modified pseudo-viscous model in Eqs. 20 and 21 were used to determine the location of the CVP cores analytically. The ability of the modified model on predicting the path of CVP was corroborated by comparing the analytical solutions with the smoke visualization results and the other analytical models (i.e. Jones model, Habchi model, and Lögdberg model) as shown in the next section.

Table 5. VG parameters in the modified pseudo-viscous model (Eq. 20 and Eq. 21), reprinted with permission from ASME

VG Type	C_0(1)	C_∞(2)	A_0(3)	δ_0(4)	$\sigma_1$5)	σ_2 (6)
VG-A	1.71	1.7	0.24	0.26	0.03	1.12
VG-B	1.67	1.78	0.25	0.32	0.02	0.04
VG-C	1.52	1.53	0.24	0.39	0.01	0.05
VG-D	1.43	1.45	0.26	0.51	0.02	0.04

Notes:
(1) At x/β of 0.2 using Eq. 13
(2) At x/β of 2.0 using Eq. 13
(3) At x/β of 0.2 using Eq. 20
(4) $\delta = {}^{2\pi x}/_{D}$ at x/β of 0.2
(5) Found by data fitting Eq. 20
(6) Found by data fitting Eq. 21

4.3 Path of CVP Cores*

The path of the CVP cores was measured by identifying the location of the CVP cores from smoke visualization images. The CVP vertical core distance, a, and the horizontal separation distance, b, were measured at different axial distance as shown in Fig. 5, within the stability region. The experimental measurements were compared with the analytical solutions (i.e. the modified pseudo-viscous model, Jones model, Habchi model, and Lögdberg model).

Figure 22 shows the path of CVP induced by the rectangular tab (VG-A) in terms of a and b as predicted by Eqs. 13 and 19, and the experimental data. As Fig. 22 shows, the initial a/β and b/β (0.6 and 1.25) for the analytical solutions (Eqs. 13 and 19) were obtained from the experimental values of a and b at x/β of 0.2. Figure 22 shows that Jones model (Eq. 13) for multiple CVPs converges to the single CVP case (Eq. 19) when D is equal or greater than 3 times l_{50} (Table 2). Therefore, D in the Jones model was set as 3 l_{50} to predict a CVP induced by a single trapezoidal VGs. The figure also shows a good agreement between the experimental and analytical results within the stability region ($x/\beta < 2$), which suggest that the inviscid approximation is reasonable. The results also reveal that vortex separation (b) decreases while the vertical distance (a) increases along the duct length.

*Part of the data reported in this chapter is reprinted with permission from "Characterization of Tab-Induced Counter-Rotating Vortex Pair for Mixing Applications" by Park *et al.*, 2016, *Journal of Basic Engineering*, 139(3), 031102, Copyright [2016] by ASME

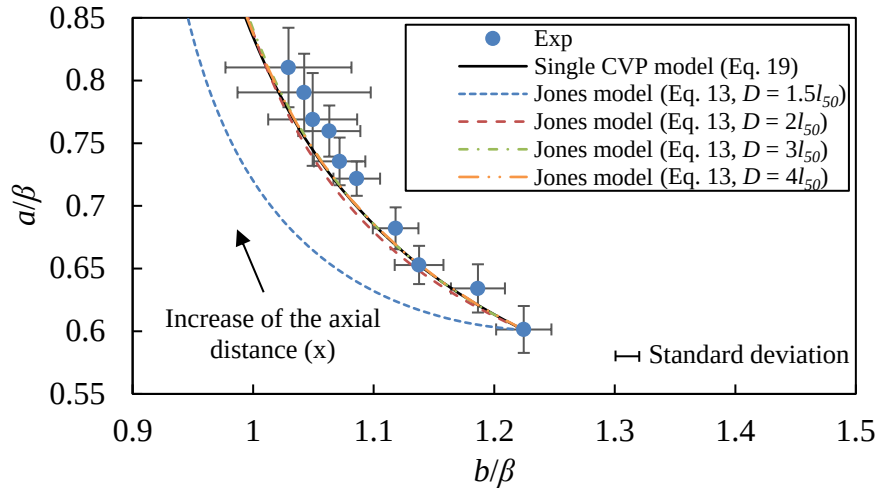

Fig. 22. Vortex core locations in the spanwise (y-z) plane along the axial distance (x) for VG-A ($\phi = 0°$), reprinted with permission from ASME

The coordinates of the CVP cores in the spanwise plane as a function of x/β were predicted using the modified pseudo-viscous model (Eqs. 20 and 21). The results were compared with the experiments, Jones, Habchi, and Lögdberg models, as shown in Fig. 23. The modified pseudo-viscous model fit the experimental results better than the other models. As a matter of fact, C_0 in the modified pseudo-viscous model correlates well with the taper angle and aspect ratio of the trapezoidal VGs, as shown in Fig. 24. As taper angle (or aspect ratio) increases, C_0 decreased linearly. However, it is not straightforward to infer a relation between the exponential decay constants (σ_1 and σ_2) in the model and the VG geometric factors. This may imply that those parameters are not solely dependent on the VG geometries, but also on flow characteristics.

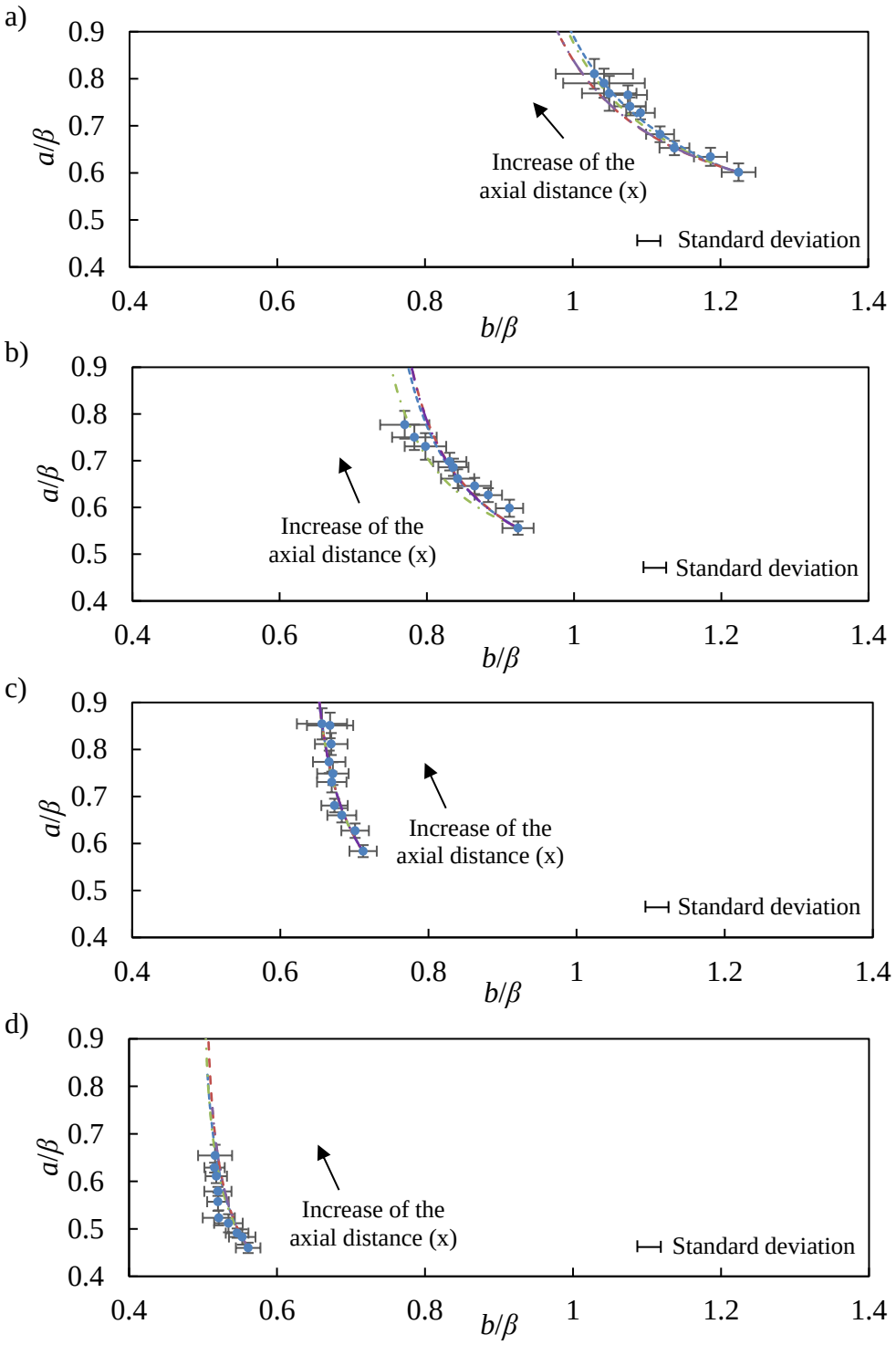

Fig. 23. Projection of the vortex path on the y-z plane along the axial distance (x) for a) VG-A (ϕ = 0°), b) VG-B (ϕ = 7.6°), c) VG-C (ϕ = 13.5°), and d) VG-D (ϕ = 19.3°), reprinted with permission from ASME:
● Experiment, Modified model (Eqs. 20, 21), Jones Model (Eq. 13), Habchi model [16] Lögdberg model [17]

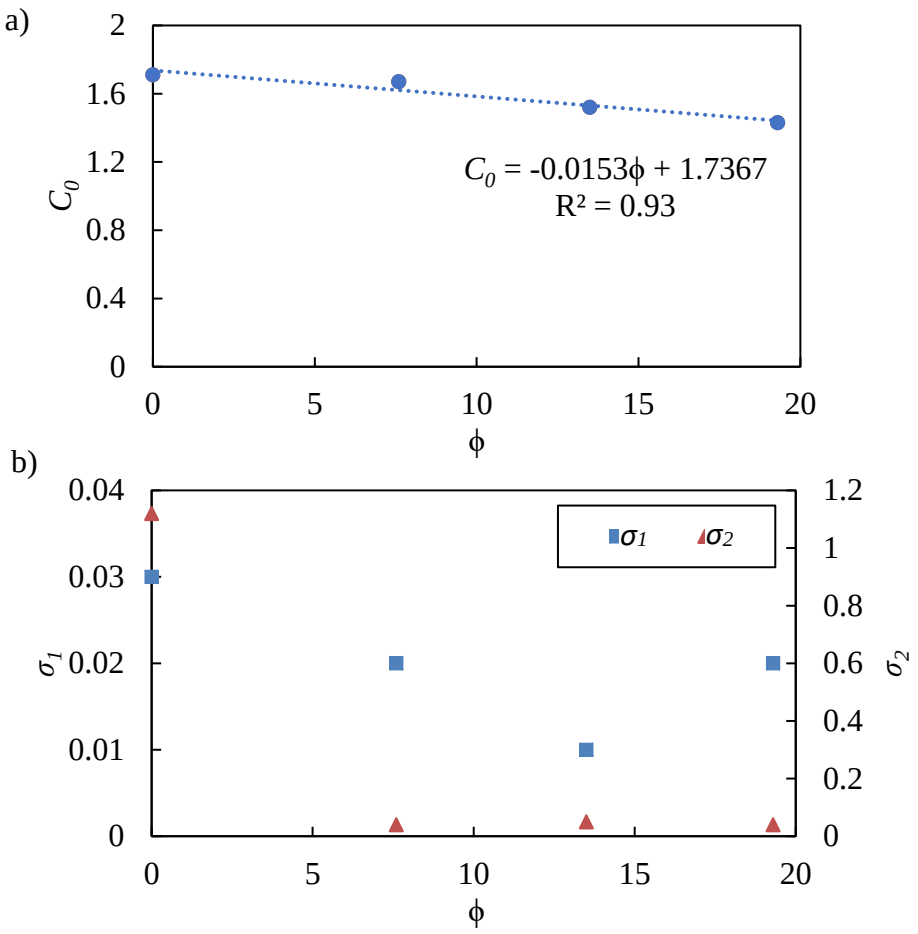

Fig. 24. Variation of the parameters in the modified pseudo-viscous model for different taper angle of trapezoidal VGs: a) C_0 in Eq. 20, b) σ_1 and σ_2 in Eqs. 20 and 21

The vortex core locations of *a* and *b* along the axial distance (x) are shown in Fig. 25 and Fig. 26, respectively. Figure 25 shows how the CVPs core shift vertically as they move downstream while Fig. 26 reveals that the normalized horizontal separation distance b/β approaches b_∞/β asymptotically. The b_∞ can be obtained by letting $a \rightarrow \infty$ in Eq. 13, and is given by:

$$b_\infty = \frac{D}{\pi}\left[\sin^{-1}\left(\sqrt{\frac{1}{C_\infty}}\right)\right] \tag{22}$$

where *D* was assumed to be 3 times l_{50}, as explained above. The values of b_∞ for different VGs are shown in Table 4. Figure 26 also shows that *b* decreases as the taper angle increases. As Table 2 shows, l_{50} also decreases when taper angle increases, which suggest that l_{50} can be directly related to *b*. On the other hand, Fig. 25 shows that the linear behavior of *a* along the axial distance does not change significantly with taper angle (ϕ), since, inclination angle (θ) was the same for all the cases.

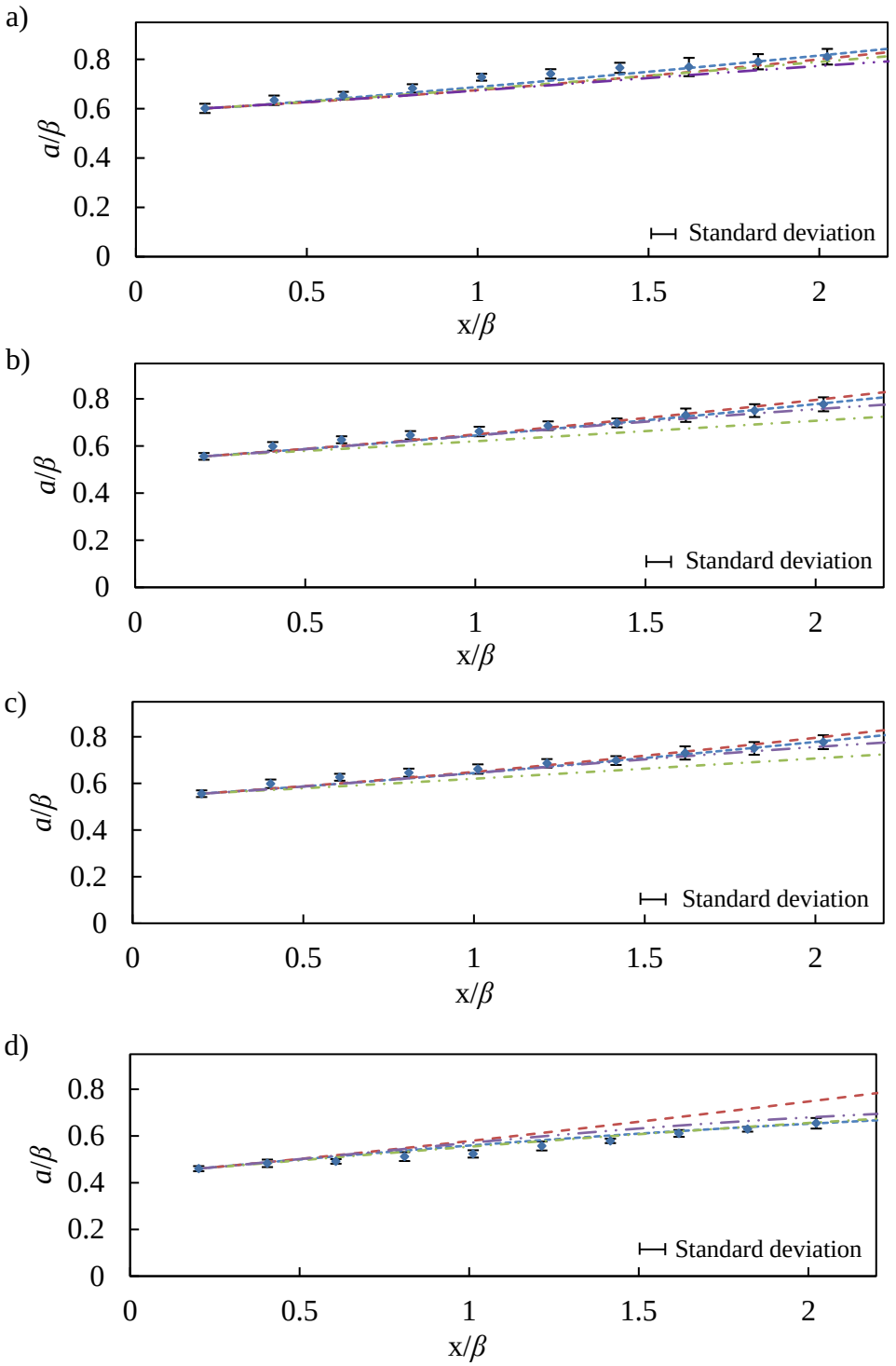

Fig. 25. Vertical locations of the vortex core (*a*) along the axial distance (x) for a) VG-A (ϕ = 0°), b) VG-B (ϕ = 7.6°), c) VG-C (ϕ = 13.5°), and d) VG-D (ϕ = 19.3°), reprinted with permission from ASME:
● Experiment, ····· Modified model (Eqs. 20, 21), - - - Jones Model (Eq. 13), -·-· Habchi model [16] —·— Lögdberg model [17]

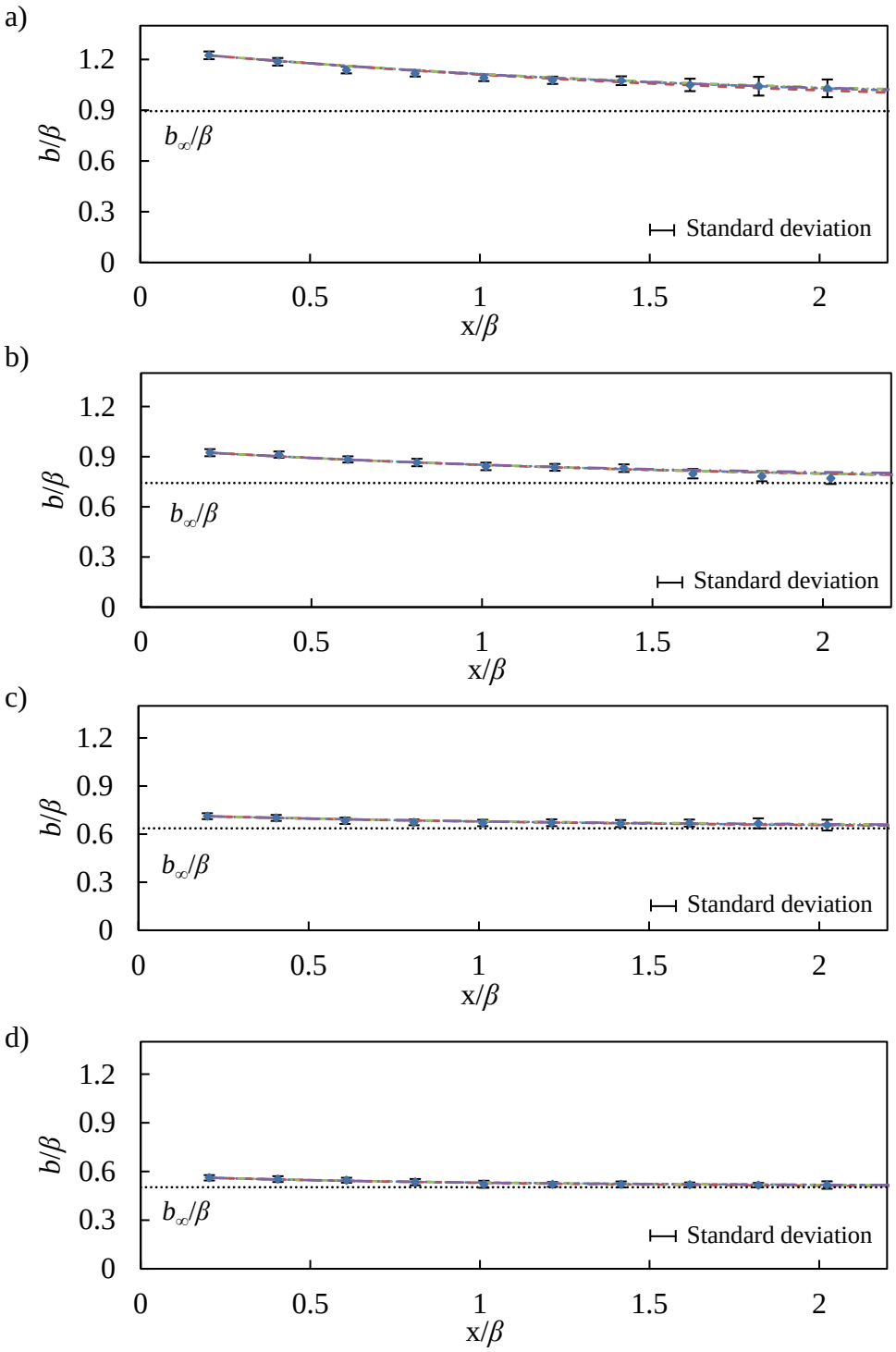

Fig. 26. Horizontal separation distances of the vortex cores along the axial distance (x) for a) VG-A (ϕ = 0°), b) VG-B (ϕ = 7.6°), c) VG-C (ϕ = 13.5°), and d) VG-D (ϕ = 19.3°), reprinted with permission from ASME:
● Experiment, ····· Modified model (Eqs. 20, 21), - - - Jones Model (Eq. 13), -·-·- Habchi model [16] — ·· — Lögdberg model [17]

4.4 Particle Image Velocimetry (PIV) Results

PIV analysis was conducted to measure velocity of the flow in the wake of trapezoidal VGs. For the single VG cases, the large VGs used in smoke visualization study were employed. However, for the multiple VG cases, the size of the VGs was reduced so that multiple (three or more) VGs can be placed within the limited width of the duct. Furthermore, the influence by the side walls on the coherent flow was minimized with the small-scaled VGs when multiple VGs were employed. Therefore, the sizes of trapezoidal VGs were 55% smaller than the ones used in the single VG study. Table 3 shows the details of geometric factors of VGs used in PIV analysis.

PIV measurement validation

In the PIV experiments, air was seeded with smoke particles, which flowed through a straight square duct at a Reynolds number of 4800 based on hydraulic diameter. Multiple honeycomb structures and turbulators were employed to promote fully developed turbulent flow at the inlet of the duct as described in the previous chapter. For validation of the PIV system, PIV experiments were conducted in the absence of VG (baseline case). The sampling rate was set to 3000 fps with a resolution was 45 μm/px. The flow field was recorded for 3.6 seconds and the corresponding 5000 frames of the PIV recording were used for data processing by using PIVLab. Two interrogation windows of sizes 64 x 64 and 32 x 32 pixels were used for data processing with a 50% overlap with the neighboring interrogation regions.

Figure 27 shows the mean velocity profile in the streamwise direction (U) of the baseline (no VG) case, scaled using U_0 and $0.5D_h$, where U_0 is the streamwise velocity at the center of the duct and $0.5D_h$ is the half of hydraulic diameter. The streamwise velocity was measured in the center plane (z/l = 0 mm) at the entrance of the test section (i.e. 2.75 m downstream from the

honeycombs and turbulators of the duct inlet). Figure 27 also includes velocity measurements from other studies under similar conditions [73, 74] for comparison purposes. Gavrilakis [73] and Niederschulte [74] studied fully developed turbulent flows at low Reynolds numbers in a straight square duct at Re ≈ 4410 and 4915, respectively. As shown in Fig 27, the agreement between the present study and the references is excellent, which implies that the flow in the test section is fully developed turbulent flow.

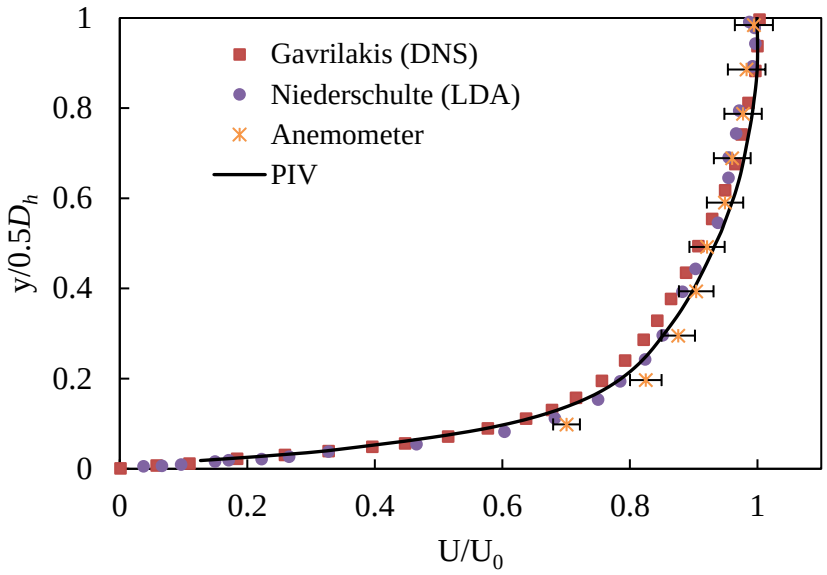

Fig. 27. Time-averaged streamwise velocity profile at the inlet of the test section in absence of VG, scaled with outer variable U_0

To further confirm the flow development in the present study, the mean streamwise velocity profile was scaled with inner variables y^+ and u^+, as shown in Fig. 28. The inner variables are defined as follows:

$$y^+ = \frac{yu_\tau}{\nu} \tag{23}$$

$$u^+ = \frac{u}{u_\tau} \tag{24}$$

where $u_\tau = \sqrt{\frac{\tau_w}{\rho}}$ is the friction velocity, $\tau_w = \mu \frac{\partial U}{\partial y}$ is the wall shear stress, and ρ is density of air. The velocity gradient for the wall shear stress (τ_w) was estimated by curve-fitting and using the last three data points next to the wall [26].

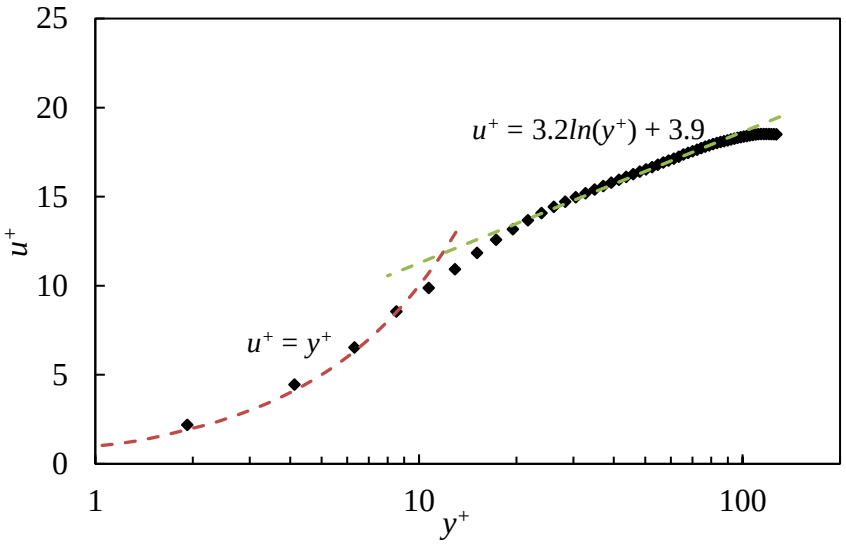

Fig. 28. Time-averaged streamwise velocity profile at the inlet of the test section in absence of VG, scaled with inner variables y^+ and u^+

The logarithm region in the u_τ-scaled profile follows a relation $u^+ = 3.2 \ln(y^+) + 3.9$ over the range $30 < y^+ < 100$, which was suggested by Gavrilakis [73] for low-Reynolds-number turbulent flows in a straight square duct. Therefore, the flow in the test section was considered as fully developed. Moreover, the results also indicate that the PIV technique provides accurate data.

The flow statistics were obtained by computing the root-mean-square (rms) value of the velocity fluctuation components. The rms velocity represents fluctuating motion of turbulent flow, i.e. turbulent intensity [75, 76], and can be obtained as follows:

$$u_{rms} = \sqrt{\frac{1}{N-1}\sum(u')^2} \quad (25)$$

where u = U + u′, U is the mean velocity, u′ is its fluctuating component, and *N* is the number of frames used for data processing. Furthermore, the time-averaged primary Reynolds stress ($-\overline{u'v'}$) was also computed for the PIV system validation purposes as follows:

$$-\overline{u'v'} = -\sqrt{\frac{1}{N-1}\sum(u'v')} \quad (26)$$

where u′ and v′ are fluctuating velocity in the streamwise and vertical directions, and *N* is the number of frames used for data processing. Reynolds stress represents turbulent convective mometum created by unsteady turbulent motion associated with velocity fluctuations [75, 76]. For flow statistics, 5000 frames of the PIV recording were used for data processing. In addition, two interrogation windows of sizes 128 x 128 and 64 x 64 pixels were used with a 50% overlap with the neighboring interrogation regions. The rms velocities (u_{rms} and v_{rms}) were scaled with the friction velocity (u_τ) and the primary Reynolds stress ($-\overline{u'v'}$) was scaled with the rms velocities (u_{rms} and v_{rms}), as shown in Figs. 29 and 30, respectively. The rms velocities and the primary Reynolds stress from Gavrilakis [73] and Niederschulte [74] who studied fully developed turbulent flows in a straight square duct at Re ≈ 4410 and 4915 were compared with the current results for validation purposes.

As shown in Fig. 29a, the peak value of u_{rms} was found near the wall or at y/0.5D_h of 0.1. The corresponding y^+ value was 11, which is in the middle of the buffer layer ($5 < y^+ < 30$). It has been found that the production of turbulence reaches a maximum in the buffer layer due to the acceleration of the flow [75, 76]. The variations of v_{rms} and $-\overline{u'v'}$ also fall within the reference data, as shown in Fig. 29b and Fig. 30. Therefore, the flow statistics data also suggest that the rms velocity and Reynolds stress measurements from the PIV system are reasonable and

accurate. In addition, it also indicates that the flow in the test section can reach fully developed turbulent conditions.

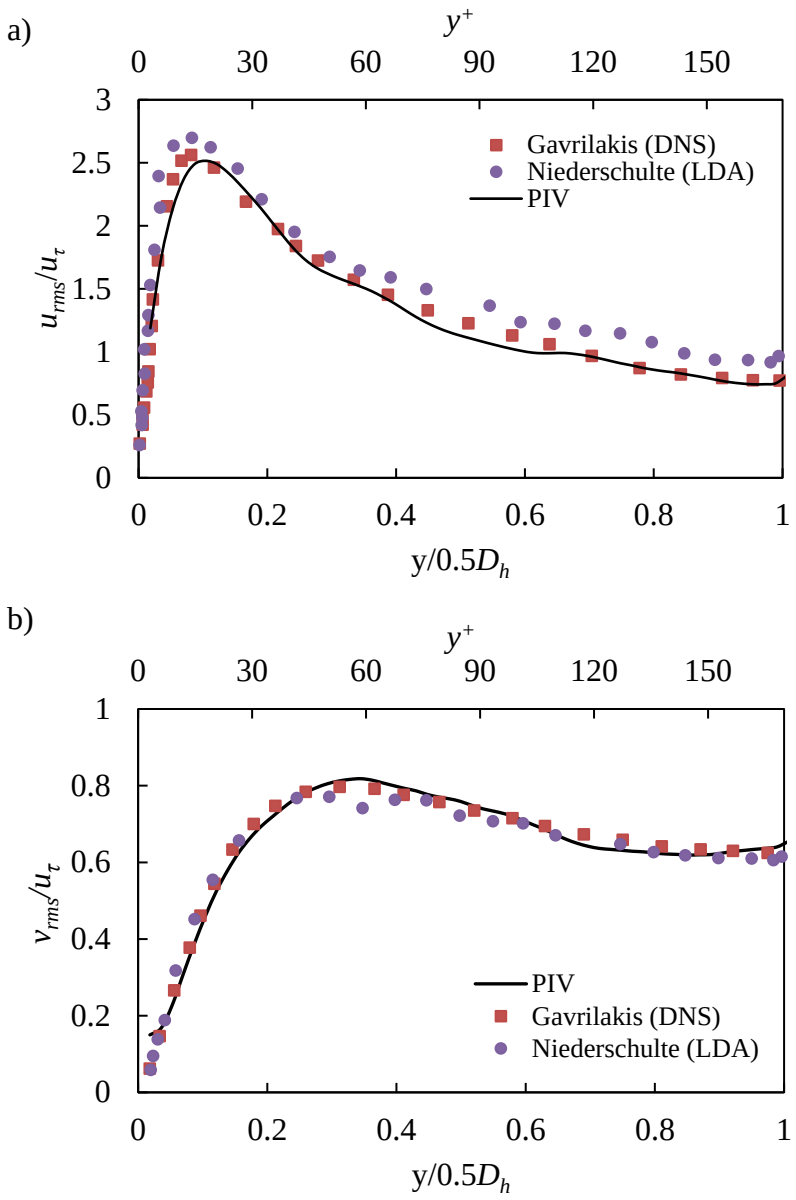

Fig. 29. Root-mean square values of velocity fluctuation components of the a) streamwise velocity and b) vertical velocity at the inlet of the test section in absence of VG, scaled with friction velocity u_τ

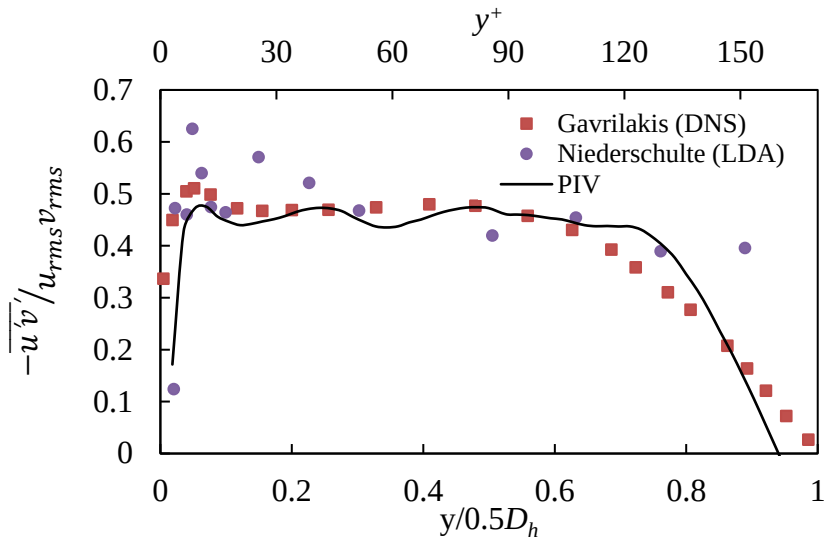

Fig. 30. Primary Reynolds stress $-\overline{u'v'}$ at the inlet of the test section in absence of VG, scaled with product of the rms velocities u_{rms} and v_{rms}

Flow characteristics with variable inclination angle and taper angle of single VGs

Single VGs with different taper and inclination angles (Table 3) were used to obtain velocity profiles of the flow in the wake of the VGs. The mean velocities of the coherent flow induced by trapezoidal VGs were measured in the spanwise plane (y-z) at x/β = 0.5 by using the PIV system. The streamlines with the velocity vectors were also determined for each case as shown in Fig. 31. As shown in Fig. 31, all tested VGs induced a counter-rotating vortex pair (CVP) with the common-up flow in the middle of the CVP itself. The vortex cores were observed at a lower vertical location of y/β at higher inclination angles (θ). The streamlines with the velocity vectors of the CVP suggest that the CVP can transport the fluid near the wall into the freestream and also entrain fluid from the free stream into the wall region. As a result, the convective process can be enhanced under this condition. In addition, it was observed that the transverse velocities were weakened and lead to the formation of a dead zone near the wall (y/β < 0.3) in the middle of the CVP (-0.2 < z/l < 0.2), as shown in Fig. 31.

It has been suggested that there is a relation between the streamwise vorticity and the convective heat transfer (Nusselt number) in the wake of VGs [29, 77]. Therefore, streamwise vorticity (ω_i) was calculated for each case based on the mean spanwise velocity (W) and mean vertical velocity (V) measured at x/β = 0.5. The vorticity (ω) is a measure of local rotation of the fluid, which is defined as the curl of the velocity vectors as shown below.

$$\boldsymbol{\omega} = \nabla \times \mathbf{u} = \left(\frac{\partial W}{\partial y} - \frac{\partial V}{\partial z}\right)\hat{i} + \left(\frac{\partial U}{\partial z} - \frac{\partial W}{\partial x}\right)\hat{j} + \left(\frac{\partial V}{\partial x} - \frac{\partial U}{\partial y}\right)\hat{k} \tag{25a}$$

$$\omega_i = \frac{\partial W}{\partial y} - \frac{\partial V}{\partial z} \tag{25b}$$

where U, V, and W are the mean velocities in x, y, and z directions, respectively. $\hat{i}, \hat{j}$, and $\hat{k}$ are the unit vectors in x, y, and z direction, respectively.

Figure 32 shows the time-averaged streamwise vorticity (ω_i) measured in the spanwise plane (y-z) at x/β = 0.5. The vorticty (ω_i) was nondimensionalized with VG height (β) and the mean velocity at the duct center (U_0) in order to consider the physical geometry of the VG and flow condition. Figure 32 shows that the streamwise vorticity was intense near the wall for all tested cases. Furthermore, greater streamwise vorticity was observed at higher inclination angle, especially near the wall. However, the magnitudes of the streamwise vorticity were not significantly affected by taper angle.

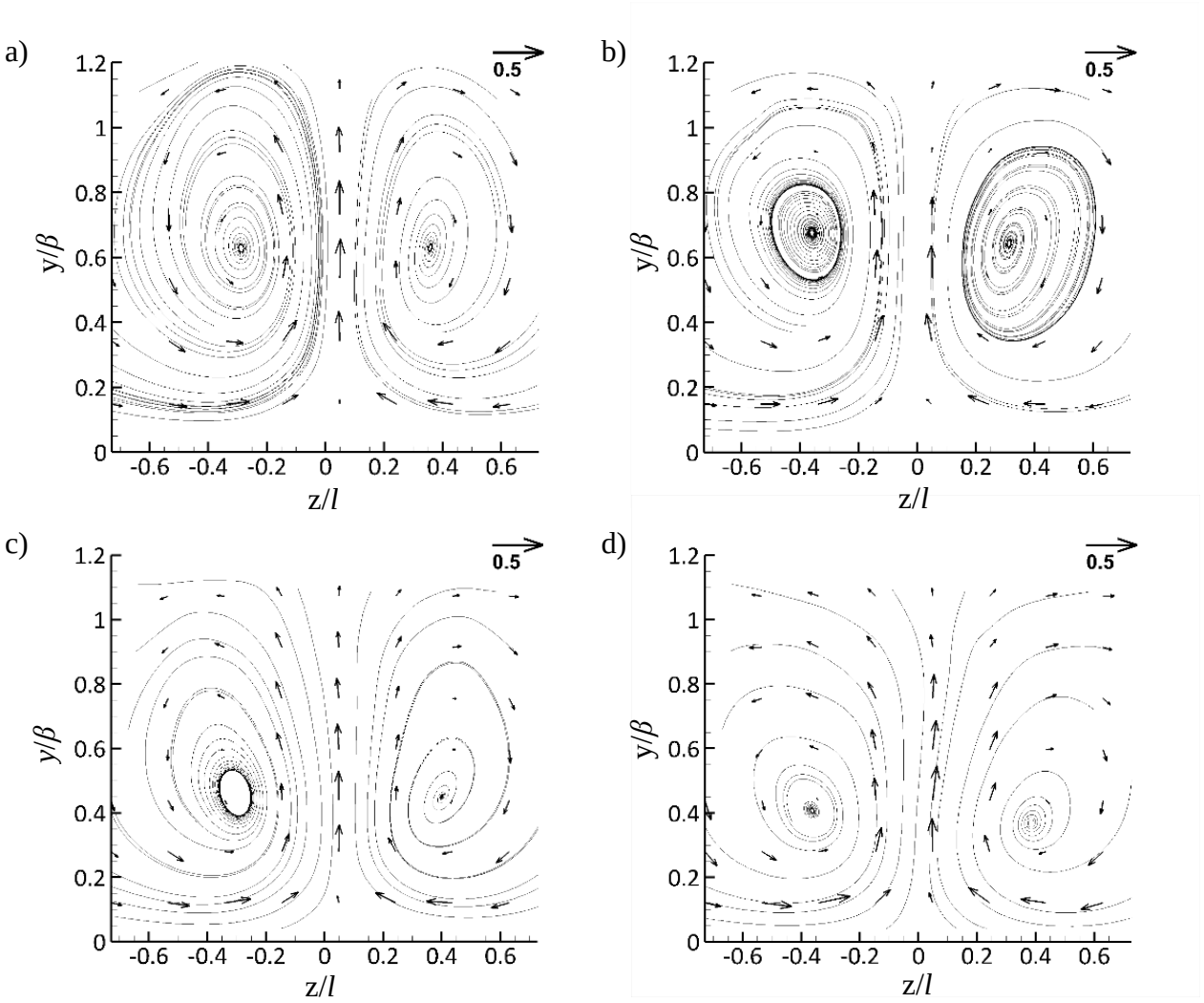

Fig. 31. Time-averaged streamlines with velocity vectors in the spanwise plane (y-z) at x/β = 0.5 for a) trapezoidal VG (ϕ = 7.6°) at θ = 45°, b) rectangular VG (ϕ = 0°) at θ = 45°, c) trapezoidal VG (ϕ = 7.6°) at θ = 60°, and d) rectangular VG (ϕ = 0°) at θ = 60°

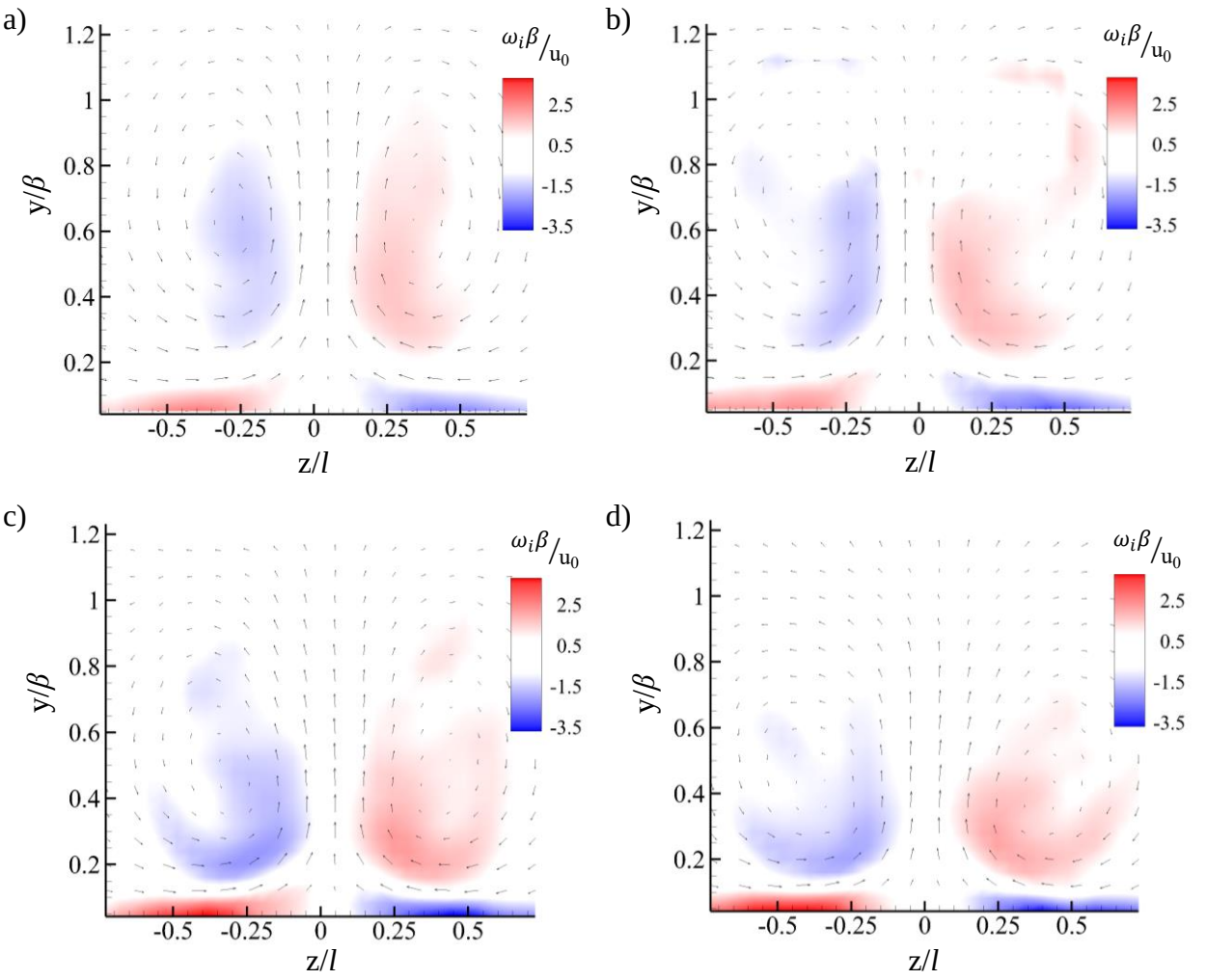

Fig. 32. Time-averaged streamwise vorticity in the spanwise plane (y-z) at x/β = 0.5 for a) trapezoidal VG (ϕ = 7.6°) at θ = 45°, b) rectangular VG (ϕ = 0°) at θ = 45°, c) trapezoidal VG (ϕ = 7.6°) at θ = 60°, and d) rectangular VG (ϕ = 0°) at θ = 60°

According to the argument made by Chang *et al.* [77], greater heat transfer rates on the wall would be expected for the VG with higher inclination angle due to the stronger streamwise vorticity. However, Habchi *et al.* [29] concluded that vorticity flux was not the only contributing factor for convective heat transfer and must consider other characteristics of the vortex structure. In addition, Lemenand *et al.* [35] also found that the streamwise vorticity flux and Nusselt number behaved in a different way as the CVP developed along the downstream. Therefore, the effect of trapezoidal VGs on heat transfer will be discussed in the later section of this work,

considering shear rates $\left(\dot{\gamma}_w = {\partial U}/{\partial y}\Big|_w\right)$ and turbulence near the wall rather than just accounting for vorticity [79-81].

The time-averaged velocities of the coherent flow induced by single VGs were measured in the streamwise plane (x-y) to investigate the common-up flow and down flow regions by using the PIV system. The trailing edge of VG was located at x/β of 0. Figure 33 shows the mean streamwise velocity (U) profiles measured in the common-up flow region in between of the CVP itself (i.e. z/l = 0, the center plane). In the common-up flow region, it was found that the vortices induced inflectional velocity profiles in the wake of VGs for all tested cases. The inflectional velocity profiles became flatten or approached the no-VG velocity profile as the flow developed along the downstream. This suggests that the strength of circulation of the CVP decreased along the downstream due to viscous dissipation [26, 78]. At higher inclination angle, the inflectional velocity profiles became flatten or approached the no-VG velocity profile at a shorter axial distance of x/β, which implies that the CVP decayed faster. Furthermore, strong negative streamwise velocities in the vicinity of the VGs were observed, especially at higher inclination angle. This implies that stronger recirculation flows were generated at the bottom corner of the VGs at higher inclination angle [16]. However, taper angle of VGs had minor effect on the velocity profile in the common-up flow region.

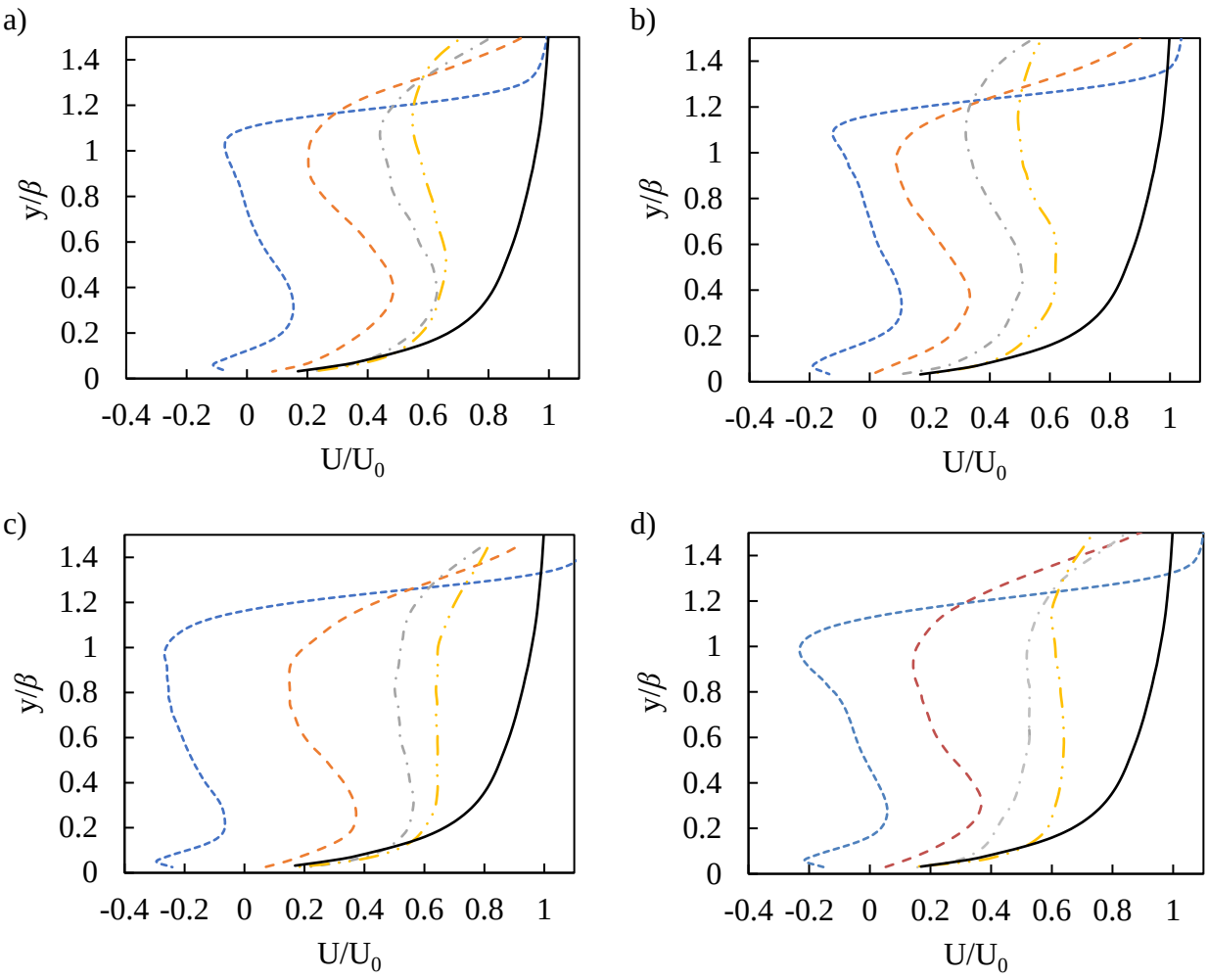

Fig. 33. Time-averaged streamwise velocity profiles measured in the common-up flow region (z/l = 0, center plane) for a) trapezoidal VG (ϕ = 7.6°) at θ = 45°, b) rectangular VG (ϕ = 0°) at θ = 45°, c) trapezoidal VG (ϕ = 7.6°) at θ = 60°, and d) rectangular VG (ϕ = 0°) at θ = 60°: x/β = 0.5, x/β = 1.5, x/β = 2.5, x/β = 3.5, no VG

Figure 34 shows the mean vertical velocity (V) profiles in the common-up flow region (z/l = 0, center plane) for the rectangular (ϕ = 0°) and trapezoidal (ϕ = 7.6°) VGs at different inclination angles. Figure 34 indicates that the magnitudes of vertical velocities decreased as inclination angle increased. It has been known that higher vertical velocity implies higher circulation strength of the vortices [10, 14, 78]. Therefore, Fig. 34 indirectly suggests that the VGs at lower inclination angle produced CVP with stronger circulation. This is a consistent

observation based on the streamwise velocity profiles shown in Fig. 33, which indicate that the CVP lasted for a longer axial distance of x/β at lower inclination angle.

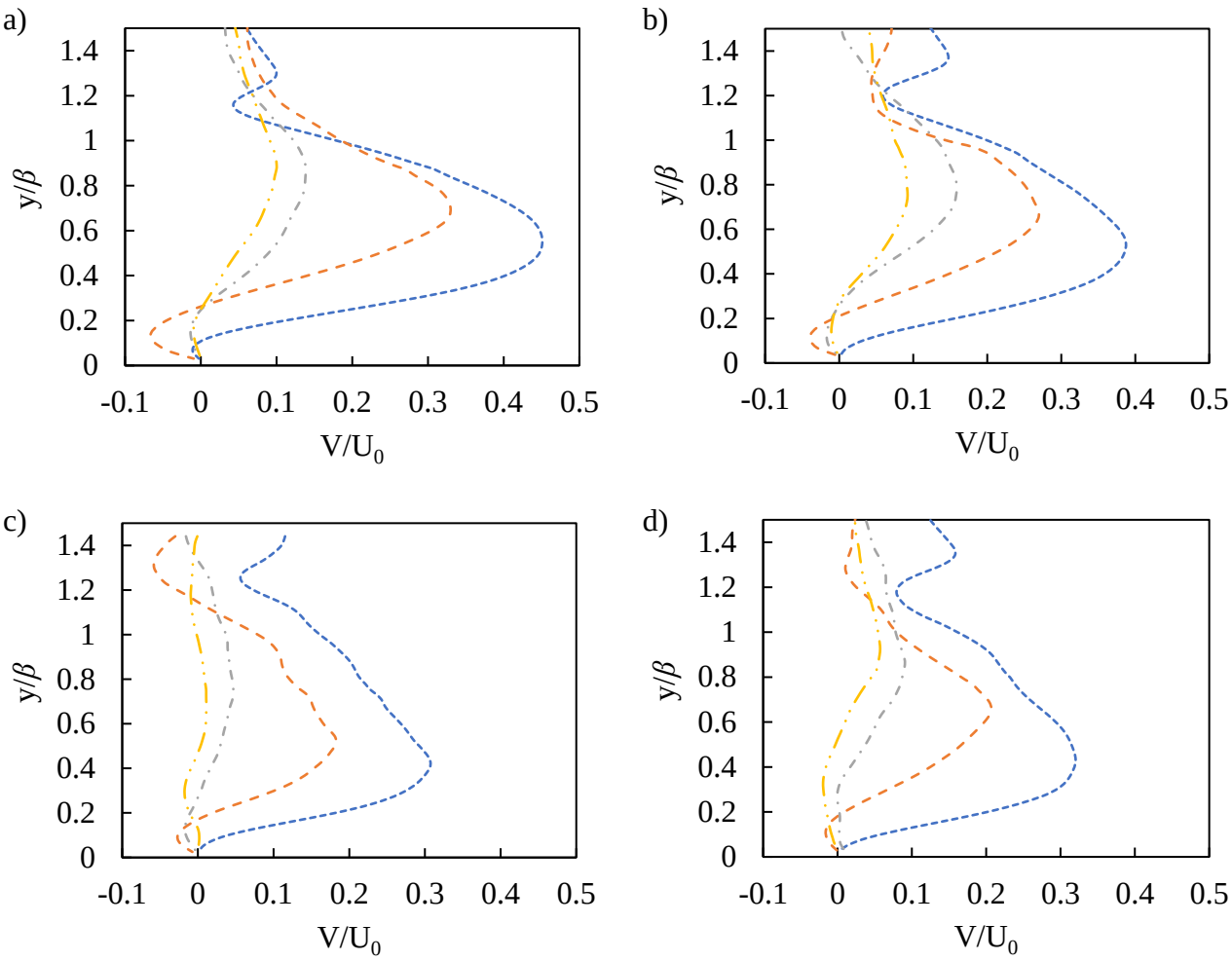

Fig. 34. Time-averaged vertical velocity profiles measured in the common-up flow region (z/l = 0, center plane) for a) trapezoidal VG (ϕ = 7.6°) at θ = 45°, b) rectangular VG (ϕ = 0°) at θ = 45°, c) trapezoidal VG (ϕ = 7.6°) at θ = 60°, and d) rectangular VG (ϕ = 0°) at θ = 60°: x/β = 0.5, x/β = 1.5, x/β = 2.5, x/β = 3.5

Figure 35 shows the mean streamwise velocity (U) profiles measured in the down flow region on the outer-side of the CVP (i.e. z/l = 0.7). It was found that the flow was accelerated in the streamwise direction due to the induced vortical structure, especially near the wall. Also, as

inclination angle increased, the flow was also accelerated. In general, the effect of the vortices on the acceleration of flow near the wall became insignificant after x/β = 1.5, as shown in Fig. 35. Furthermore, the rectangular VG (ϕ = 0°) generated a more vigorous inflectional velocity profile in the vicinity of the VG (i.e. x/β = 0.5) due to the wide width of the trailing edge.

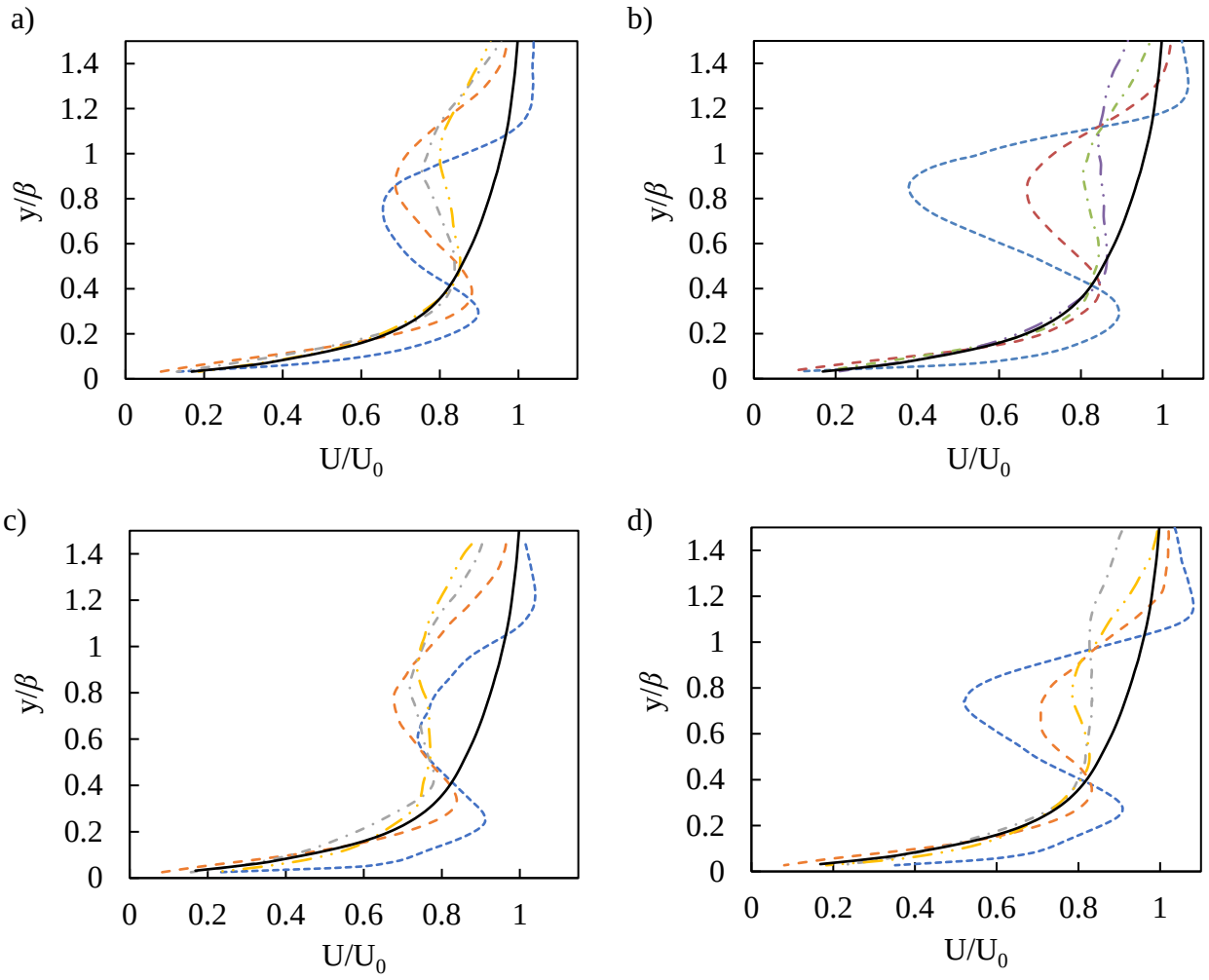

Fig. 35. Time-averaged streamwise velocity profiles measured in the down flow region (z/l = 0.7) for a) trapezoidal VG (ϕ = 7.6°) at θ = 45°, b) rectangular VG (ϕ = 0°) at θ = 45°, c) trapezoidal VG (ϕ = 7.6°) at θ = 60°, and d) rectangular VG (ϕ = 0°) at θ = 60°: x/β = 0.5, x/β = 1.5, x/β = 2.5, x/β = 3.5, no VG

Figure 36 shows the mean vertical velocity (V) profiles in the down flow region (z/l = 0.7) for rectangular ($\phi = 0°$) and trapezoidal ($\phi = 7.6°$) VGs at different inclination angles. As shown in Fig. 36, stronger downward velocity was generated by VGs at lower inclination angle. This also suggests that stronger circulation of the CVP was generated at lower inclination angle. However, taper angle did not have a significant effect on the mean vertical velocities.

By comparing Figs. 34 and 36, it was found that the magnitude of the upward velocities in the middle of the CVP ($z/l = 0$, Fig. 34) was twice as large as the magnitude of downward velocities on the outer-side of the CVP ($z/l = 0.7$, Fig. 36) approximately. This suggests that interaction of the counter-rotating vortices led to the CVP being elevated along the downstream direction by generating a strong upward momentum in the middle of it. As a result, the locations of the peak of the streamwise and vertical velocities shifted up vertically along the downstream, as shown in Figs. 34 and 36.

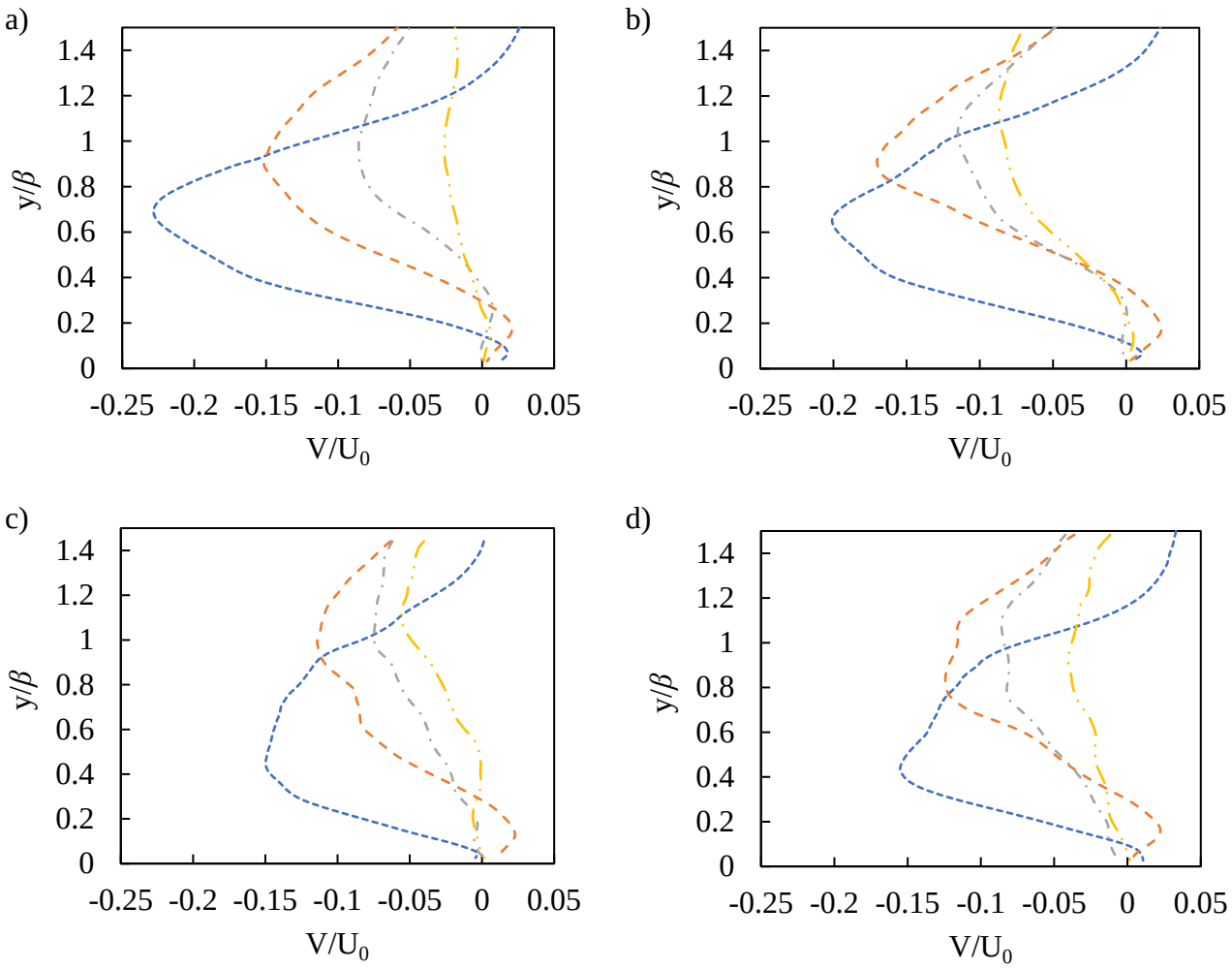

Fig. 36. Time-averaged vertical velocity profiles measured in the down flow region (z/*l* = 0.7) for a) trapezoidal VG (ϕ = 7.6°) at θ = 45°, b) rectangular VG (ϕ = 0°) at θ = 45°, c) trapezoidal VG (ϕ = 7.6°) at θ = 60°, and d) rectangular VG (ϕ = 0°) at θ = 60°: x/*β* = 0.5, x/*β* = 1.5, x/*β* = 2.5, x/*β* = 3.5

Flow characteristics with variable spanwise spacing of VGs in a single row

It has been found that better convective heat transfer occurs in the common-down flow regions of the counter-rotating vortex pairs (CVPs) along with the accelerated streamwise flow [8, 10, 13,14, 38]. When more than two trapezoidal VGs are used, the common-down flows are generated in between the VGs. In this study, three VGs were employed in a single row, aligned with an equidistance along the spanwise direction as shown in Fig. 37(a). The size of VGs were

reduced in order to place multiple VGs within the limited width of the duct, as described in Section 3.5. Details of dimensions of the VGs are shown in Table 3. In order to investigate the effect of spanwise spacing of VGs in a single row, taper angle and inclination angle were set to 7.6° and 45°, respectively. Taper angle was set to 7.6° (trapezoidal) rather than 0° (rectangular) since there was no significant effect on the velocity profiles by taper angle. Furthermore, trapezoidal VGs have smaller projected area, which should reduce the magnitude of the drag force and the corresponding pressure drop in the duct. Inclination angle was set to 45° since VGs with inclination angle of 45° generated CVP with stronger circulation than the ones with inclination angle of 60° based on PIV experiments for the single VG cases (Figs. 34 and 36).

The spacing-to-width ratio (STW = H/l) was varied from 1.0 to 2.5, as shown in Figs. 37(a), 38, 39, 40 and 41. In the case of STW of 1.0, the three VGs are aligned along the spanwise direction without any spacing in between the VGs. PIV analysis was conducted for the CVP generated by the VG located at the center of the duct. Specifically, the mean streamwise and vertical velocities were measured in the common-up flow (z/l = 0 mm, center plane) and common-down flow regions (a plane in between the VGs), as shown in Fig. 37.

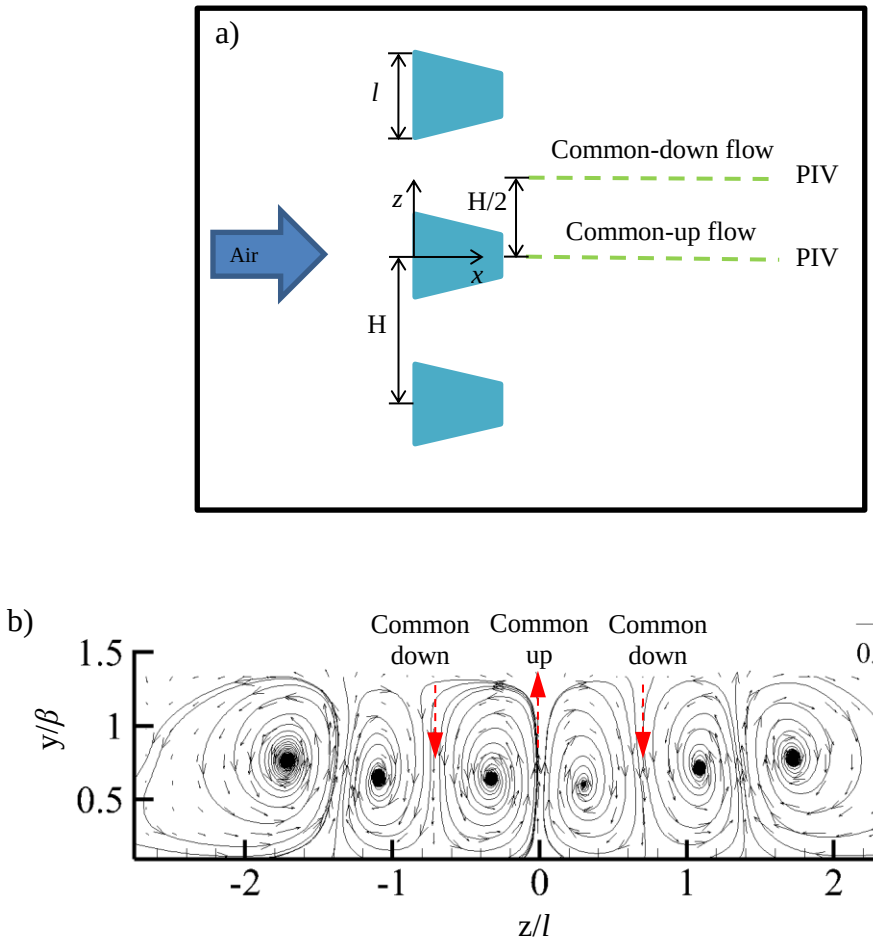

Fig. 37. a) Multiple VGs in single row and b) a sample streamline contour with velocity vectors of the CVPs induced by VGs in a single row with STW of 1.5 at x/β =1

Figure 38 shows the time-averaged streamwise vorticity (ω_i) with velocity vectors measured in the spanwise plane (y-z) at x/β = 1 for different STWs. As shown in Fig. 38, CVPs were not generated completely in the wake of VGs with STW of 1.0 and exhibited very weak streamwise vorticity, as shown in Fig. 38(a). Furthermore, weaker streamwise vorticity was observed with STW of 1.5 than those with STW of 2.0 and 2.5. This implies that the CVPs interacted more vigorously with the neighboring CVPs at STW of 1.5, which led to greater lower

vorticity. The magnitudes of the streamwise vorticity did not vary significantly for STW greater than 2.0 due to a larger separation distance between of CVPs.

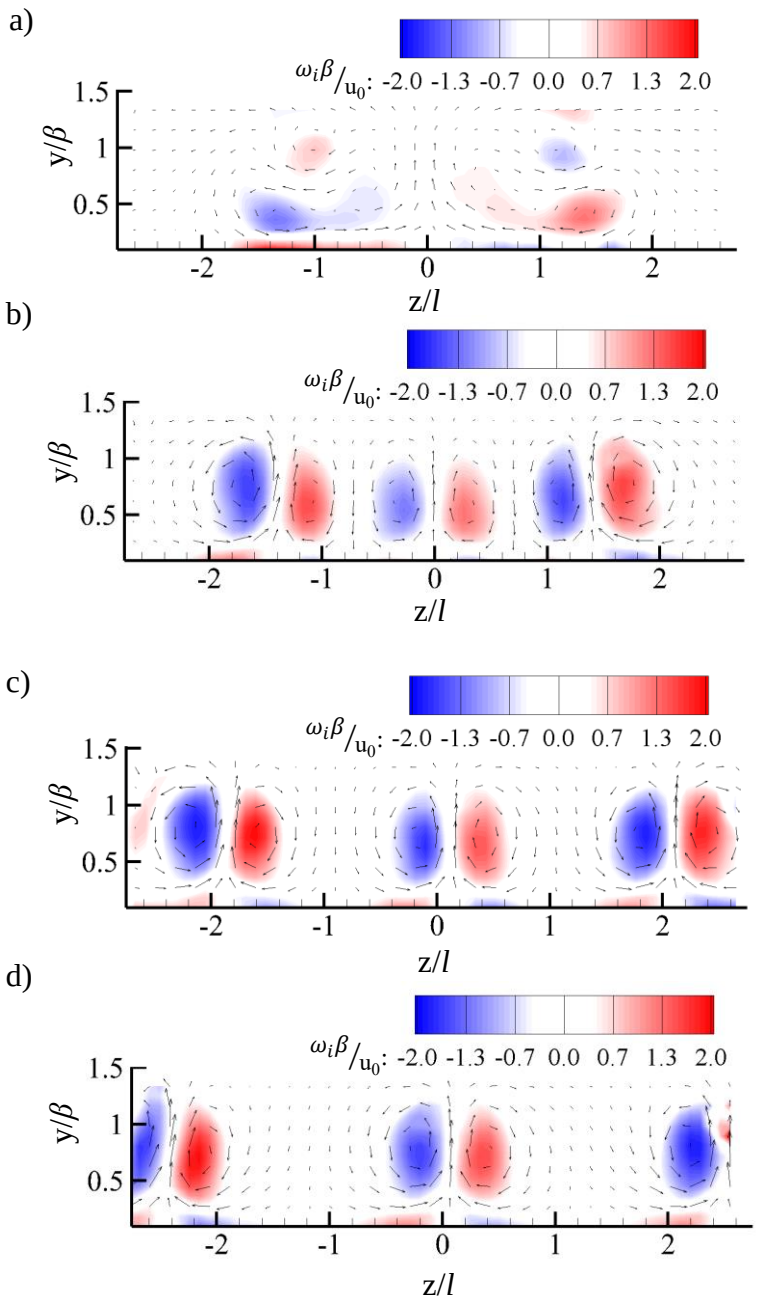

Fig. 38. Time-averaged streamwise vorticity in the spanwise plane (y-z) at x/β = 1 for a) STW = 1.0, b) STW = 1.5, c) STW = 2.0, and d) STW = 2.5

Figure 39 shows a comparison of CVPs in the wake of a single VG and multiple VGs with STW of 2.5. As shown in Fig. 39, the magnitudes streamwise vorticity and velocity vectors for the single VG case and multiple VG case with STW of 2.5 were almost identical. It is important to keep in mind that according to the inviscid potential flow model, described in Section 4.2, CVPs behaved completely independent when a distance between the CVPs was larger than 3 times of l (i.e. STW > 3). Therefore, the PIV results shown in Fig. 39 are consistent with the analytical model, which provides a fair prediction on bulk vortex behavior. The results also show that CVPs produced by multiple VGs at STW values less than 2.5 should lead lower vorticity within each CVP region; however, the CVP adjacent zones are more directly affected by CVP interactions under those conditions (i.e. STW < 2.5)

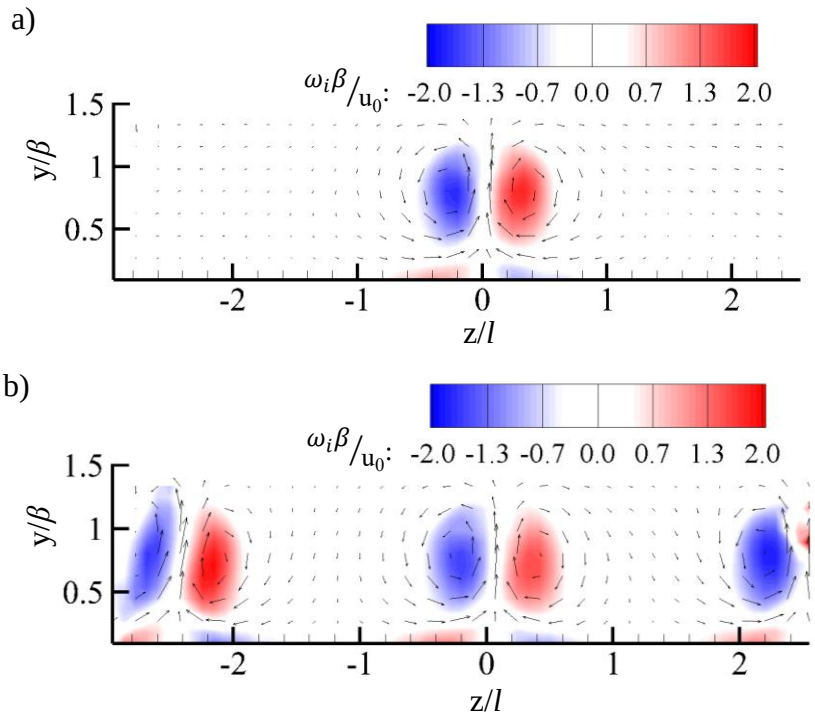

Fig. 39. Time-averaged streamwise vorticity in the spanwise plane (y-z) at x/β = 1 for a) a single VG and b) multiple VGs with STW of 2.5

Figures 40 and 41 show the streamwise and vertical velocity profiles measured in the common-up flow region ($z/l = 0$, center plane) when VGs were placed in a single row with different spacing-to-width ratio (STW). In the figures, the trailing edge of VG was located at x/β of 0. As shown in Figs. 40 and 41, the magnitude of the streamwise velocities increased as the CVPs developed along the downstream while the magnitude of vertical velocities decreased. This suggests that circulation of the CVPs became weaker along the downstream. As a result, the vertical velocity decreased and the streamwise velocity increased [10, 14, 78].

The peak locations of the vertical velocity in Fig. 41 indicate that the CVP stayed close to the wall as it developed downstream for STW of 1.5; however, for the other STW values, the location of peak velocity increased with axial distance. For STW of 1.5, it was evident that the CVP generated by the center VG interacted with the neighboring CVPs, resulting in stronger common-down flows, as shown in Fig. 38b. On the other hand, as STW increased, the vertical locations of the peak velocity increased, indicating that the CVPs moved away from the wall, as shown in Figs. 41. In addition, Figs. 40 and 41 show that the magnitudes of both streamwise and vertical velocities decreased as STW decreased. This implies that CVPs interacted more vigorously with each other for STW less than 2.5, which led to a decrease of CVP strength, as shown in Fig. 38. This is consistent with results and findings discussed by Pearcey [12].

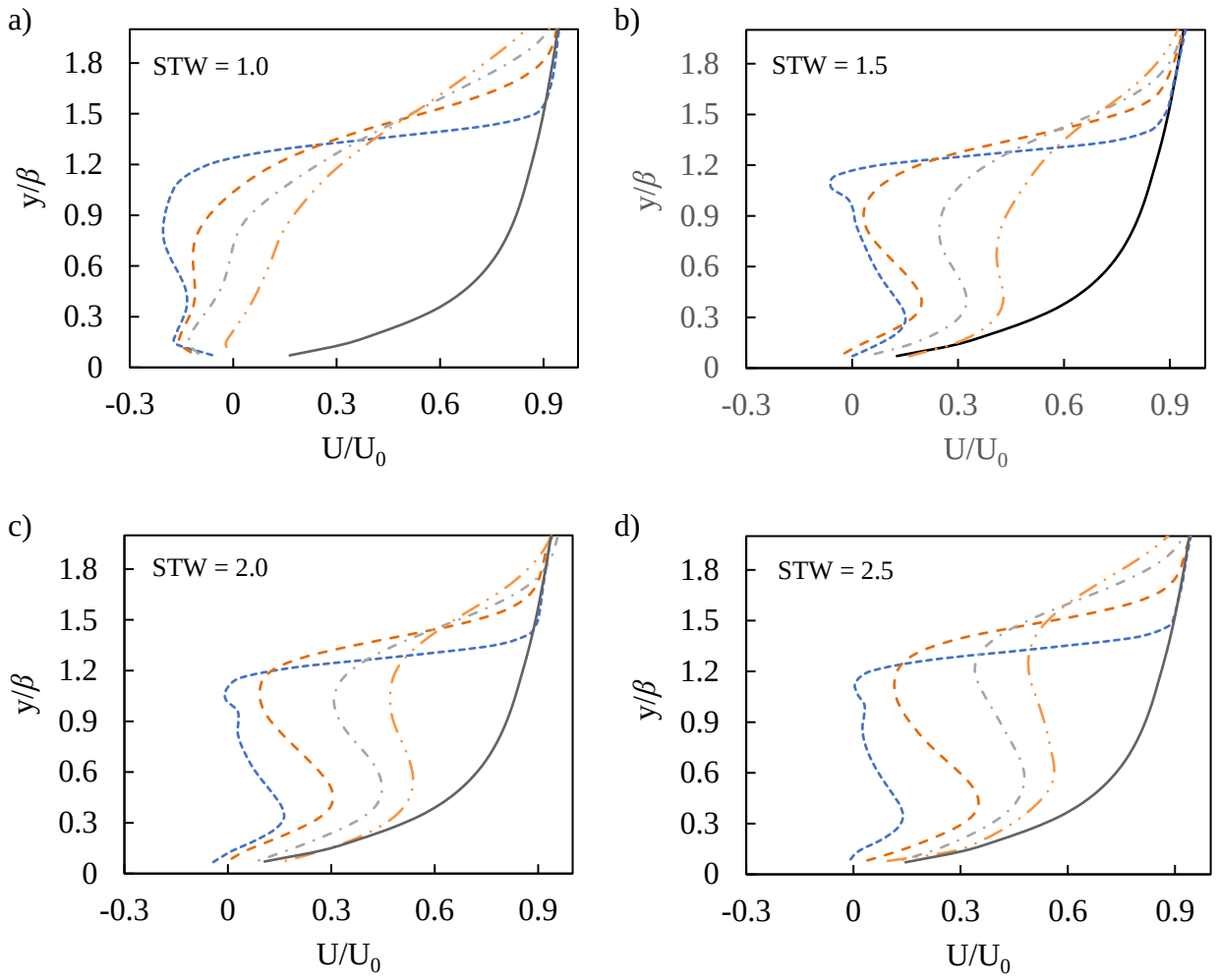

Fig. 40. Time-averaged streamwise velocity profiles measured in the common-up flow region (z/l = 0, center plane) in the wake of trapezoidal VGs (ϕ = 7.6°) at θ = 45° for a) STW = 1.0, b) STW = 1.5, c) STW = 2.0, and d) STW = 2.5:
x/β = 0.5, x/β = 1.5, x/β = 2.5, x/β = 3.5, no VG

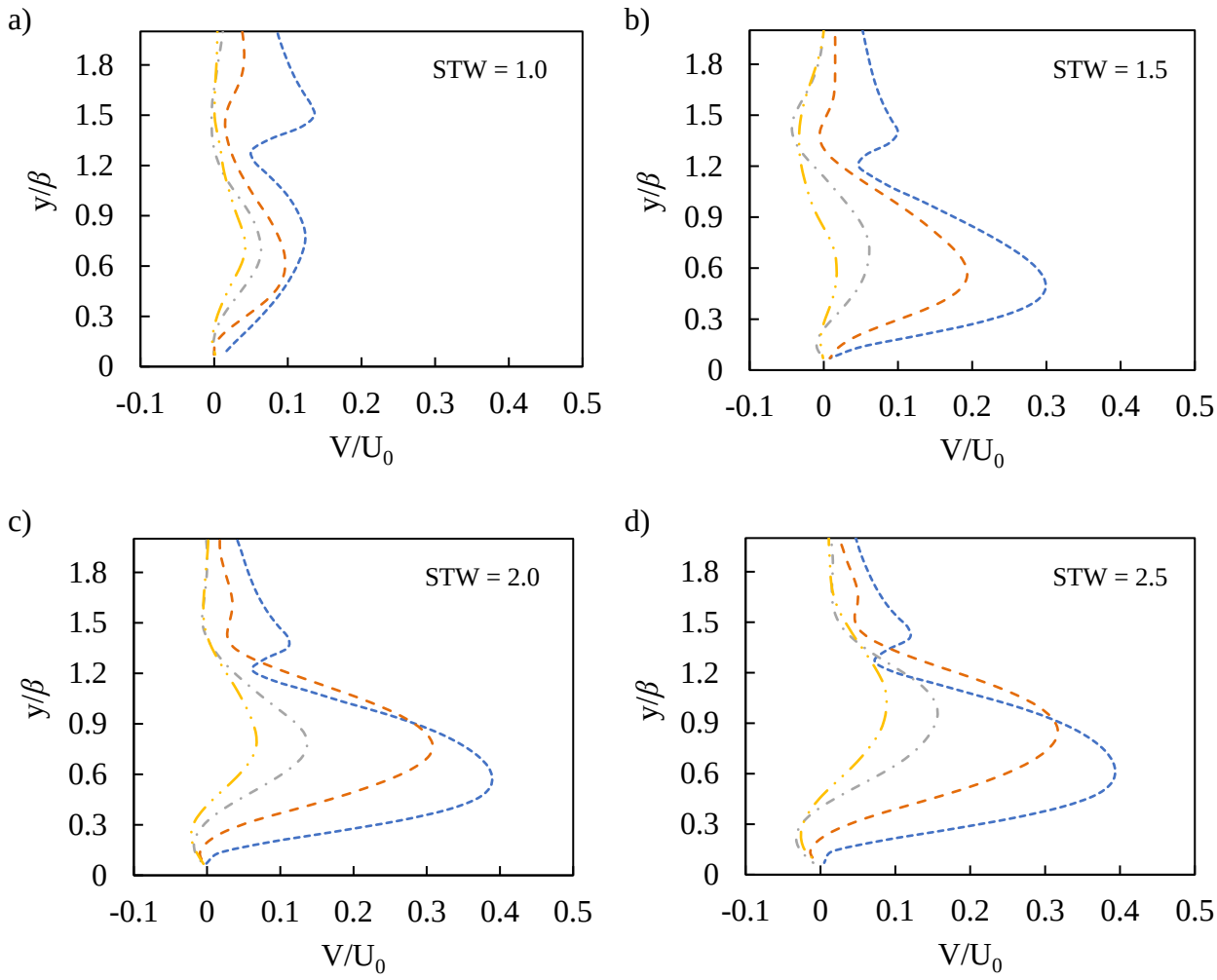

Fig. 41. Time-averaged vertical velocity profiles measured in the common-up flow region (z/*l* = 0, center plane) in the wake of trapezoidal VGs ($\phi = 7.6°$) at $\theta = 45°$ for a) STW = 1.0, b) STW = 1.5, c) STW = 2.0, and d) STW = 2.5:
x/β = 0.5, x/β = 1.5, x/β = 2.5, x/β = 3.5

Figures 42 shows the streamwise velocity profiles measured in the common-down flow region (a plane in between the VGs) for VGs in a single row with different spacing-to-width ratio (STW). As shown in Fig. 40, it was found that the flows in the common-down flow region were accelerated in the streamwise direction, except in the case of STW of 1.0. For STW of 1.0, the VGs had no spanwise spacing. Therefore, a restricted flow path could be found in between the VGs. As a result, the CVP structures were not created completely in the wake of VGs, and the

flow did not experience an acceleration in between the VGs. On the other hand, the flow was accelerated in the streamwise direction significantly for STW of 1.5. It has been known that the accelerated flows increase thermal energy transport in the streamwise direction [8, 39]. Therefore, it is expected that VGs with STW of 1.5 should provide better heat transfer performance, as discussed in Section 4.5 below.

Figures 43 shows the vertical velocity profiles measured in the common-down flow region (a plane in between VGs or at z =H/2) for VGs in a single row with different spacing-to-width ratio (STW). The vertical velocity reached a maximum when STW was set at 1.5; however, the vertical velocities decreased rapidly along the downstream direction, especially at x/β > 1.5, as strength of the CVPs became weaker, as suggested in Figs. 40, and 41. On the other hand, in the case of STWs of 2.5, the vertical velocity did not vary much along the axial distance as shown in Fig. 43(d). This indicates that a row of VGs with STW of 2.5 induced CVPs, which were sufficiently separated from each other and behaved almost like single CVP, as shown in Figs. 38(d) and 39.

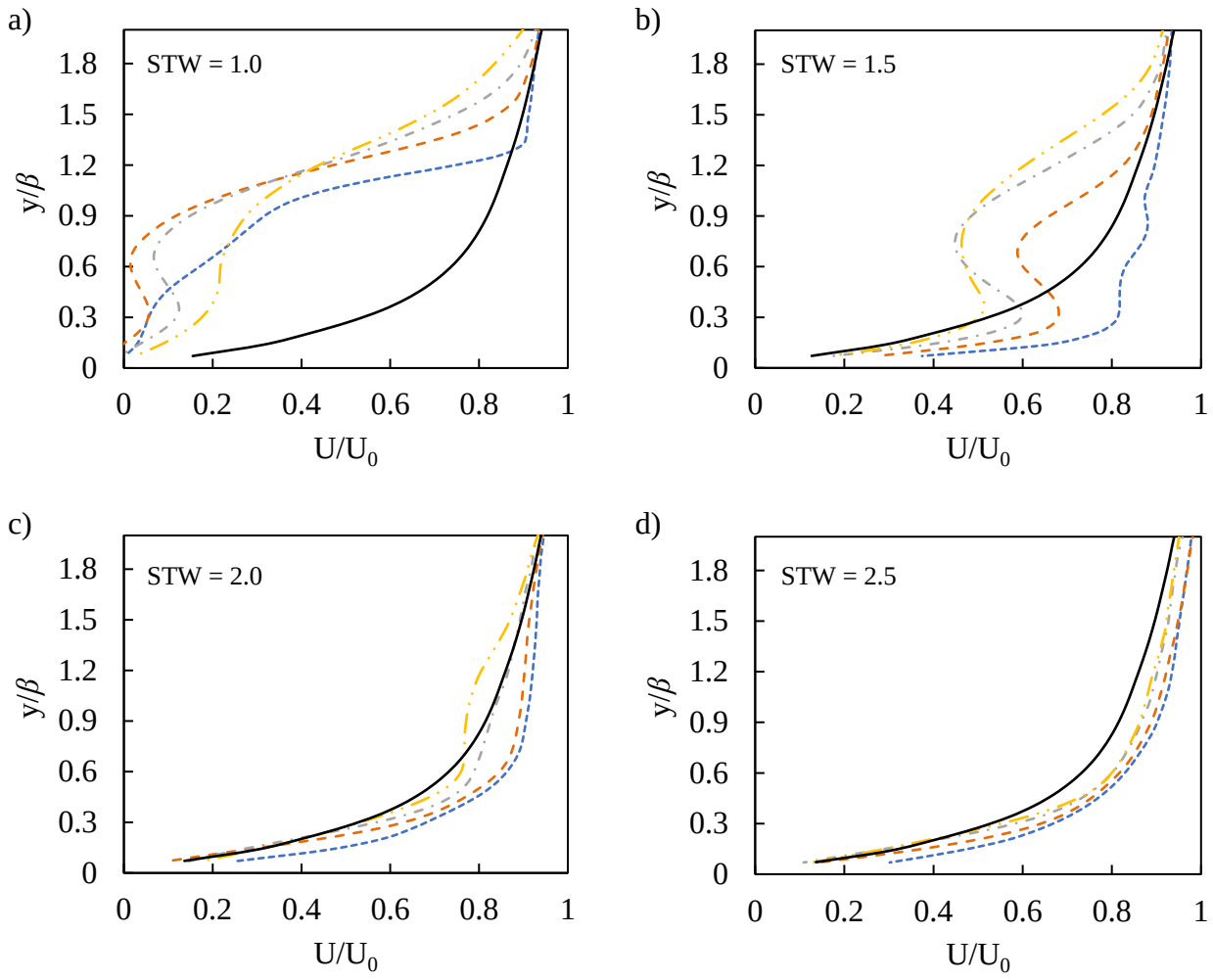

Fig. 42. Time-averaged streamwise velocity profiles measured in the common-down flow region (a plane between of the VGs or at z = *H*/2) in the wake of trapezoidal VGs (ϕ = 7.6°) at θ = 45° for a) STW = 1.0, b) STW = 1.5, c) STW = 2.0, and d) STW = 2.5:
x/*β* = 0.5, x/*β* = 1.5, x/*β* = 2.5, x/*β* = 3.5, no VG

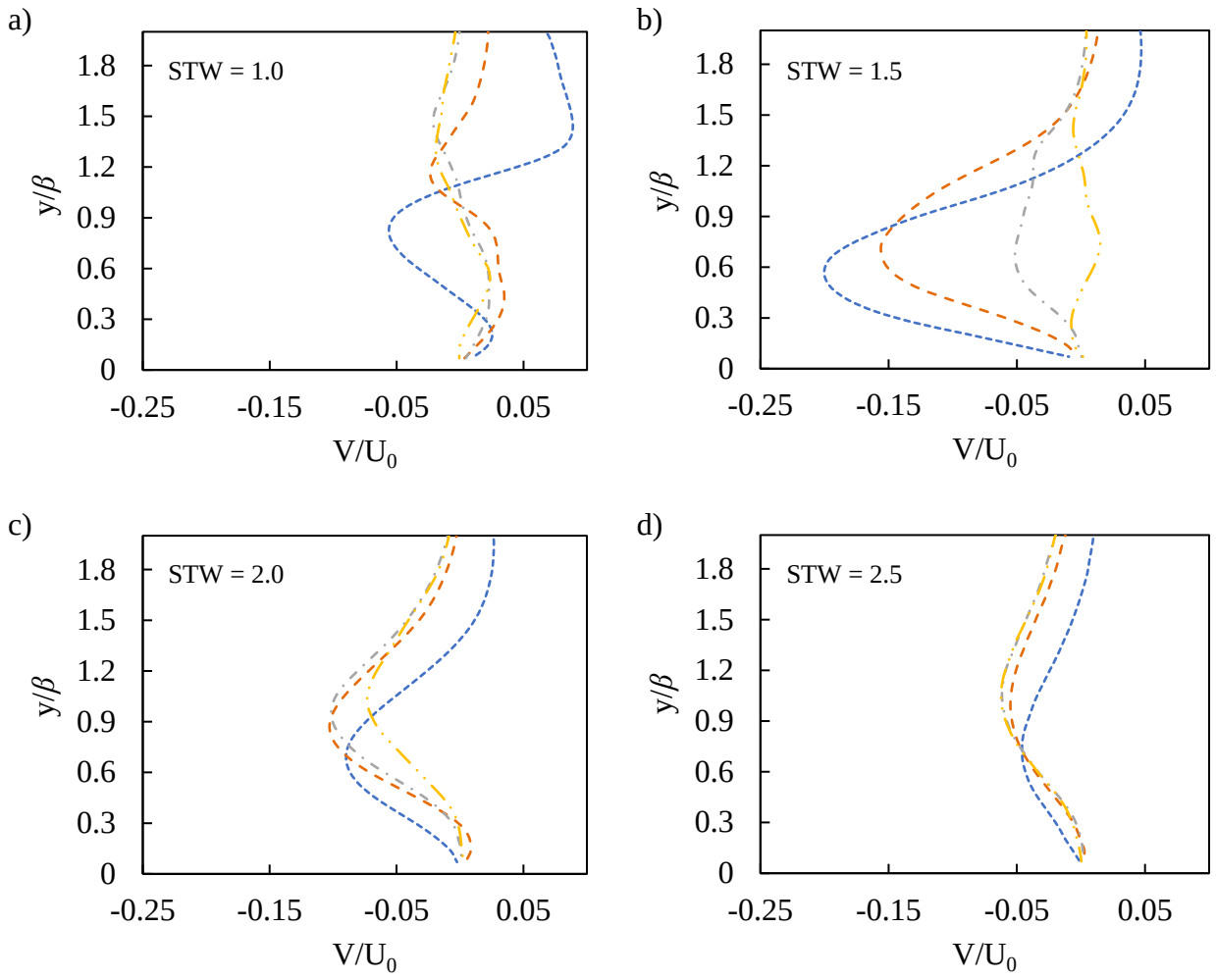

Fig. 43. Time-averaged vertical velocity profiles measured in the common-down flow region (a plane between of the VGs z =*H*/2) in the wake of trapezoidal VGs (ϕ = 7.6°) at θ = 45° for a) STW = 1.0, b) STW = 1.5, c) STW = 2.0, and d) STW = 2.5:
x/*β* = 0.5, x/*β* = 1.5, x/*β* = 2.5, x/*β* = 3.5

Flow characteristics in the wake regions of multiple rows of VGs

Understanding the effects of using multiple rows of VGs on flow behavior is important in many applications including mixing chambers and heat exchanger. Therefore, the effects of rows of trapezoidal VGs on the coherent flow structures were investigated. Specifically, vertical and spanwise velocities were measured in the spanwise plane after the first row, second row, and third row, respectively, to understand how the coherent flow structure changes along the rows of

VGs. Furthermore, the streamwise and vertical velocities were measured in the streamwise plane after the first, second, and third rows of VGs to obtain turbulent flow statistics.

In the study of multiple rows of VGs, three VGs were employed in each row with a spacing-to-width ratio (STW) of 1.5. The STW of 1.5 was used since VGs with STW of 1.5 induced the CVPs with strong common-down flows as shown in Fig. 43. CVPs with strong common-down flows have been known to provide better heat transfer performance [8, 10, 13, 14, 38]. For the STW of 1.5 case, the effect of flow acceleration in the common-down flow region decreased significantly at $x/\beta > 1.5$, as shown in Fig. 42b. Furthermore, as shown in Fig. 43b, the magnitudes of vertical velocity also significantly decreased at $x/\beta > 1.5$. Therefore, each row of VGs was separated along the streamwise distance by a spacing S or x/β of 2. Taper angle (ϕ) and inclination angle (θ) of VGs were set to 7.6° and 45°, respectively, as described in the previous section. The dimensions of VGs used in the multiple row cases are shown in Table 3.

In order to characterize the bulk motion of the coherent flow structures in the wake of rows of VGs, PIV analysis was carried out to measure the mean vertical and spanwise velocities in the spanwise plane. The velocity measurements were done at an axial distance of x/β of 1 from the trailing edges of row of VGs, as shown in Fig. 44.

.

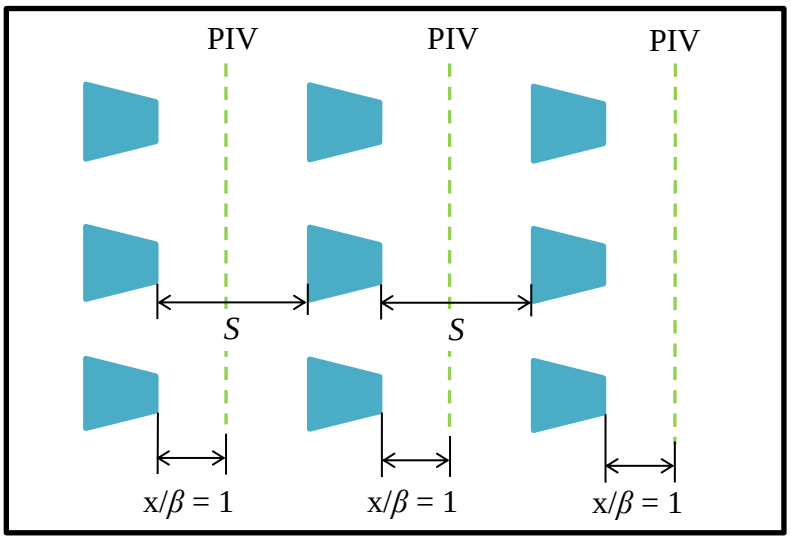

Fig. 44. PIV analysis in the spanwise planes for multiple rows of VGs

Figure 45 shows the streamline contours based on the mean vertical and spanwise velocities measured in the spanwise plane in the wake of the first, second, and third rows of VGs, respectively. As shown in Fig. 45a, VGs generated three CVP structures in the wake of the first row. In the wake of the second row (Fig. 45b), it was found that one of the counter-rotating vortices, which were adjacent to the center CVP, became small and moved close to the wall. This suggests that the flow became less coherent after the second row of VGs. After the third row of VGs, the small vortices, which were observed in the wake of the second row, were completely undistinguishable, as shown in Fig. 43c. As a result, only one vortex remained per VG, indicating that the initial counter-rotating vortex pairs lost their original coherent flow structure.

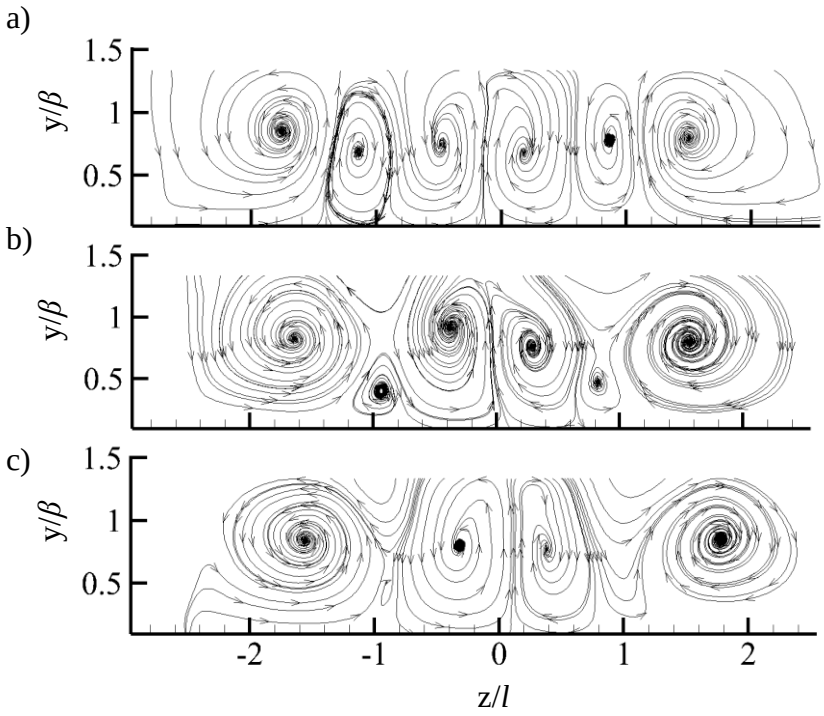

Fig. 45. Streamline contours based on the mean vertical and spanwise velocities in the wake of the a) first row, b) second row, and c) third row, measured at an axial distance of x/β = 1 from the trailing edge of VGs

As the flow became less coherent in the wake of multiple rows of VGs, especially after the second row, the instantaneous flow fields were investigated after each row to understand how the flow behaved with respect to time. As shown in Fig. 46a, CVPs were identified instantaneously in the wake of the first row after 1, 2 and 3 seconds. However, the locations of the centers of CVP vary with time. Furthermore, the vortical structures became much less coherent and contained smaller vortices in the wake of the second and third rows, as shown in Fig. 46b-c. Figure 47 shows the time-averaged streamwise vorticity ($\omega_{i,}$ from Eq. 25) with velocity vectors measured in the spanwise plane after the first, second, and third rows of VGs. As shown in Fig. 47a, CVPs in the wake of the first row have strong vorticity. However, in the wake of the second and third rows, the magnitudes of vorticity of CVPs decreased significantly, as shown in Fig. 47b and 47c. This is because CVPs became less coherent and their strength

became weaker, as suggested in Fig. 45 and 46. Therefore, Figs, 45 – 47 suggest that turbulence statistics are necessary to understand the characteristics of the flow in the wake of multiple rows of VGs accurately.

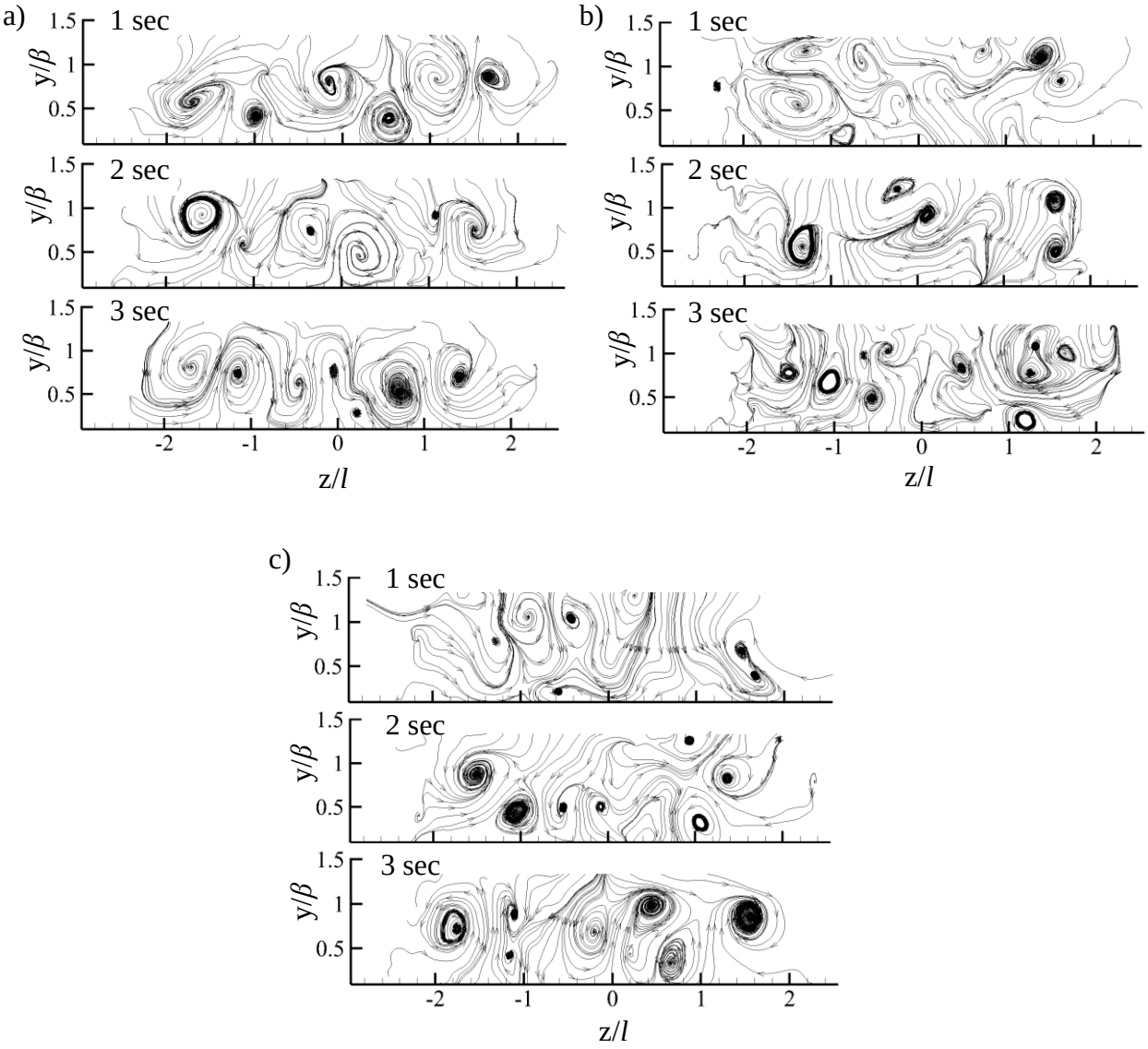

Fig. 46. Streamline contours based on instantaneous velocities in the wake of the a) first, b) second, and c) third rows measured at the locations of x/β = 1 away from the trailing edge of VGs

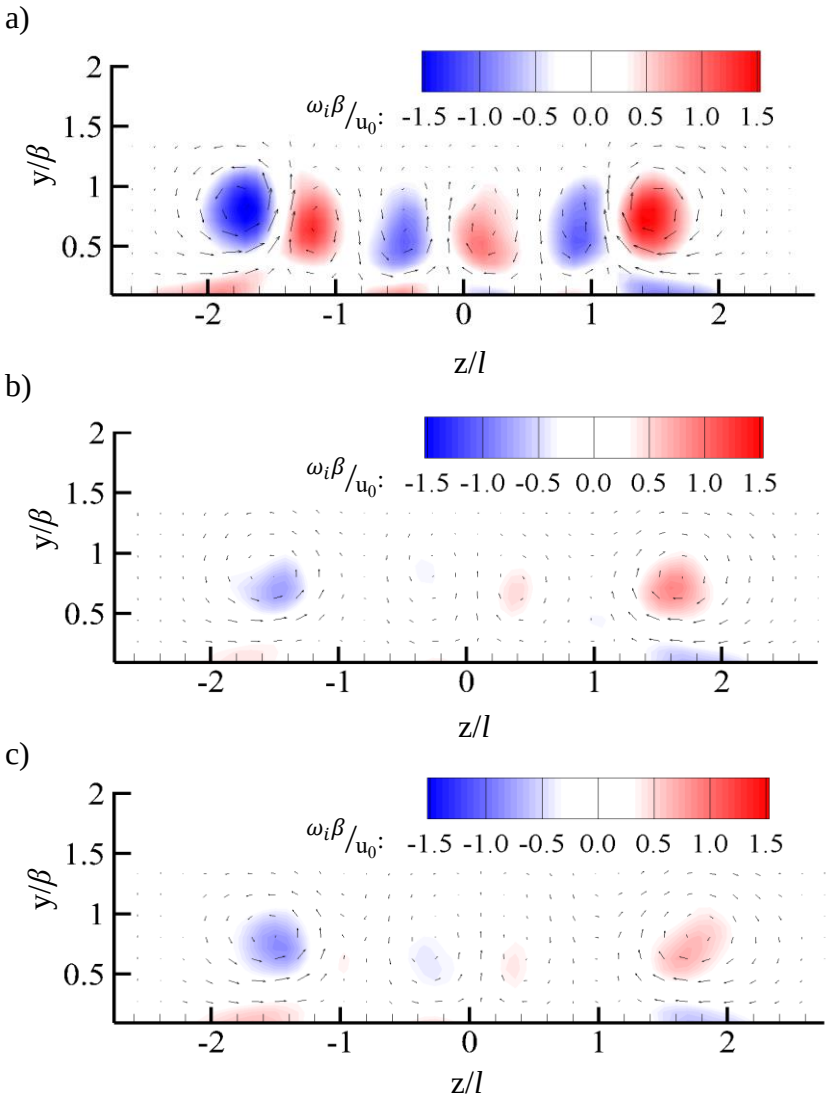

Fig. 47. Streamline contours based on the mean vertical and spanwise velocities in the wake of the a) first row, b) second row, and c) third row, measured at an axial distance of x/β = 1 from the trailing edge of VGs

For better understanding of the flow characteristics in the wake of multiple rows of VGs, PIV analysis was conducted to obtain velocity data in the wake of the first, second, and third rows of VGs, respectively. The mean velocities (U and V), rms velocities (u_{rms} and v_{rms}), and the primary Reynolds stresses ($-\overline{u'v'}$) were obtained in the common-up and common-down flow regions for those cases.

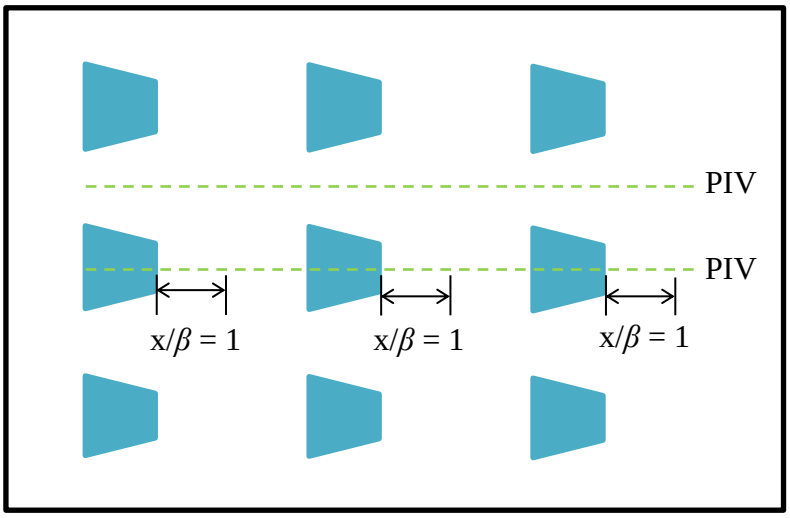

Fig. 48. PIV analysis in the streamwise planes for multiple rows of VGs

Figures 49 shows the mean streamwise and vertical velocities in the common-up flow region (z/*l* = 0, center plane) in the wake of the first, second and third row of VGs, measured at an axial distance of x/β = 1 from the trailing edge of VGs. In the wake of the first row, the mean streamwise velocity of the flow decreased while the mean vertical velocity increased due to the presence of strong CVPs, as shown in Fig 47. However, the mean vertical velocity of the CVPs decreased while the streamwise velocity (U) increased in the wake of the second and third rows of VGs. This suggest suggests that the CVPs became less coherent and weaker in the wake of the second and third rows as streamwise velocity increased, as shown in Figs. 47 and 49(a).

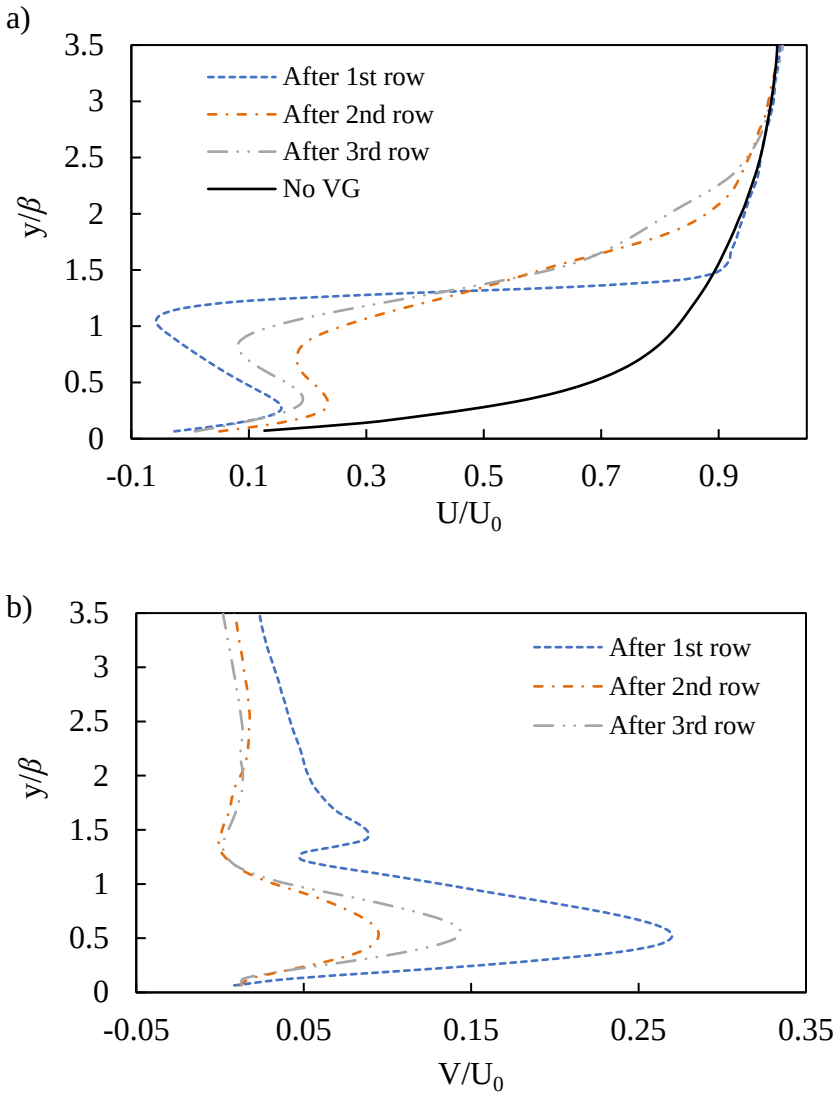

Fig. 49. Time-averaged a) streamwise and b) vertical velocity profiles measured in the common-up flow region (z/l = 0, center plane) at the locations of x/β = 1 away from the trailing edge in the wake of the first, second, and third rows of VGs (ϕ = 7.6°, θ = 45°)

Figure 50 shows the mean streamwise and vertical velocities in the common-down flow region (z/l = 0.75, a plane in between of VGs) in the wake of the first, second and third row of VGs, respectively. As shown in Figs. 47 and 50, the interaction of the center CVP with the neighboring CVPs in the wake of the first row induced strong common-down flow and an acceleration of the flow in the streamwise direction. However, those interactions of the CVP

decreased significantly in the wake of the second and third rows, as seen in Figs. 47 and 50. In summary, the mean velocity data measured in the common-up flow and common-down flow regions also suggest that the CVPs were strong and more coherent in the wake of the first row of VGs. However, the CVPs became weaker and less coherent after the second and third rows.

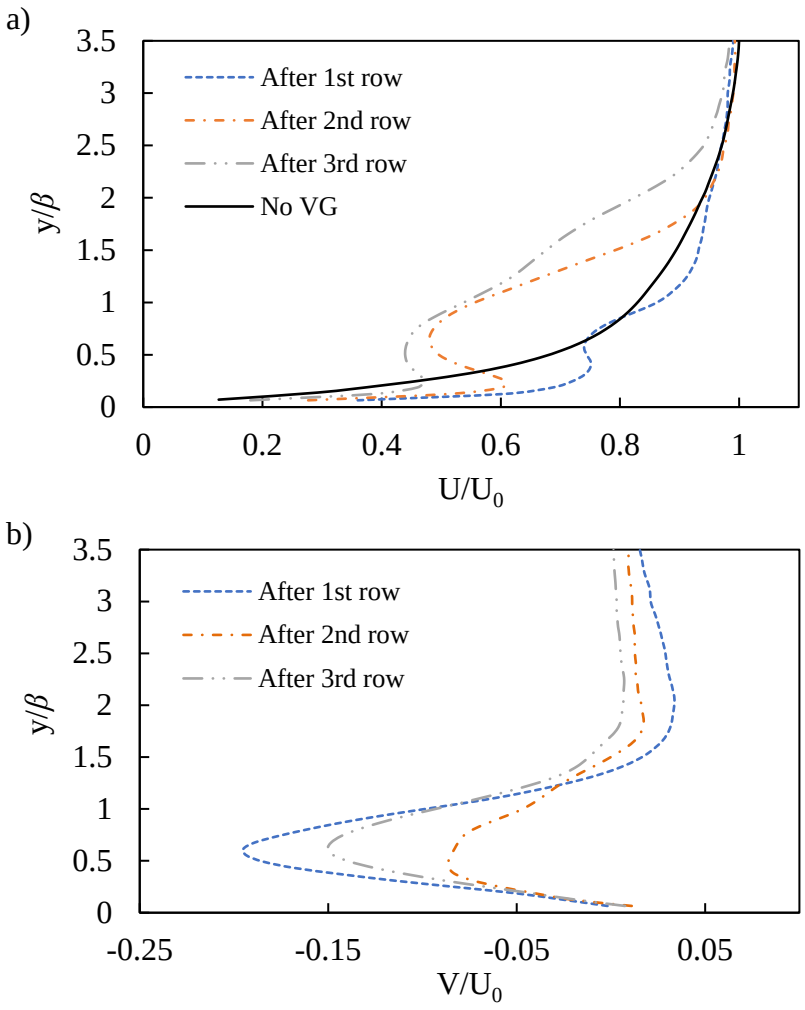

Fig. 50. Time-averaged a) streamwise and b) vertical velocity profiles measured in the common-down flow region (z/l = 0.75, a plane in between of VGs) at the locations of x/β = 1 away from the trailing edge in the wake of the first, second, and third rows of VGs (ϕ = 7.6°, θ = 45°)

Figure 51 shows the root-mean-square of the fluctuating components of the streamwise (u_{rms}) and vertical (v_{rms}) velocities, respectively, in the common-up flow region (z/l = 0, center

plane) in the wake of the first, second and third rows of VGs. In general, as shown in Fig. 51a, the rms velocity in the streamwise direction (u_{rms}) increased significantly for $y/\beta > 1$ due to the shear flow ($\partial U/\partial y$) associated with the trailing edge of VGs. However, in the region below the trailing edge of VGs ($0.5 < y/\beta < 1$), the velocity fluctuations in the streamwise direction decrease with lower mean shear flow ($\partial U/\partial y$), as shown in Fig. 49a. On the other hand, as shown in Fig. 51b, the rms velocity (v_{rms}) increased throughout the most of flow field ($0 < y/\beta < 2$) for all cases. Especially, the increase of rms velocity (v_{rms}) reached a maximum in the wake of the second row of VGs. This indicates that turbulence intensity in the vertical direction increased significantly in the wake of the second row of VGs.

Figure 52 shows the root-mean-square of fluctuating components of the streamwise (u_{rms}) and vertical (v_{rms}) velocities, respectively, in the common-down flow region ($z/l = 0.75$, a plane in between of VGs). In general, the rms velocity in the streamwise direction (u_{rms}) increased for $y/\beta > 0.5$, as shown in Fig. 52a. However, a lower increase of u_{rms} was observed after the first row of VGs. This suggests that the flow was less turbulent and more coherent after the first row. On the other hand, the rms velocity (u_{rms}) increased significantly in the wake of the second row, indicating that turbulent intensity reached a maximum.

Figure 52b shows that the rms velocity in the vertical direction (v_{rms}) slightly increased in the range of $0 < y/\beta < 1$ in the wake of the first row of VGs. On the other hand, the rms velocity (v_{rms}) increased significantly throughout the entire flow field ($y/\beta > 0$) in the wake of the second row of VG. The rms velocities u_{rms} and v_{rms} began to decrease after the third row of VGs, as shown in Fig. 52. In summary, the rms velocity data suggest that turbulence intensity increased significantly in the wake of the second row of VGs.

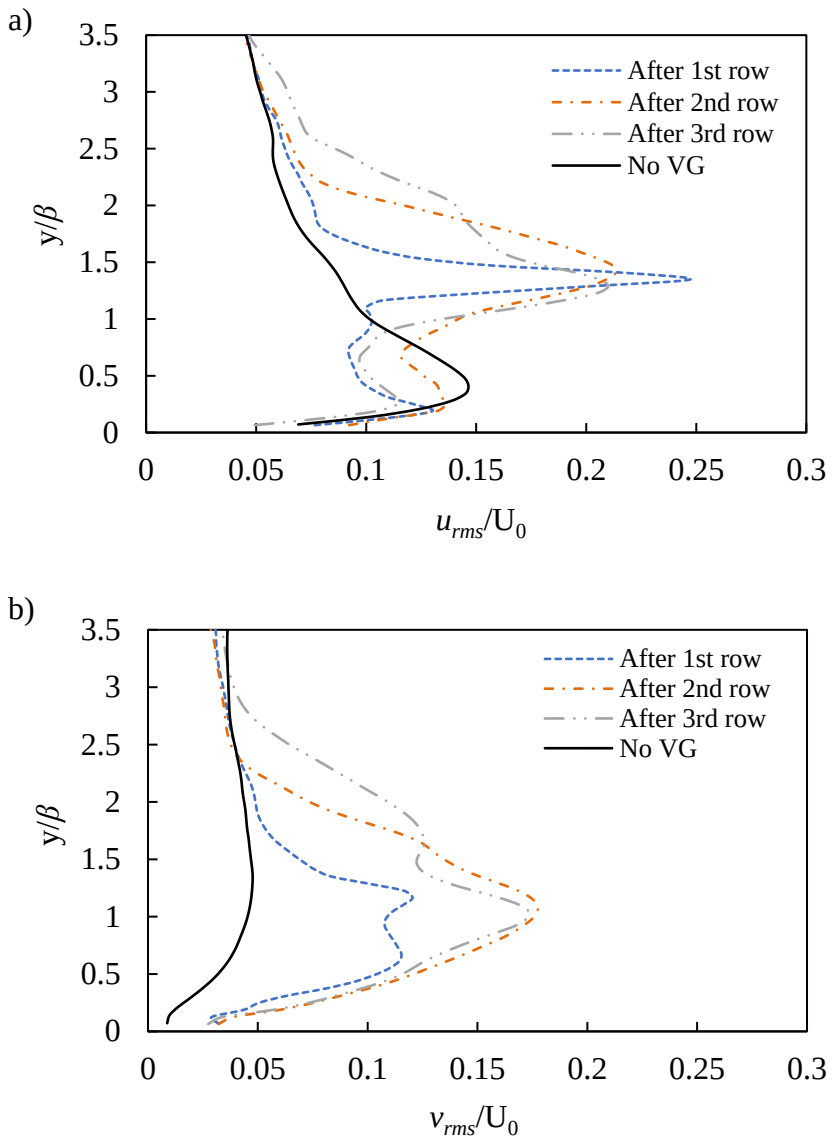

Fig. 51. Root-mean-square of fluctuating components of the a) streamwise and b) vertical velocity measured in the common-up flow region (z/*l* = 0, center plane) at the locations of x/*β* = 1 away from the trailing edge in the wake of the first, second, and third rows of VGs (ϕ = 7.6°, θ = 45°)

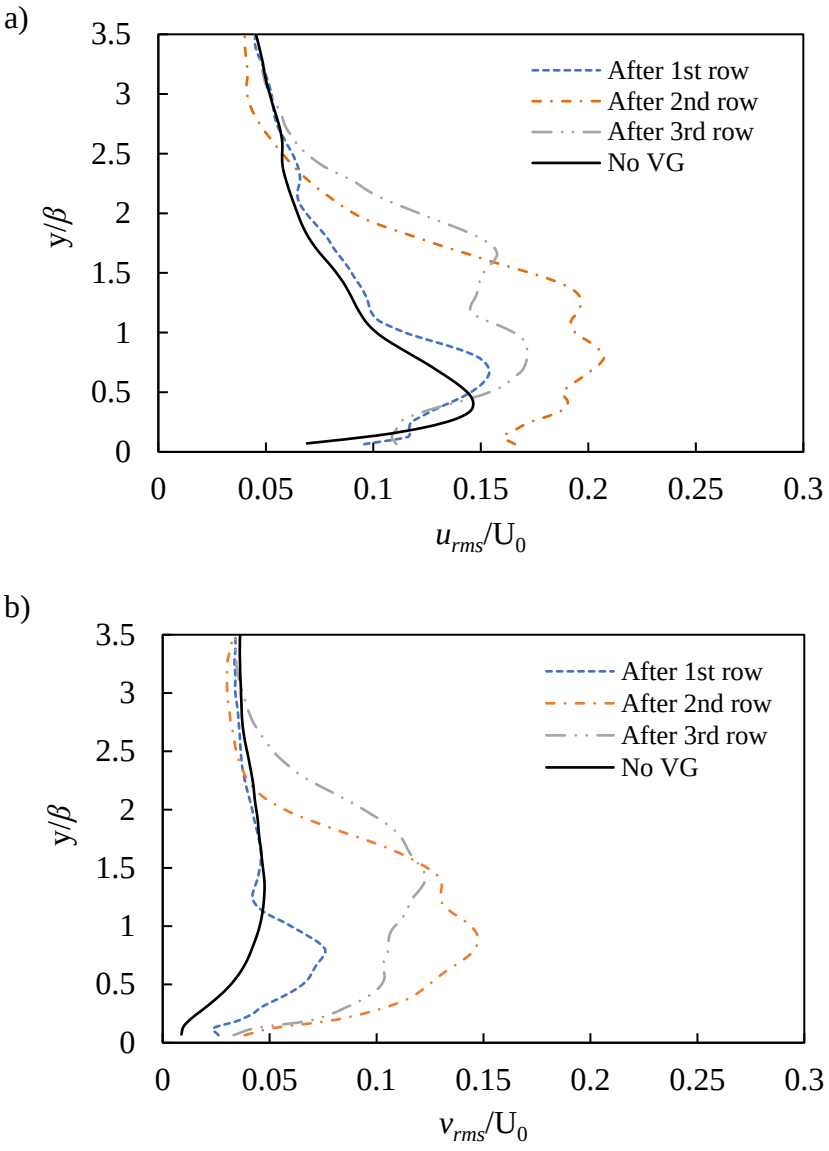

Fig. 52. Root-mean-square of fluctuating components of the a) streamwise and b) vertical velocity measured in the common-down flow region (z/l = 0.75, a plane in between of VGs) at the locations of x/β = 1 away from the trailing edge in the wake of the first, second, and third rows of VGs (ϕ = 7.6°, θ = 45°)

It is known that Reynolds stresses, Equation 26, represent convective momentum generated by the random motion of small vortices [82]. Reynolds stresses themselves are negative when the mean velocity gradient ($\partial U/\partial y$) is greater than zero. When $\partial U/\partial y > 0$,

positive (or negative) value of v' tend to decrease (or increase) u', resulting in a negative value of $u'v'$ [82].

Figure 53 shows the primary Reynolds stress measured in the common-up flow ($z/l = 0$, center plane) and common-down flow region ($z/l = 0.75$, a plane in between of VGs). As shown in Fig. 53a, Reynolds stresses significantly increased at $y/\beta > 1$, where strong mean shear flows were found with shallow slopes of the mean velocity profile seen in Fig. 49a. Negative Reynolds stresses were found at $y/\beta < 1$, where lower values of u_{rms} were found due to a decrease in mean shear flow [82], as shown in Fig. 49a. The primary Reynolds stress increased significantly in the wake of the second row of VGs. This indicates that the strong fluctuating velocities, especially v_{rms} seen in Fig. 51, led to greater Reynolds stresses in the wake of the second row of VGs. The primary Reynolds stress then began to decrease after the third row of VGs.

Figure 53b shows that the primary Reynolds stresses in the common-down flow region. Reynolds stresses became negative in the wake of the first row of VGs ($0.3 < y/\beta < 0.8$) where the mean shear ($\partial U/\partial y$) decreased with steep slopes of the mean velocity profile seen in Fig. 50a. On the other hand, the primary Reynolds stresses increased significantly throughout the entire flow field ($y/\beta > 0$) in the wake of the second row of VG, reaching a maximum value. After the third row of VGs, the primary Reynolds stresses began to decrease.

In summary, the primary Reynolds stress data suggest that turbulent convective momentum by the fluctuating components of velocity would increase significantly in the wake of the second row of VGs. Furthermore, by comparing Figs. 53a and 53b, Reynolds stresses in the common-up flow region were greater than that in the common-down flow region. This is consistent with findings in [14, 21, 78], indicating that strong turbulence intensity was found in the up-flow region of longitudinal vortex due to greater flow instabilities.

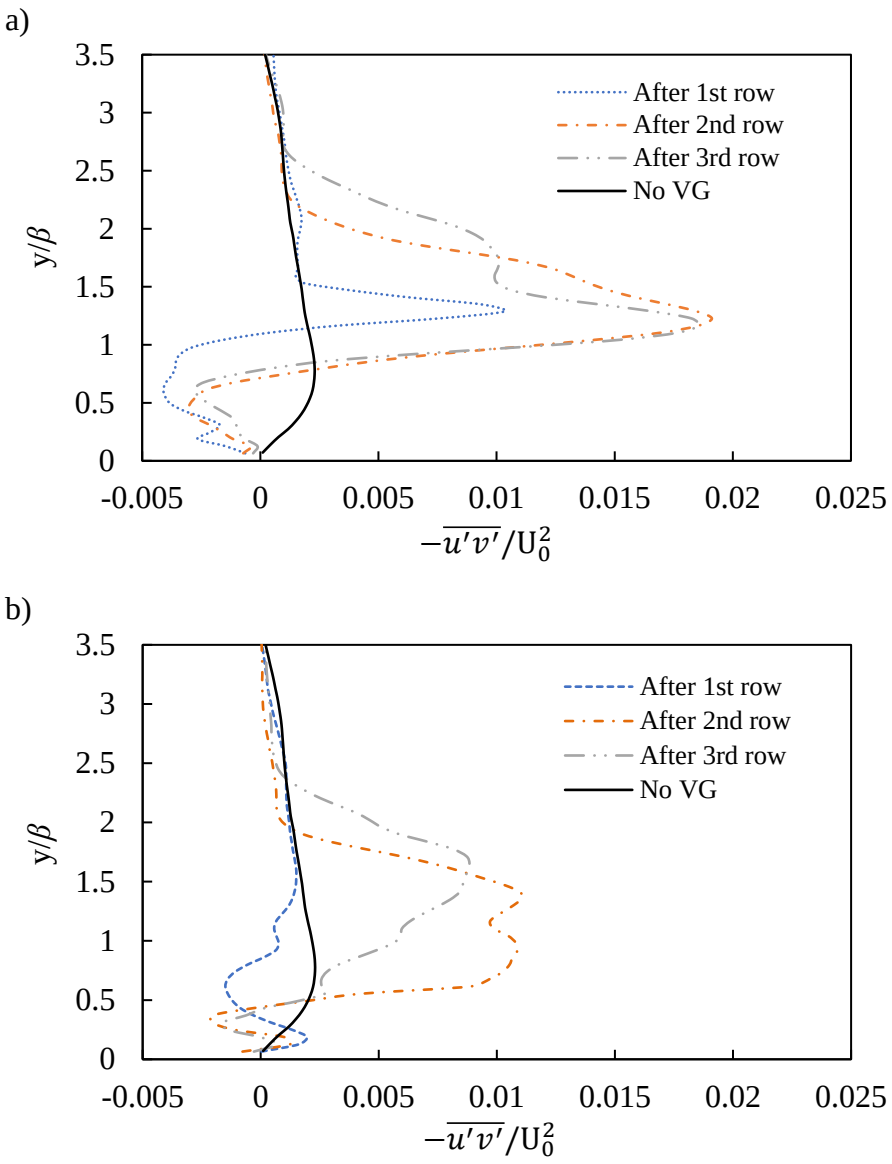

Fig. 53. Primary Reynolds stress $-\overline{\boldsymbol{u'v'}}$ measured in the a) common-up flow (z/*l* = 0, center plane) and b) common-down flow regions (z/*l* = 0.75, a plane in between of VGs) in the wake of the first, second, and third rows of VGs (ϕ = 7.6°, θ = 45°)

4.5 Heat Transfer Results

The effects of the coherent flow on heat transfer are presented, analyzed and discussed in this section. For the single VG cases, the large VGs used in smoke visualization study were employed for heat transfer experiments. However, for the multiple VG cases, the small-scaled VGs were used as shown in Table 3.

Surface temperature of the heat transfer section was measured by using an IR camera. The IR images were record at a sampling rate of 30 Hz. Bulk fluid temperatures were measured using three thermocouples at the inlet and six thermocouples at the outlet of the heat transfer section. The data from IR camera and thermocouples were collected once all the physical variables reached steady state values. The steady state was assumed when the outlet temperatures varied within ± 0.5°.

The local fluid temperatures were obtained by linear interpolation of the inlet and outlet temperatures. Because of the thermal characteristics of heat transfer fluid (air), it has been assumed that the bulk fluid temperature is uniform in the spanwise direction at each axial location. Heat was applied to the bottom surface of the test section only (asymmetric heating). The other walls were insulated and assumed to be adiabatic.

The local fluid temperatures were used to determine the amount of heat applied on the heat transfer surface. Then, heat transfer coefficient was calculated by using the following equation:

$$h = \frac{q''}{T_w - T_b} \tag{26}$$

where $q'' = \dot{m} c_p (T_{out} - T_{in})$, T_w is the spanwise-averaged wall temperature and T_b is the bulk fluid temperature, which was obtained by linear interpolation using inlet and outlet temperature measurements. Nusselt number was determined by using the following equation:

$$Nu = \frac{h \cdot D_h}{k} \tag{27}$$

where D_h is hydraulic diameter of the duct and k is the fluid thermal conductivity determined at the fluid's bulk temperature. Reynolds number of 4800 based on hydraulic diameter was used in all the heat transfer tests. Adequate heat flux was applied so that the fluid bulk temperature difference between the inlet and outlet of the test section was between 1.5 and 2°C at least.

During the experiments, the maximum surface temperatures was 90 °C at the end of heat transfer section when 510 W/m^2 of heat flux was applied.

IR-Temperature measurement validation

Figure 54 shows spanwise-averaged surface temperatures measured using the IR camera. The local fluid temperatures from linear interpolation are also included in the figure. For the constant heat flux boundary condition, the surface temperature increased exponentially first due to the thermal entrance effect and then linearly increased along the heater. This result indicates that the flow in the heat transfer section was thermally developing at $0 < x/\beta < 12$ and thermally fully developed at $12 < x/\beta < 35$.

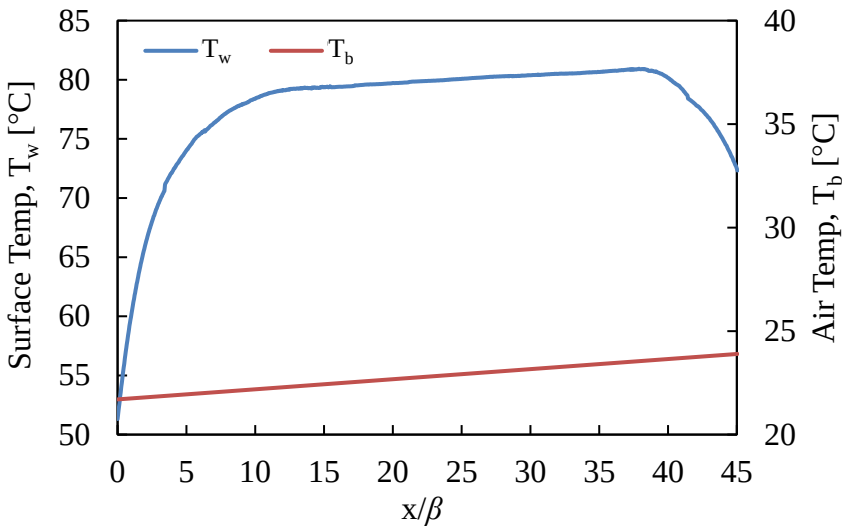

Fig. 54. Spanwise-averaged surface temperature and air temperature along the heat transfer section of the baseline (no VG) case

Figure 55 shows spanwise-averaged Nusselt numbers on the heat transfer surface without VGs. It also includes a Nusselt number value obtained from the following correlation given by Gnielinski for Re = 4800 [83, 84]:

$$\mathrm{Nu} = 0.0214\left(Re^{4/5} - 100\right)Pr^{2/5}\left[1 + \left(\frac{D_h}{\alpha}\right)^{2/3}\right] \tag{28}$$

where D_h is hydraulic diameter of the heat transfer section and α is length of the heater. For fully developed flow, the value of D_h/α in Eq. 28 is set to zero [83-85].

The Gnielinski correlation was established for the flow ($2300 < \mathrm{Re} < 10^6$, $0.5 < \mathrm{Pr} < 1.5$, $0 < D_h/\alpha < 1$) when constant uniform heat flux was applied symmetrically. Spanwise-averaged Nusselt number (Nu) for the baseline case is shown in Fig. 55. When the flow was thermally fully developed, Nu from the experiment was 20.2 and the one from the Gnielinski correlation (Eq. 28) was 18.9. The difference between the experimental results and the Gnielinski correlation value was approximately 7%. It has been found that Nusselt number values for the asymmetrical heating can vary by ± 20% of those for the symmetrical heating cases for turbulent flows [86-90]. Therefore, the 7% difference was due to the asymmetric heating in the system.

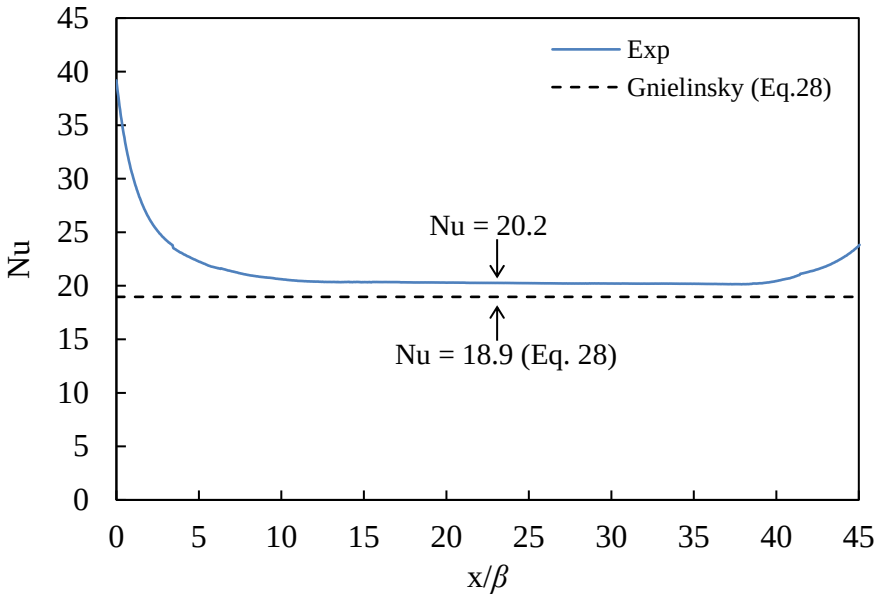

Fig. 55. Spanwise-averaged Nusselt number along the heat transfer section of the baseline (no VG) case

Surface temperature distributions with variable inclination angle and taper angle of single VGs

For heat transfer analysis, the local heat transfer coefficient ratio was obtained based on the IR camera and thermocouple measurements as follows:

$$\frac{h(x,z)}{h_0(x,z)} = \frac{T_{w_0}(x,z) - T_b(x)}{T_w(x,z) - T_b(x)} \quad (29)$$

where h is the local heat transfer coefficient in Eq. 26, and T_w (x, z) is the local surface temperature and the subscript "0" is for the baseline (no VG) case. The local bulk temperature, T_b (x) was obtained by linear interpolation using inlet and outlet temperature measurements. The local heat transfer coefficient ratio (h/h_0) was used to identify the local heat transfer phenomenon induced by the CVP, which is mainly dominant in the wake region, for each case [18, 19, 21-23].

Figure 56 qualitatively shows the effect of the CVPs on the local heat transfer enhancement. In the figure, the trailing edge of VG was located at x/β of 0. In general, better convective heat transfer was found in the down flow region for all cases. As shown in Fig. 56, the CVP flow mechanism directly affected the convective heat transfer process up to x/β = 1.5 approximately. In addition, it was found that the peak value of the local heat transfer coefficient ratio (h/h_0) increased as inclination angle increased. However, it turned out that the peak value of h/h_0 did not change significantly due to the increase in taper angle. The maximum heat transfer enhancements (or greatest value of the local h/h_0) were 18% and 22% for the trapezoidal VGs at inclination angles of 45° and 60°, respectively. Those for the rectangular VGs at inclination angles of 45° and 60° were 19%, and 23%, respectively.

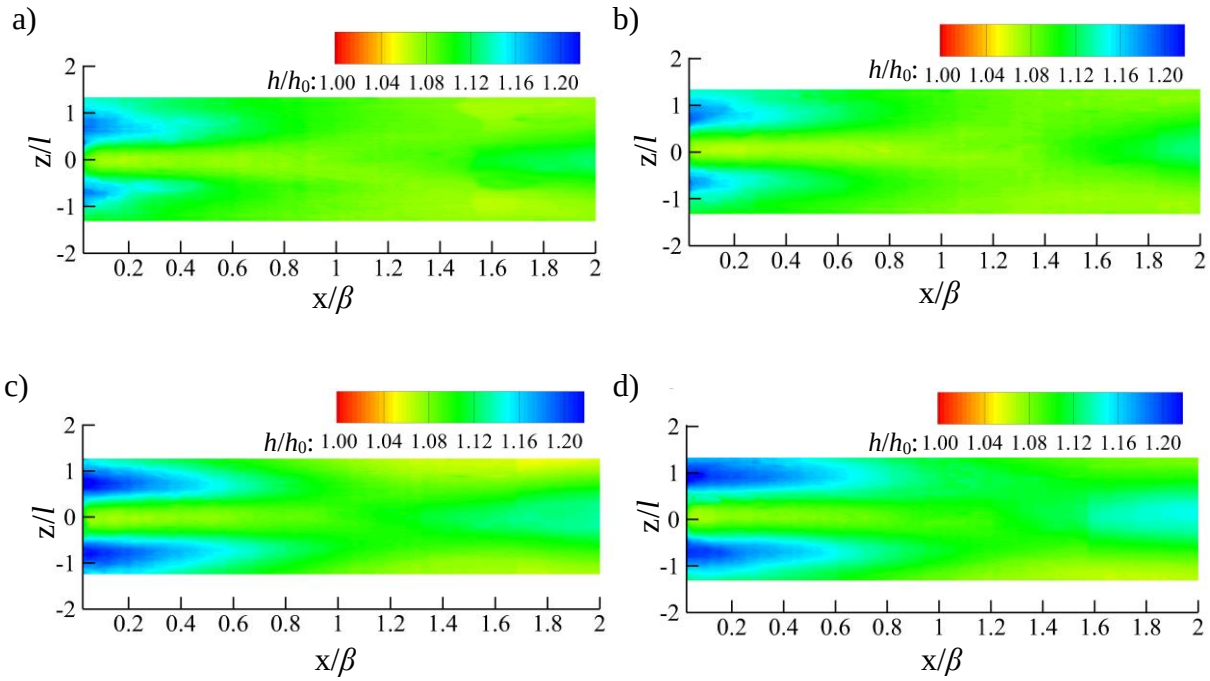

Fig. 56. Contours of the local heat transfer coefficient ratio (h/h_0) for: a) trapezoidal VG (ϕ = 7.6°) at θ = 45°, b) rectangular VG (ϕ = 0°) at θ = 45°, c) trapezoidal VG (ϕ = 7.6°) at θ = 60°, and d) rectangular VG (ϕ = 0°) at θ = 60°

Figure 57 shows the effect of the VGs on surface cooling based on the temperature difference between the local surface temperatures with and without VG (i.e. cooling effect, $\Delta T = T_w - T_{w0}$), along the plane of the common-up flow ($z/l = 0$, center plane) and the plane of the down flow ($z/l = 0.7$). As shown in Fig. 57a, a lesser cooling effect was observed in the common-up flow region, especially in vicinity of the VGs. This is because the flow was decelerated due to the recirculation flow and the formation of a dead zone near the wall ($y/\beta < 0.3$) in the middle of the CVP ($-0.2 < z/l < 0.2$), as shown in Fig. 31. As the CVP developed along the downstream, cooling in the common-up flow region was enhanced ($x/\beta > 1.5$). It suggests that the flow was less affected by the recirculation flow downstream from the VG and the effect of the CVP dead zone on the wall became less significant as the CVP rose along the downstream direction. On the other hand, greater cooling was observed in the down flow region ($z/l = 0.7$) due to the accelerated flows near the wall as seen in Fig. 35. As the CVP developed along the downstream, the cooling effect also decreased, especially for $x/\beta > 1.5$, as shown in Fig. 57. This is consistent with the mean streamwise velocity profiles, indicating that the acceleration of flow near the wall became insignificant after $x/\beta = 1.5$ as seen in Fig. 35a.

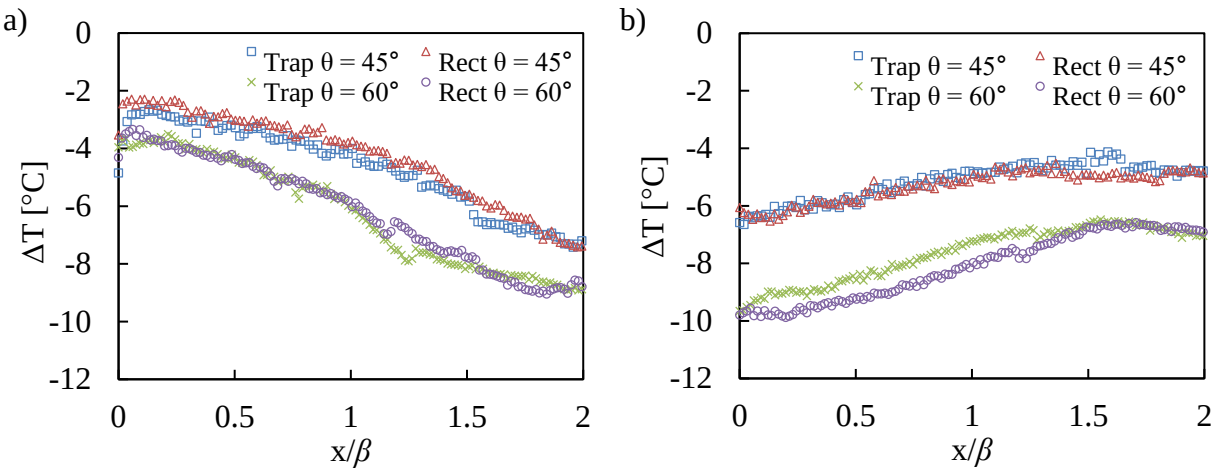

Fig. 57. Local surface temperature difference ($\Delta T = T_w - T_{w0}$) along downstream direction: a) in the common-up flow region ($z/l = 0$, center plane), and b) in the down flow region ($z/l = 0.7$)

Figures 58 and 59 show the variations of ΔT and h/h_0 along the axial distance for further downstream from the trailing edge of VG (i.e. $0 < x/\beta < 5$), respectively. Figure 58a shows that ΔT decreased along the axial distance up to x/β of 3 in the middle of the heat transfer section ($z/l = 0$). It is evident that the CVP flow mechanism affected the convective heat transfer process up to $x/\beta = 1.5$, as shown in Fig. 56; however, the decrease of ΔT (or better cooling) for $1.5 < x/\beta < 3$ could be due to the potential prevalence of anisotropic flow structures near the heat transfer surface [25-27]. Figure 59 also suggests that anisotropic flow structures had an effect on the increase in heat transfer in the middle of the heat transfer section ($-0.7 < z/l < 0.7$) for $1.5 < x/\beta < 3$.

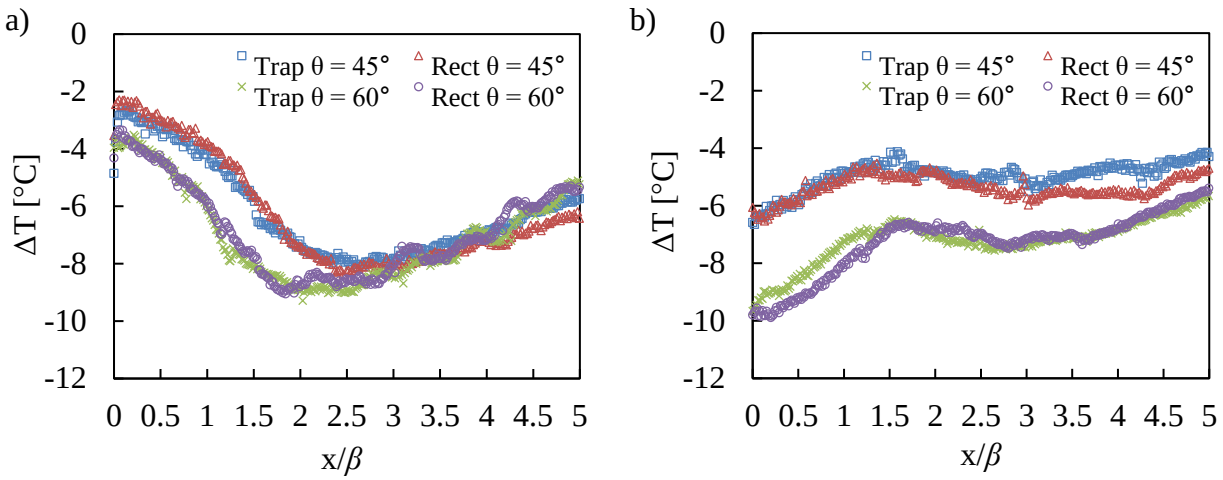

Fig. 58. Local surface temperature difference ($\Delta T = T_w - T_{w0}$) along the axial distance for further downstream from the trailing edge of VG: a) in the common-up flow region ($z/l = 0$, center plane), and b) in the down flow region ($z/l = 0.7$)

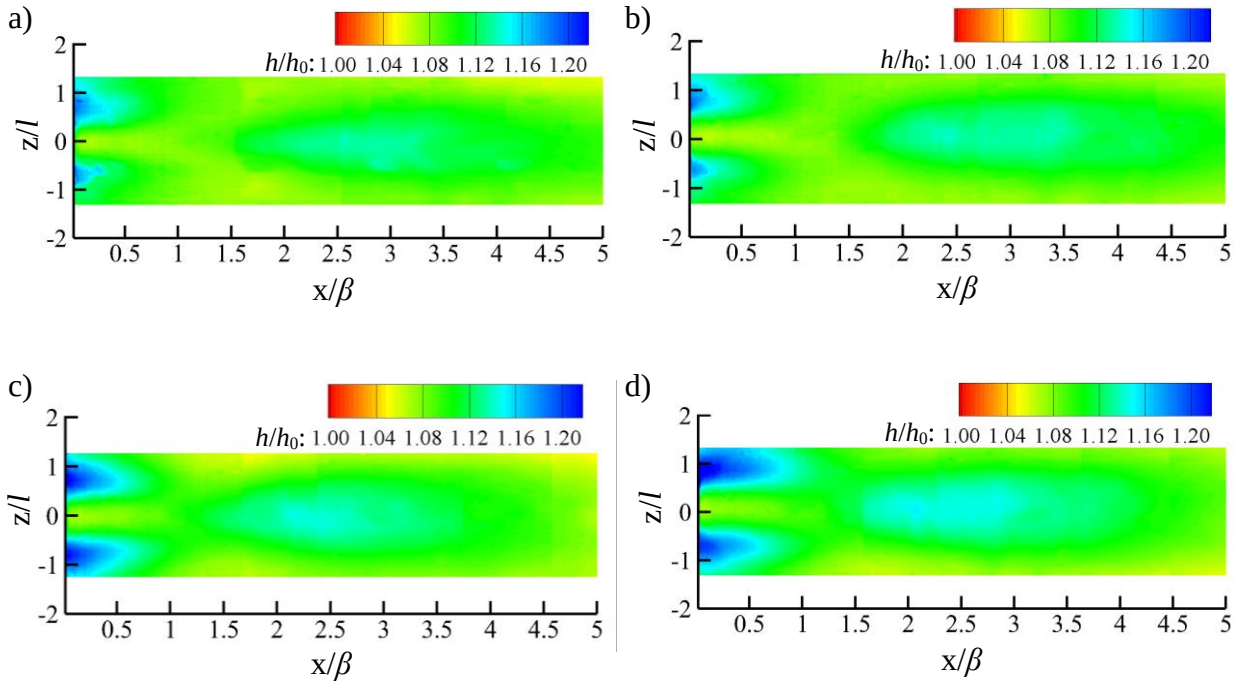

Fig. 59. Contours of the local heat transfer coefficient ratio (h/h_0) for further downstream from the trailing edge of VG: a) trapezoidal VG ($\phi = 7.6°$) at $\theta = 45°$, b) rectangular VG ($\phi = 0°$) at $\theta = 45°$, c) trapezoidal VG ($\phi = 7.6°$) at $\theta = 60°$, and d) rectangular VG ($\phi = 0°$) at $\theta = 60°$

Surface temperature distributions with variable spanwise spacing of VGs in a single row

In order to investigate the effect of spanwise spacing of VGs in a single row on heat transfer, three VGs were employed in a single row with different spacing-to-width ratio (STW). The geometrical factors of VGs in the single row cases are shown in Table 3, which were identical to those used in the PIV experiments in Section 4.4. A spacing-to-width ratio (STW = H/l as shown in Fig. 37a) was varied from 1.0 to 2.5. Surface temperatures were measured by an IR camera under the steady state condition at Reynolds number of 4800 based on the hydraulic diameter.

Figure 60 shows the local heat transfer coefficient ratio (h/h_0 in Eq. 29) for VGs in a single row with different STW values. In the figure, the trailing edges of VGs were located at x/β of 0. As shown in Fig. 60a, lower heat transfer enhancement (or lower value of the local h/h_0) was observed for STW of 1.0, especially in a region of $-1 < z/l < 1$. Due to the restricted flow path for STW = 1.0, the flow velocities in the streamwise and vertical directions decreased significantly in both the common-up and common-down flow regions, as shown in Figs. 40a, 41a, 42a, and 43a. As a result, lower heat transfer enhancement was observed for STW of 1.0. On the other hand, better convective heat transfer (or greater value of the local h/h_0) was found for STW of 1.5, especially in the common-down flow region (a plane in between of VGs, or $z = H/2$), as shown in Fig. 60b. The PIV results indicated that CVPs with strong common-down flow were induced in between of VGs for STW of 1.5, as shown in Fig. 38b and 43b. Furthermore, the flow was accelerated in the streamwise direction, especially near the wall ($y/\beta < 0.3$ shown in Fig. 42b). As a result, heat transfer enhanced significantly as shown in Fig. 58b. In addition, Fig. 60b also shows that the CVP flow mechanism affected the convective heat transfer process up to $x/\beta = 1.5$ approximately for STW of 1.5. This is also consistent with the velocity data, indicating

that the flow acceleration and the magnitudes of vertical velocity in the common-down flow region decreased significantly for $x/\beta > 1.5$, as shown in Figs. 42b and 43b.

Figure 60 also shows that as STW increased, lower heat transfer enhancements were observed in the common down flow region. For lower STW values (i.e. 1.5), stronger common-down flows were generated in between of VGs as shown in Figs. 38 and 43. Furthermore, the flow was also more accelerated in the streamwise direction for lower STW, as shown in Fig. 42. The maximum heat transfer enhancements (or greatest values of the local h/h_0) in the common-down flow region were 20%, 16%, and 13% for STW of 1.5, 2.0, and 2.5, respectively.

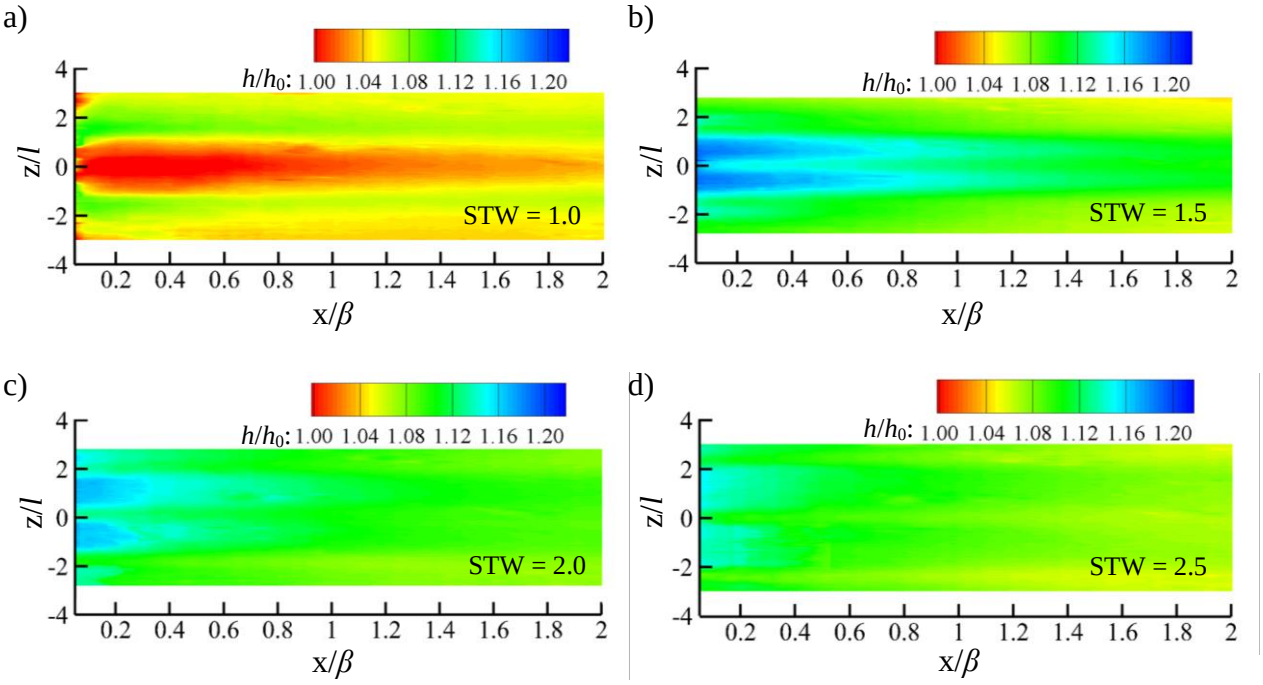

Fig. 60. Contours of the local heat transfer coefficient ratio (h/h_0) for a single row of trapezoidal VG ($\phi = 7.6°$) at $\theta = 45°$ with a) STW = 1.0, b) STW = 1.5, c) STW = 2.0, and d) STW = 2.5

Surface temperature distributions with variable configuration of multiple rows of VGs

It has been known that CVPs can either remain energetic or become weak in the downstream region, depending on the configuration or arrangement of VGs [12]. Therefore, in the study of multiple rows of VGs, four different configurations were considered in order to find the one providing the best heat transfer performance. Specifically, rows of VGs were either aligned and staggered with respect to the proceeding rows of VGs at two different streamwise spacings (S) of 2β and 3β, as shown in Fig. 61. In each row, three VGs were employed with a spacing-to-width ratio (STW) of 1.5. The STW of 1.5 was used since VGs with STW of 1.5 provided the best heat transfer performance for a single row as shown in Fig. 60. The dimensions of VGs used in the multiple row cases are shown in Table 3. Beginning of the heat transfer section was set at $x/\beta = 0$ with the leading edge of the first row of VG located at $x/\beta \approx 0.5$ and 1 for staggered and the aligned cases, respectively.

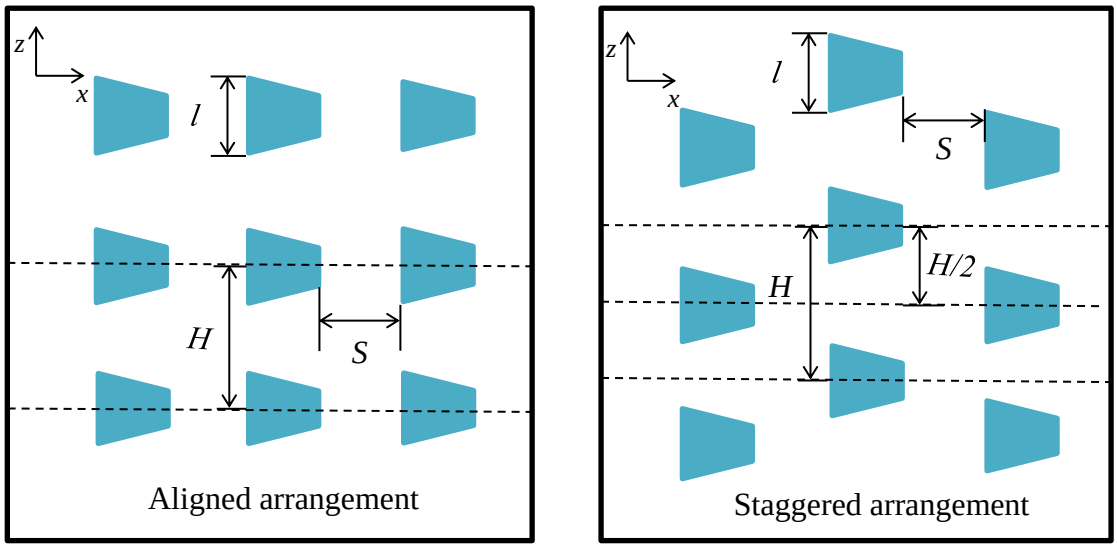

Fig. 61. Heat transfer experiments for multiple rows of VGs

Figure 62 shows the local heat transfer coefficient ratio (h/h_0 in Eq. 29) for VGs in aligned and staggered arrangements with S of 2β and 3β. As shown in Figs. 62a and 62b (or Figs. 62c and 62d), better heat transfer enhancements were obtained with aligned arrangements, when compared to staggered arrangements. Furthermore, it was found that heat transfer enhancement was greater for S of 2β than at 3β, regardless of its arrangement. Therefore, this suggest that an aligned arrangement with S of 2β was closer to an optimal configuration, when compared to the other cases. Therefore, additional heat transfer analyses were done for VGs with aligned arrangement with S of 2β (Fig. 62a), as discussed below.

For S of 2β, as shown in Fig. 62a, it was found that there was significant increase in heat transfer in the common-down flow regions in the wake of the first row, where the flows were more coherent, as shown in Figs. 45a, 46a, 50, 51b–53b. Furthermore, the mean streamwise and vertical velocities increased significantly in the common-down flow region, especially in the near-wall region, as shown in Fig. 50a and 50b, respectively. On the other hand, Figs. 51b showed that the rms velocities and Reynolds stresses were lower after the first row, when compared to the other cases, especially those in the common-down flow regions. Therefore, this suggests that the increase in heat transfer in the common-down flow regions after the first row was mainly driven by the mean motion of CVPs, associated with a significant increase of mean streamwise and vertical velocities near the wall, as shown in Fig. 50.

It is important to note that, in Fig. 62a, heat transfer increased significantly in the wake of the second row, where CVPs were less coherent, as shown in Figs. 45b, 46b, 49–53. In the wake of the second row, the mean streamwise velocity increased while the vertical velocity decreased significantly in both the common-up flow regions, as shown in Fig. 49. Also, in the wake of the second row, the mean streamwise and vertical velocities decreased significantly in the common-

down flow regions, as shown in Fig. 50. On the other hand, in the wake of the second row, the rms velocities and Reynolds stress values increased significantly in both regions, as shown in Figs. 51, 52, and 53, respectively. Therefore, these observations suggest that when the ratio of rms velocity to mean velocity and Reynold stress increase as shown in Table 6, heat transfer increases as shown in Fig. 62a. This clearly suggests that flow fluctuations and their corresponding enhanced levels of fluid mixing induced by the arrangement of multiple rows of VGs have a direct effect on heat transfer [14, 78-81].

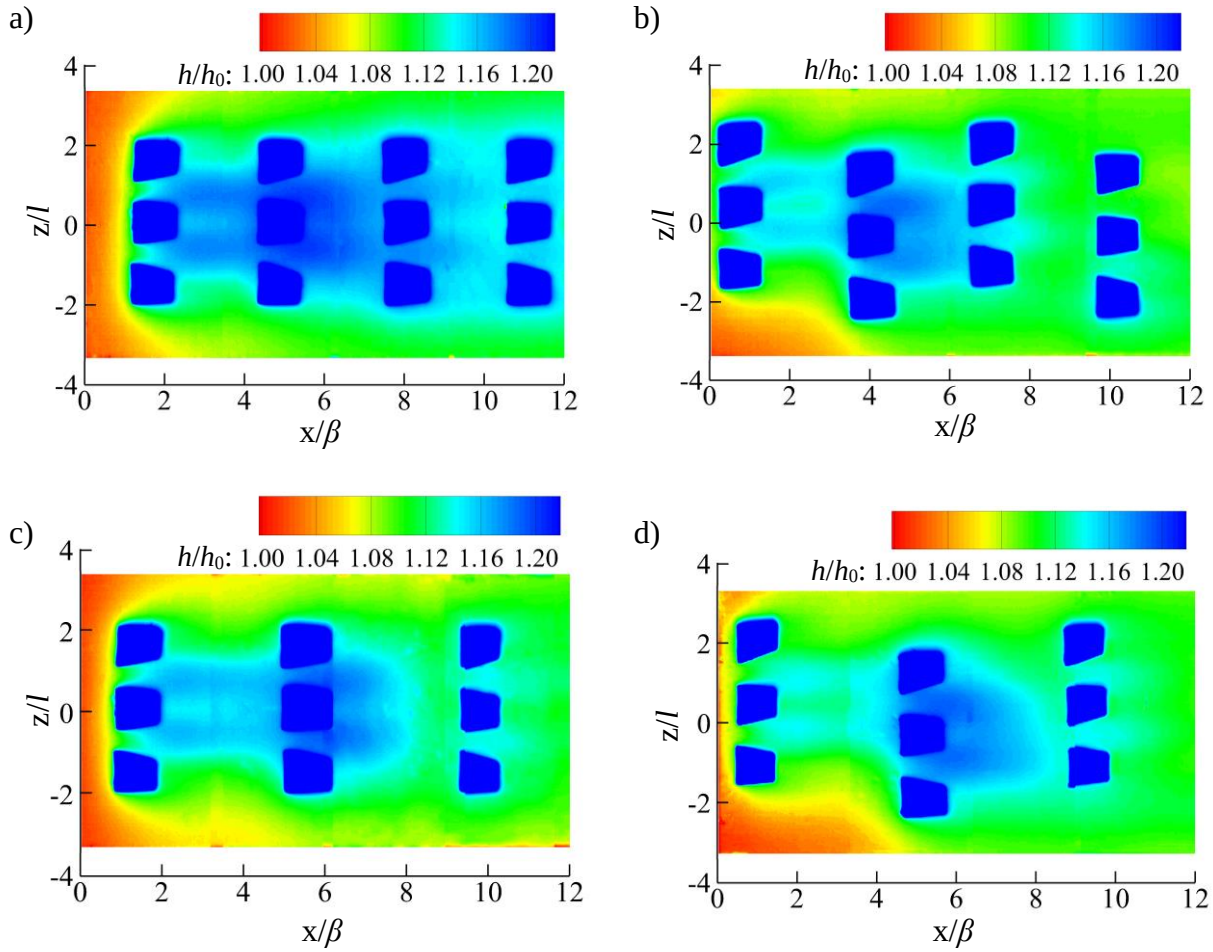

Fig. 62. Contours of the local heat transfer coefficient ratio (h/h_0) for multiple rows of trapezoidal VG ($\phi = 7.6°$) at $\theta = 45°$ with different configurations: a) Aligned, $S = 2\beta$, b) Staggered, $S = 2\beta$, c) Aligned, $S = 3\beta$, and d) Staggered, $S = 3\beta$

Figure 62a also indicates that heat transfer enhancement decreased after the third row. In the wake of the third row, the rms velocities and Reynolds stresses decreased especially in the common-down flow regions, as shown in Fig. 51b–53b. Therefore, this suggests that the lower heat transfer enhancement was caused by lower turbulence intensities (u_{rms} and v_{rms}) as well as lower Reynolds stresses ($-\overline{u'v'}$), while the mean velocities decreased, as shown in Figs. 45c, 46c, 49, and 50.

In summary, the increase in heat transfer was driven by the mean motion of CVPs when the flow was coherent and less turbulent. However, the turbulent fluctuating motion of the flow (i.e. rms velocities) became a dominant local mechanism for enhancing heat transfer once the flow became less coherent [14, 78-81].

Table 6. Peak values of Root-mean-square of velocity fluctuations and Reynolds stress in the region of $y/\beta < 1$ for multiple rows of VGs

	After the 1st row		After the 2nd row		After the 3rd row	
Region:	Common-up	Common-down	Common-up	Common-down	Common-up	Common-down
u_{rms}/U_0	0.12	0.18	0.136	0.21	0.113	0.17
v_{rms}/U_0	0.115	0.076	0.177	0.15	0.172	0.11
$-\overline{u'v'}/U_0^2$	-0.0038	0.001	-0.003	0.011	-0.0028	0.0059

Note: Obtained at $x/\beta = 1$ away from the trailing edge in the wake of the first, second, and third rows of VGs, respectively

Surface temperature distributions with variable streamwise spacing of clusters of VGs

It has been found that the heat transfer enhancement decreased after the third row of VGs, as shown in Fig. 62. Therefore, heat transfer experiments were conducted to study how heat transfer performance could vary with the use of clusters of VGs as shown in Fig. 63. The streamwise cluster spacing (B) for clusters consisting of three rows of VGs was adjusted as shown in Fig. 63, to determine its effect on heat transfer. In each cluster, VGs were aligned with S of 2β and VGs were placed with STW (H/l) of 1.5 in each row given the optimal heat transfer performance seen in Figs. 60b and 62a under those conditions. The streamwise spacing (B) was varied from 2β (continuous use of rows of VGs with no visible clusters) to 5β.

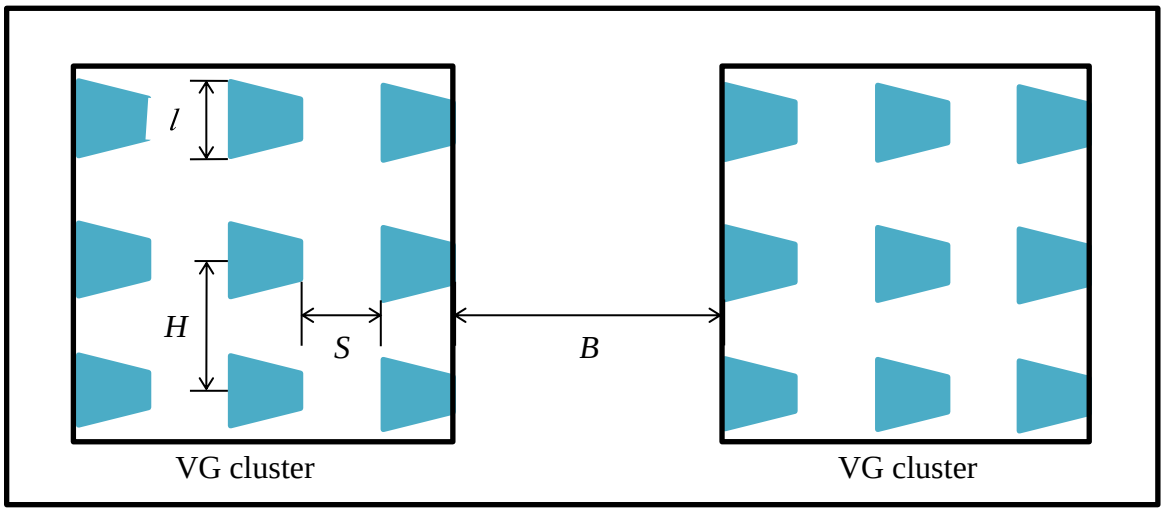

Fig. 63. Heat transfer experiments for clusters of VGs

Figure 64 shows the local heat transfer coefficient ratio (h/h_0 in Eq. 29) for clusters of VGs with a variation of streamwise spacing (B) from 2β to 5β. As shown in Fig. 64, the heat transfer enhancement over most of the heat transfer surface was rather uniform for B of 2β when compared to the other cases. On the other hand, for B greater than 2β, the heat transfer enhancement varied considerably. Furthermore, for B of 5β, spots with enhancement levels less

than 5% could be seen. Therefore, in the present study, B of 2β was considered as an optimal streamwise spacing for clusters of rows of VGs, which suggests that rows should be placed at a fixed streamwise spacing along the axial distance. In summary, optimal configuration factors for multiple rows of VGs were found based on heat transfer experiments as shown in Table 7.

Table 7. Optical configuration factors for multiple rows of VGs

Configuration factor	Optimum value
Spanwise spacing of VGs in a row (STW), Fig. 58	STW = 1.5
Streamwise spacing of rows of VGs (S), Fig. 59	$S = 2\beta$
Arrangement of VGs in a cluster, Fig. 59	Aligned
Streamwise spacing of clusters of VGs (B), Fig. 60	$B = 2\beta$

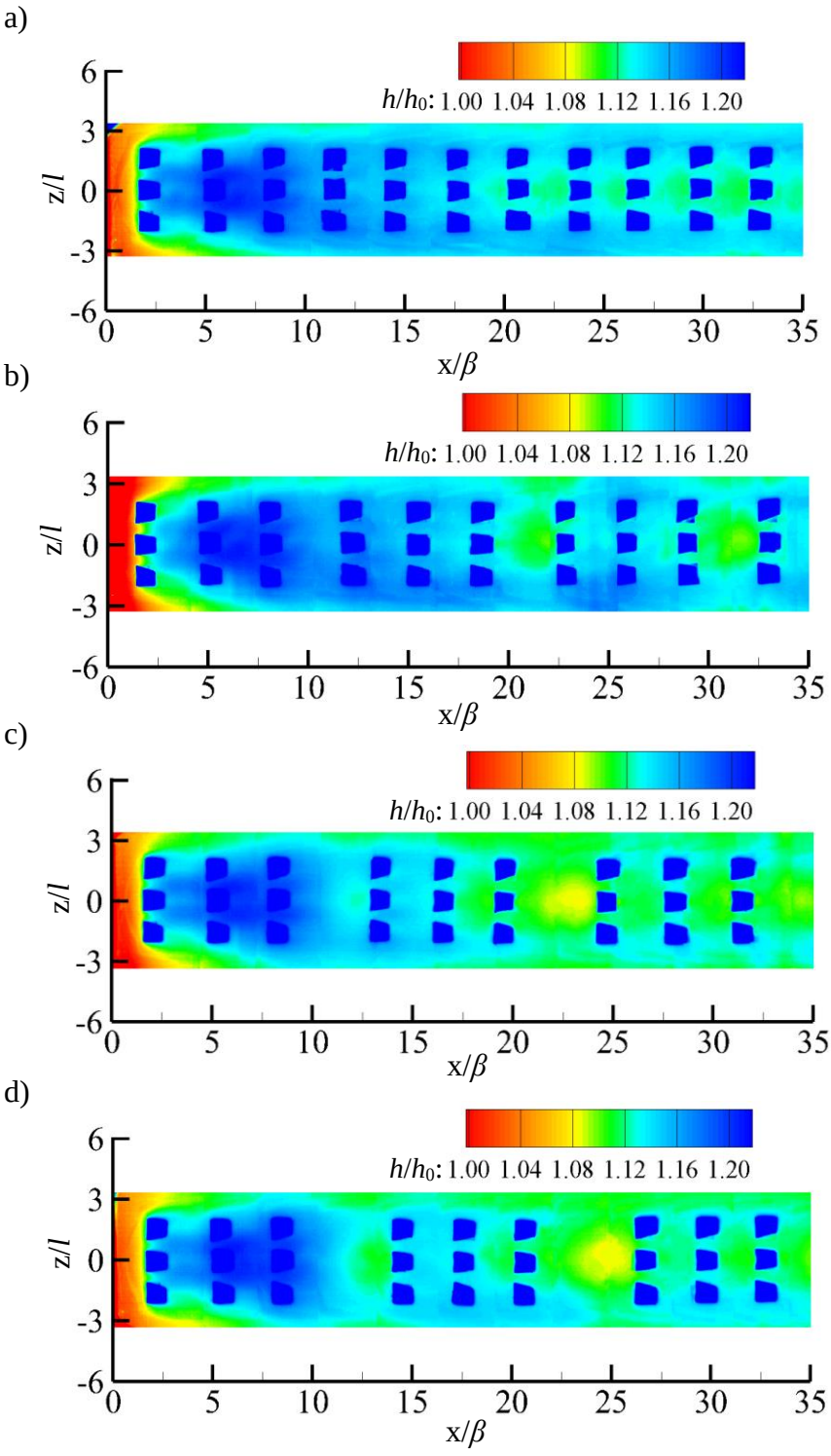

Fig. 64. Contours of the local heat transfer coefficient ratio (h/h_0) for clusters of VGs with streamwise spacing (B) of a) 2β, b) 3β, c) 4β and d) 5β

Other cases were considered by removing the middle VGs from the third row when multiple clusters of VGs were tested. By removing the middle VG, it was hypothesized that the flow might recover some of its coherence, which could in turn lead to better heat transfer. However, by removing the middle VG, heat transfer performance did not improve as seen in Fig. 65. Therefore, removing middle VGs was not considered in the rest of the study.

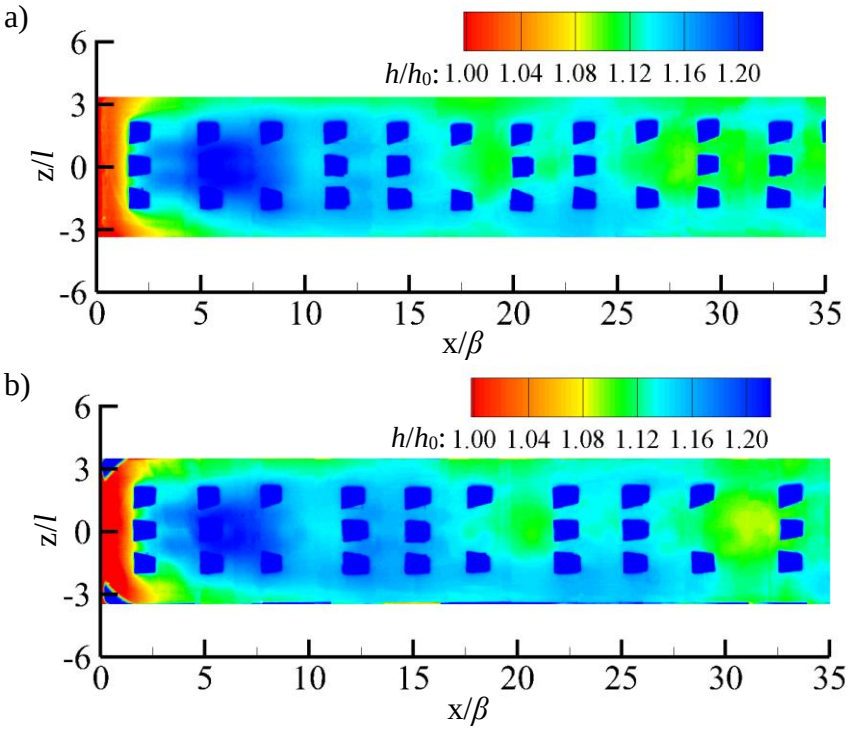

Fig. 65. Contours of the local heat transfer coefficient ratio (h/h_0) for clusters of VGs in the absence of a middle VG in the third row for streamwise cluster spacing (B) of a) 2β, and b) 3β

4.6 Relation Between Wall-Shear Rate and Local Heat Transfer

The convective transport of mass, momentum and heat occurs through a thin boundary layer close to the wall. It has been also found that the modification of local sublayer thickness by the presence of a coherent vortex has significant effects on heat transfer [79-81, 91]. The sublayer thickness is determined by the local skin friction, which is a function of the gradient of

the mean streamwise velocity near the wall (i.e. wall-shear rate) [81, 91]. Therefore, an analysis by using local heat transfer coefficient ratio (h/h_0) and local shear rate ratio ($\lambda = \dot{\gamma}_w/\dot{\gamma}_{w0}$) was conducted to understand the relationship between fluid flow and heat transfer in the near-wall region, where $\dot{\gamma}_w$ is the local wall-shear rate with a VG and $\dot{\gamma}_{w0}$ is the local wall-shear rate without a VG (baseline case). The local wall-shear rates were obtained based on the mean streamwise velocity gradient as follows:

$$\dot{\gamma}_w = \left.\frac{\partial U}{\partial y}\right|_w \tag{30}$$

where $\partial U/\partial y$ is the mean streamwise velocity gradient. The local shear rate $(\dot{\gamma}_w)$ was estimated by linear curve-fitting of the last three velocity data points from the wall obtained from PIV measurements at each streamwise location with a resolution of 24 μm/px [26]. The three data points from the wall were found to fall within $y^+ < 5$.

Figures 66 and 67 show the comparison between the local heat transfer coefficient ratio (h/h_0) and the shear rates ratio (λ) along the axial distance for single VGs, in the common-up flow ($z/l = 0$, center plane) and down flow ($z/l = 0.7$) regions, respectively. Figures 66 and 67 show that the local heat transfer coefficient ratio (h/h_0) had very similar trends as the shear rate ratio (λ) along the axial distance. The fairly good agreement of the trends of h/h_0 and λ along the axial distance suggests that the boundary layer heat transfer mechanism was dominant within the viscous sublayer ($y^+ < 5$) [10, 14, 78].

In the common-up flow regions ($z/l = 0$, center plane) in the vicinity of the VG ($x/\beta <$ ~1), negative shear rates were observed ($\lambda < 0$) in Fig. 66, which correspond to the prevalence of reverse flow in the wake region of the VG. Therefore, this indicates that heat transfer was dominated by the streamwise component of the reverse flow in the viscous sublayer under this condition [79-81]. This is because the transversal velocities decreased and led to the formation of

a dead zone near the wall ($y/\beta < 0.3$) in the middle of the CVP ($-0.2 < z/l < 0.2$), as shown in Fig. 31. As the CVP developed further the downstream ($x/\beta > 1$), the flow in the boundary layer reattached as suggested the positive value of shear rate ratio ($\lambda > 0$).

In the down flow regions ($z/l = 0.7$) seen in Fig. 67, the local heat transfer (h/h_0) was significantly enhanced since the flow near the surface was accelerated in the streamwise direction, as shown in Fig. 35. Therefore, the local shear rate (λ) also increased. Furthermore, the agreement between h/h_0 and λ trends seen in Figs. 66 and 67 also suggest that heat transfer in the wake of single VGs was closely related to the mean velocities of the coherent flow in both common-up flow and common-down flow regions [10, 14, 78]. Lastly, both h/h_0 and λ reached stable levels for $x/\beta > 1.5$ in the common-down flow region as seen in Fig. 67. This behavior can be attributed to a decrease in the magnitudes of the mean velocities for $y/\beta < 0.4$ as seen in Figs. 35 and 36.

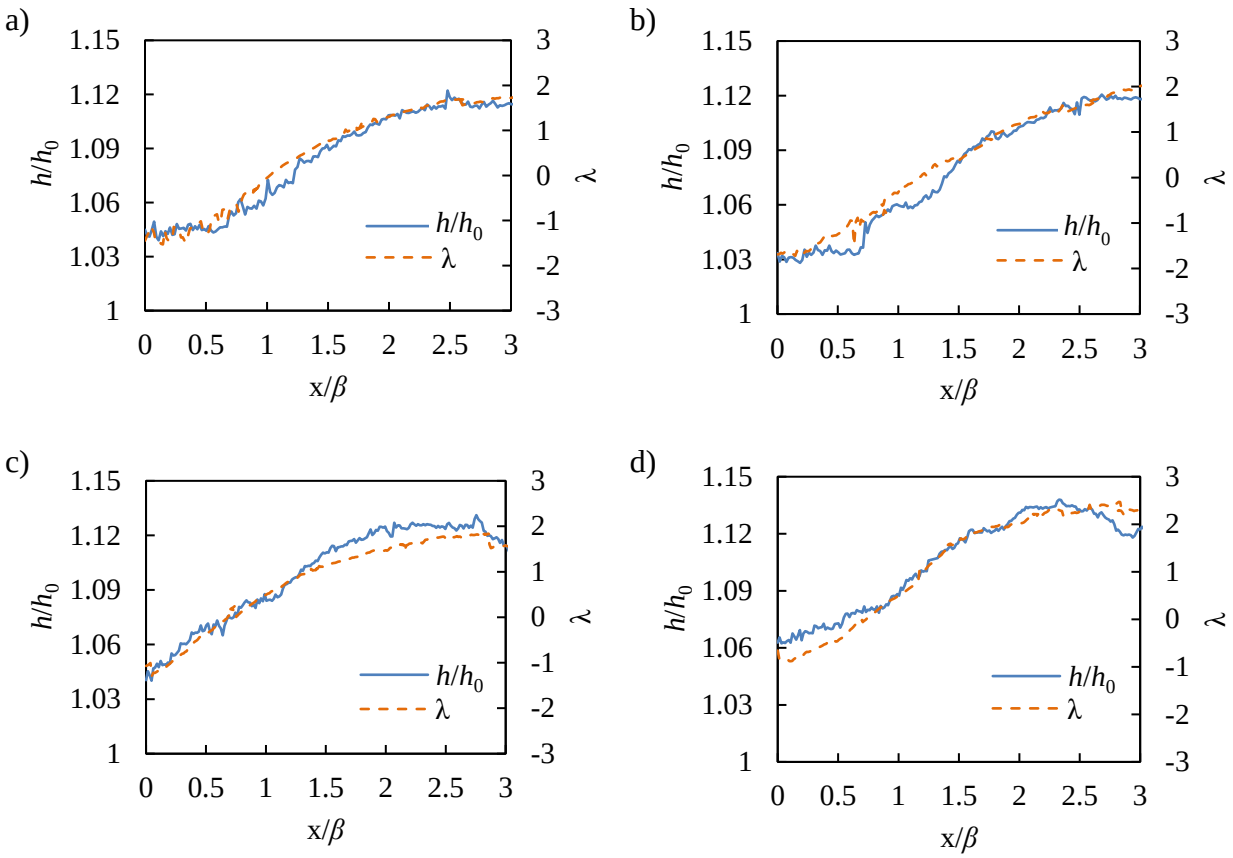

Fig. 66. Local heat transfer coefficient ratio (h/h_0) and local shear rate ratio (λ) along the duct measured in the common-up flow region ($z/l = 0$, center plane) for: a) trapezoidal VG ($\phi = 7.6°$) at $\theta = 45°$, b) rectangular VG ($\phi = 0°$) at $\theta = 45°$, c) trapezoidal VG ($\phi = 7.6°$) at $\theta = 60°$, and d) rectangular VG ($\phi = 0°$) at $\theta = 60°$

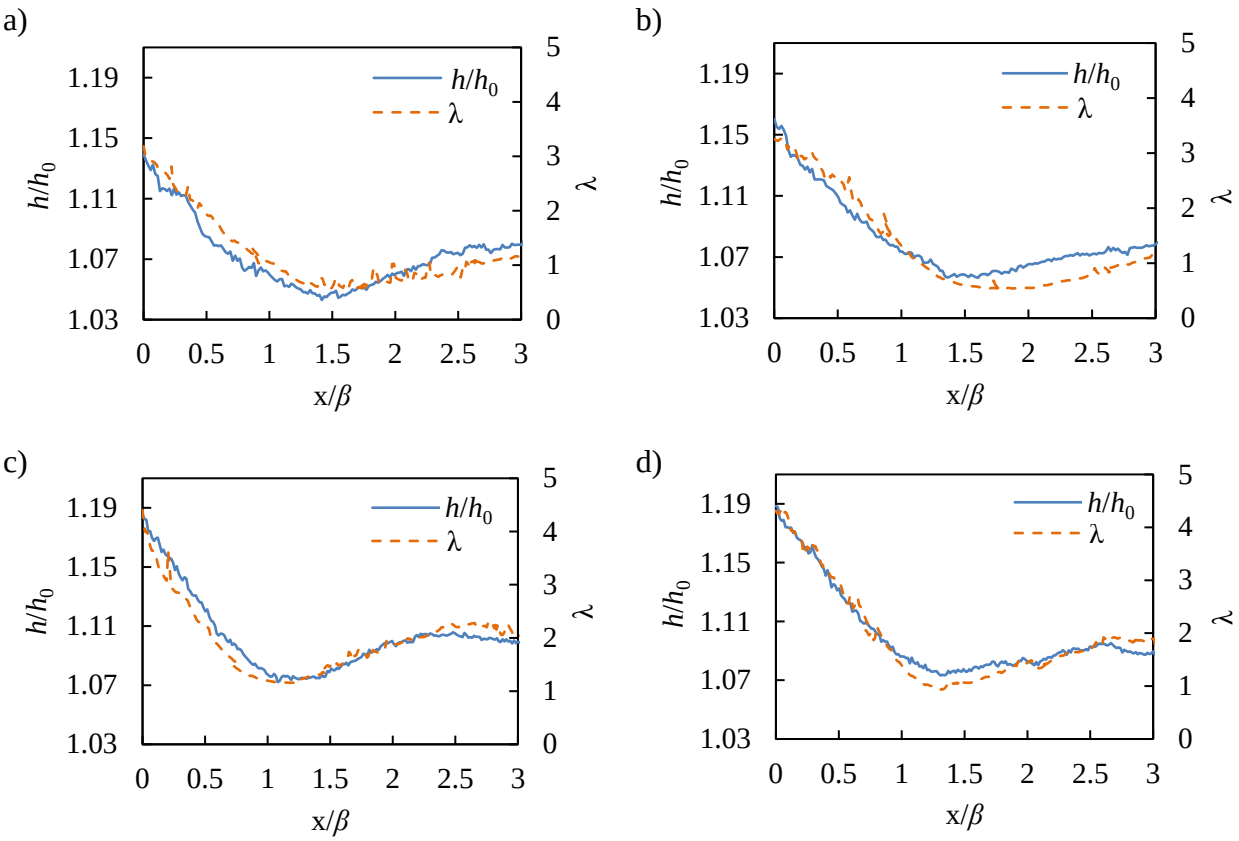

Fig. 67. Local heat transfer coefficient ratio (h/h_0) and local shear rate ratio (λ) along the axial distance measured in the down-flow region ($z/l = 0.7$) for: a) trapezoidal VG ($\phi = 7.6°$) at $\theta = 45°$, b) rectangular VG ($\phi = 0°$) at $\theta = 45°$, c) trapezoidal VG ($\phi = 7.6°$) at $\theta = 60°$, and d) rectangular VG ($\phi = 0°$) at $\theta = 60°$

Figures 68 and 69 show the comparison between the local heat transfer coefficient ratio (h/h_0) and the local shear rate ratio (λ) in the common-up flow and common-down flow regions for a single row of VGs with different STW values. Unlike the single VG cases, Fig. 68 shows that the trends of h/h_0 deviated initially with respect to λ along the axial distance in the common-up flow region, before converging to a single value further downstream. The trends seen in Fig. 68 can be attributed to a greater level of turbulence intensity for x/β less than 1.0, as seen in Fig. 70. Furthermore, at greater levels of turbulence intensity (i.e. greater rms velocities), the effect of mean velocity on heat transfer is not as dominant, which explains the initial divergence in h/h_0

and λ levels in the common up flow region. Westphal *et al.* [21] also found that the turbulence intensity in the upwash region of longitudinal vortices was higher than that in the center or down flow regions. Torri and Yanagihara [14, 78] also found a significant increase in heat transfer where turbulence intensity increased significantly. For the STW = 1.0 case, VGs without any spanwise spacing induced incomplete CVPs and led to substantial decrease in the mean streamwise velocity near the wall ($y/\beta < 1$), as shown in Fig. 40a. As a result, lower heat transfer performance was observed ($h/h_0 < 1.05$), when compared to the other cases.

In Fig. 69, h/h_0 follows λ closely along the axial distance in the common-down flow, except for the STW = 1.0 case, where the incomplete CVPs led to decrease in heat transfer with the low shear rate ratio ($\lambda < 0$). The fairly good agreement between the trends of h/h_0 and λ along the axial distance suggests that the boundary layer heat transfer mechanism was dominant within the viscous sublayer ($y^+ < 5$) even though the neighboring CVPs interacted more strongly with each other as STW decreased [78].

The turbulence statistics were also obtained in the common-down flow region for a single row with STW of 1.5, as shown in Fig, 70. Figure 70 shows the u_{rms}, v_{rms}, and $-\overline{u'v'}$ measured at an axial distance of x/β of 1 away from the trailing edge, respectively. As shown in Fig. 70, lower rms velocities and Reynold stress values can be seen in the common-down flow regions. Therefore, an increase in mean streamwise and vertical velocities near the wall, as shown in Figs. 42 and 43, played a more important role in heat transfer in the common-down flow region than in the common-up flow region.

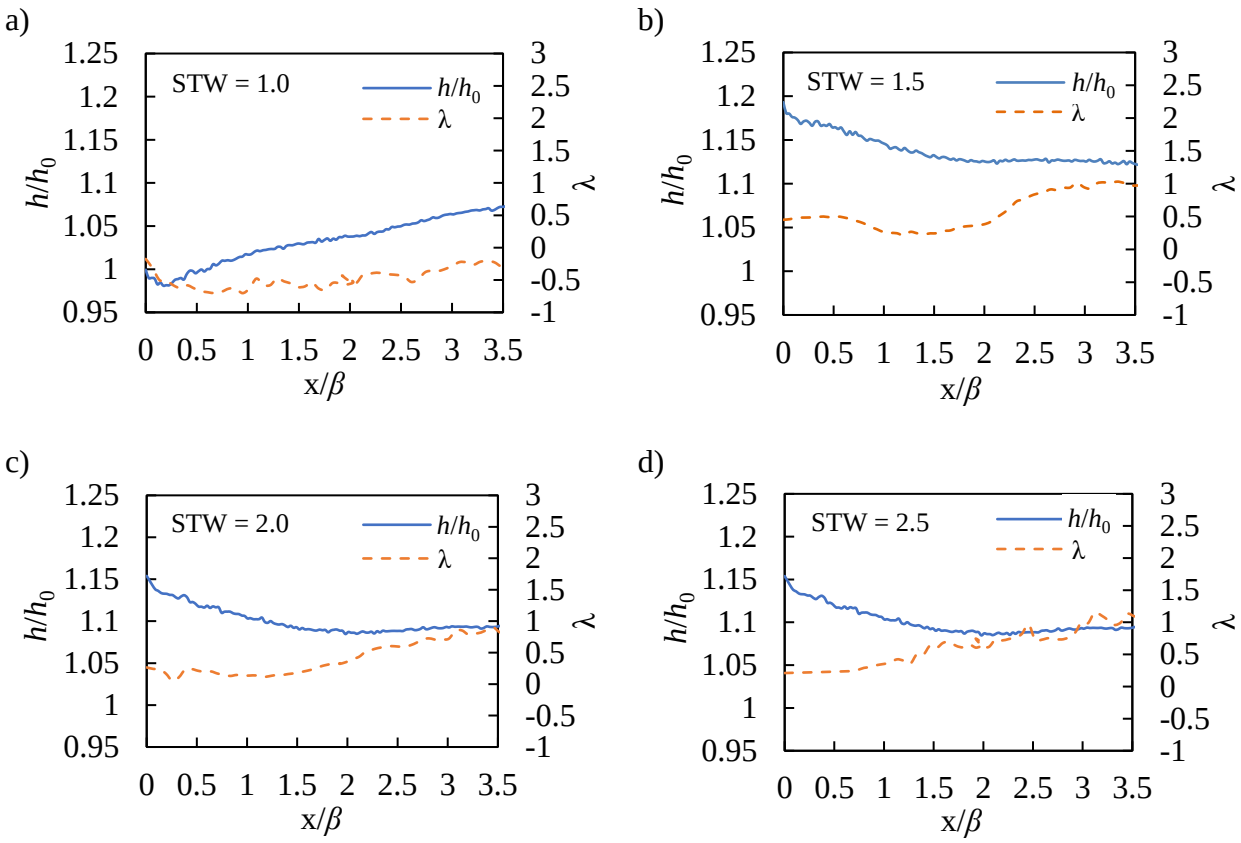

Fig. 68. Local heat transfer coefficient ratio (h/h_0) and local shear rate ratio (λ) along the axial distance measured in the center plane (common-up flow region) for a) STW = 1.0, b) STW = 1.5, c) STW = 2.0, and d) STW = 2.5

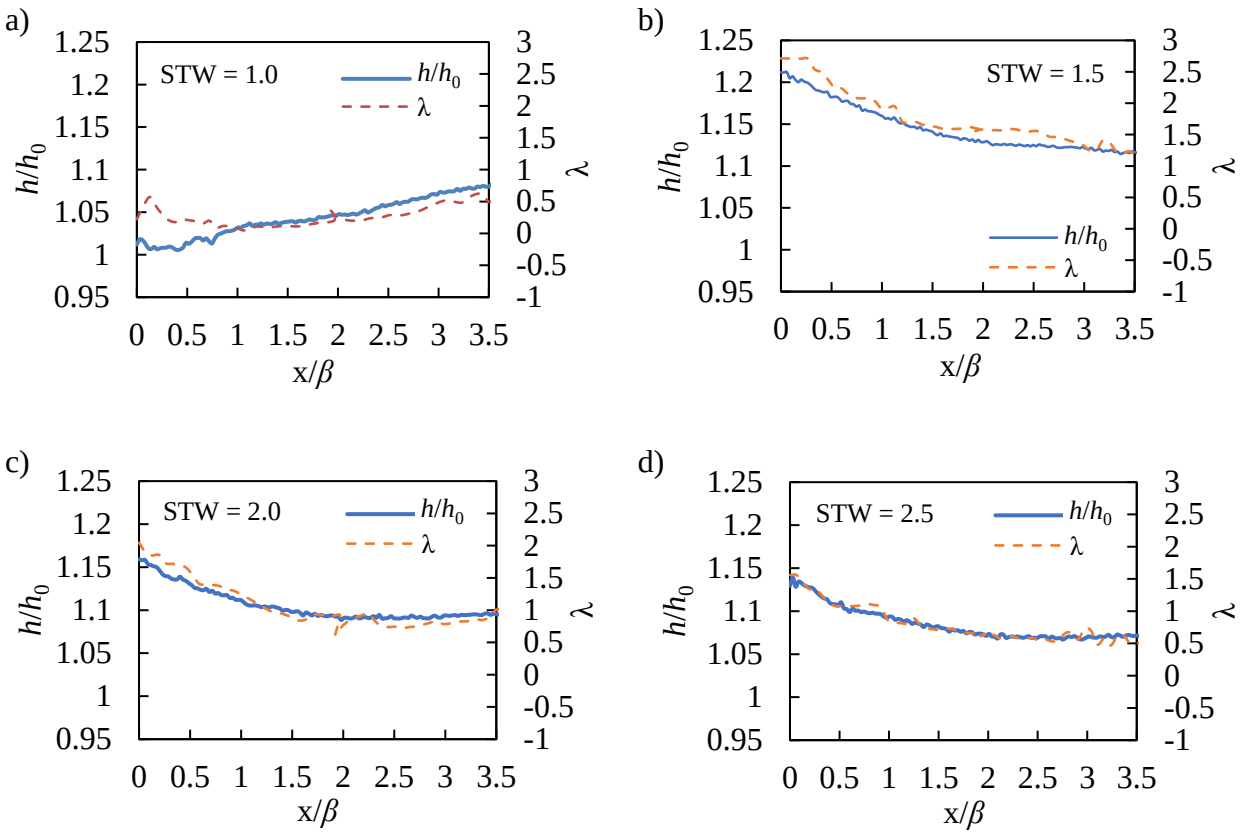

Fig. 69. Local heat transfer coefficient ratio (h/h_0) and local shear rate ratio (λ) along the axial distance measured in the plane in between of the VGs (common-down flow region) for a) STW = 1.0, b) STW = 1.5, c) STW = 2.0, and d) STW = 2.5

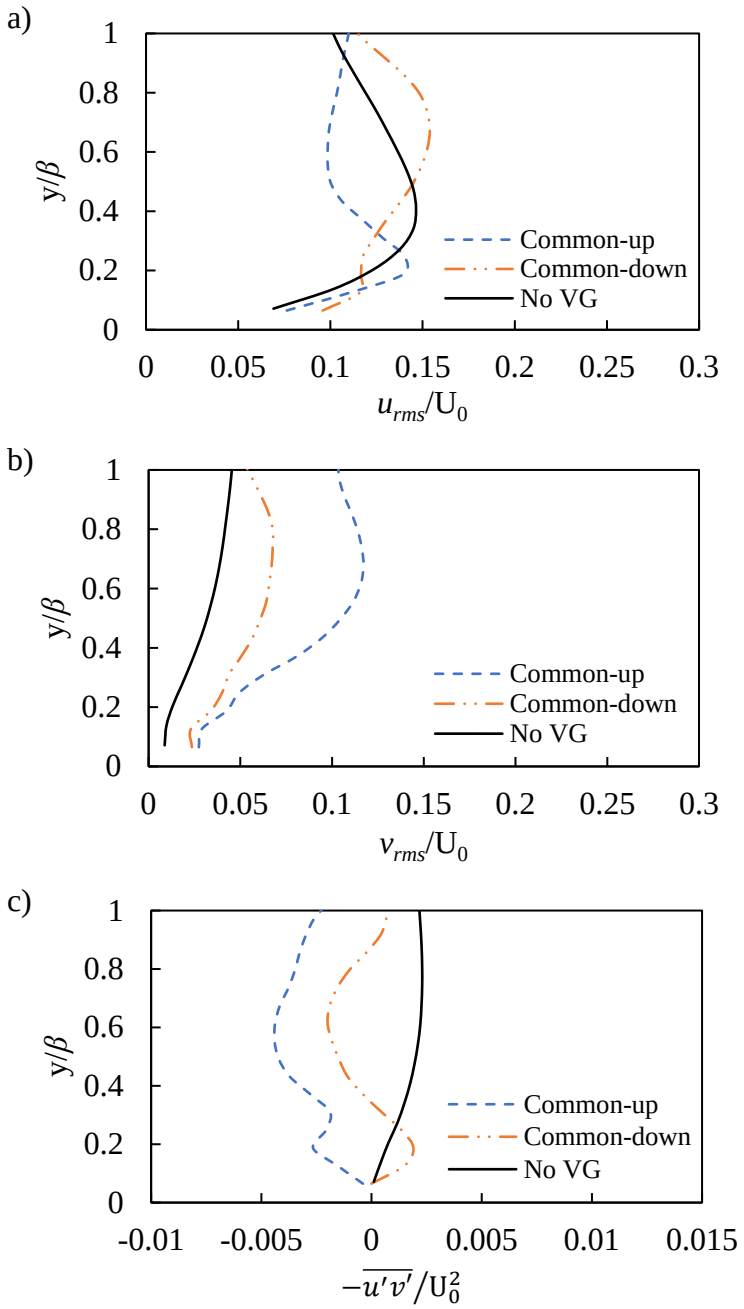

Fig. 70. Root-mean-square of fluctuating components of the a) streamwise and b) vertical velocities, and c) primary Reynolds stress $-\overline{\boldsymbol{u'v'}}$ measured in the common-up flow (z/*l* = 0, center plane) and common-down flow regions (z/*l* = 0.75, a plane in between of VGs) in the wake of single row of VGs for STW of 1.5 at *x*/*β* of 1.0.

CHAPTER V

CONCLUSION AND RECOMMENDATIONS

The primary objective of this study was to gain a better understanding about the coherent flows induced by single and multiple trapezoidal VGs and their effects on heat transfer. To understand the induced vortical flow structures and their effects on heat transfer in the wake of VGs, a series of experiments have been conducted using smoke visualization, high speed optical imaging and IR thermal imaging techniques. Based on the results of this study, the effects of the role of geometrical factors and configurations of the trapezoidal vortex generators (VGs), such as taper angle, inclination angle, spanwise spacing in a single row of VGs, streamwise spacing of multiple rows of VGs, and streamwise spacing of clusters of VGs, on the flow characteristics and surface heat transfer have been elucidated. In this Chapter, the conclusions and recommendations for future study are presented below.

5.1 Conclusions

Based on the experimental results of the current study, it was found that geometric factors and configuration of VGs play significant roles in the flow and heat transfer characteristics. In this subsection, concluding remarks are made for various test conditions, as described below.

Conclusion of single vortex generator study

- The effects of single VGs with different taper angle and inclination angle CVP path, mean velocity, and surface temperature distributions were characterized. Trapezoidal VGs induced counter-rotating vortex pair (CVP) with the common-up flow in between them. As CVP developed along the downstream, the horizontal separation distance of the

vortex cores decreased while the vertical distance from the wall increased. At lower inclination angle, CVP lasted for a longer axial distance of x/β.

- It was found that stronger recirculation flows are generated at the bottom corner of VGs at higher inclination angle. In addition, the transversal velocities of CVP weakened and formed a dead zone near the wall. As a result, low heat transfer performance was observed in the common-up flow region. On the other hand, in the down flow region, the near-wall flows accelerated in the streamwise direction due to the induced vortical structure.
- As inclination angle increased, the flow was accelerated in the streamwise direction and led to an increase in heat transfer. In general, the effect of CVP on the flow acceleration and heat transfer enhancement became insignificant after $x/\beta = 1.5$. The increase of taper angle had lesser effect on the velocity and surface temperature distributions in the wake of single VGs.

Conclusion of single row of vortex generators study

- Particle image velocimetry (PIV) and heat transfer experiments were conducted to understand the role of the spacing-to-width ratio (STW) of three trapezoidal VGs on the induced vortical structures and heat transfer in the wake region at $Re \approx 4800$. It was found that for STW of 2.5, CVPs separated and behaved almost independently of neighboring CVPs. On the other hand, for STW of 1.0, CVPs were not generated completely due to the restricted flow path in between of VGs. As a result, lower heat transfer enhancement was observed.

- Strong downward momentum was generated due to the interaction of CVPs, especially for STW of 1.5. As a result, the vortices remained closer adjacent to the surface along the streamwise direction and the flow was accelerated in the streamwise direction, which also led to enhanced heat transfer. The CVP flow mechanism affected the convective heat transfer process up to $x/\beta = 1.5$ approximately for STW of 1.5.

Conclusion of multiple rows of vortex generators study

- In this study, the effects of rows of trapezoidal VGs on the coherent flow structures were investigated using PIV. Mean velocities, root-mean-square of velocity fluctuations, and Reynolds stresses were measured in the regions after the first row, second row, and third row of VGs in order to understand how the coherent flow structure changed along the rows of VGs. The PIV results were also used to explain the heat transfer characteristics when using multiple rows of VGs.
- Based on turbulence statistics and heat transfer experiments, it was found that the increase in heat transfer was driven by the mean motion in the wake of the first row of VGs. However, the turbulent motion of the flow became a dominant mechanism for heat transfer enhancement in the wake of the second and third rows.
- In the heat transfer experiments of aligned and staggered arrangements of rows of VGs were considered in order to find optimal heat transfer performance. It was found that an aligned arrangement with S of 2β was closer to an optimal configuration, when compared to the other cases. For multiple clusters of VGs, heat transfer results indicate that placing rows of VGs at a fixed spacing lead to optimal heat transfer performance when compared to clusters of VGs separated at streamwise cluster spacing (B) greater than 2β.

Conclusion of relationship of wall shear rate and surface temperature

- An analysis based on local heat transfer coefficient ratio (h/h_0) and local mean shear rate ratio (λ) was conducted to understand the relationship between fluid flow and heat transfer in the near-wall region. For single VGs, the local heat transfer coefficient ratio (h/h_0) follows the local shear rate ratio (λ) closely along the axial distance, suggesting that the heat transfer rates on the surface depend on mean shear ($\partial U/\partial y$) within the viscous sublayer ($y^+ < 5$).
- For a single row of VGs, h/h_0 initially deviated from λ along the axial distance due to increased turbulence intensity in the common-up flow region. However, h/h_0 followed λ closely along the axial distance due to lower levels of turbulence intensity in the common-down flow region. From the PIV results, it is evident that turbulence intensity in relation with mean velocity plays a dominant role in the heat transfer process.

5.2 Recommendations for Future Work

Pressure drop measurement

First of all, pressure drop penalty has to be identified for the suggested configuration of clusters of VGs, as shown in Fig. 61a. The pressure loss in a horizontal straight duct flow should be calculated using the known Darcy-Weisbach equation as follows:

$$\Delta \mathrm{P} = f \frac{L}{D_h} \frac{\rho U^2}{2} \tag{31}$$

where Δp is pressure loss, f is the Darcy friction factor, L length of duct or test section, D_h is hydraulic diameter of the duct, ρ is density of fluid, and U is flow velocity. In the experimental conations of the present study, f was found to be about 0.038 assuming smooth surface condition, L/D_h of 6, density, ρ of 1.18 kg/m^3 and streamwise velocity U of 0.8 m/s. Under those

conditions, an expected pressure loss of 0.09 Pascal without VGs could be obtained in the test section. Therefore, future studies should consider greater velocities to determine the effects of using VGs on pressure drop. Furthermore, heat transfer experiments and PIV analysis should be conducted at increased Reynolds number to analyze the flow structures and heat transfer performance comprehensively.

In addition, pressure drop has to be assessed over a range of flow rates to evaluate effective friction factor (f) of configuration of VGs. This is useful parameter to estimate pressure losses by the VGs with variation in flow conditions.

Air injection from the bottom corner of trapezoidal VGs

For clusters of VGs, better heat transfer performances were observed when streamwise spacing in between of cluster (B) was set at 2β. However, even for the suggested configuration in this study, a decrease in heat transfer was observed when more than 3 rows of VGs were used. Therefore, future studies should consider fluid (air) injection along the axial distance to further enhance heat transfer performance along the downstream. Analogous to film cooling techniques used in turbines, by injecting cool air from the bottom corner of VGs, a significant increase in heat transfer could be obtained in the vicinity of VGs. Furthermore, it has been known that transverse jets can induce CVPs, which could potentially improve heat transfer performance further downstream. For the air injection approach, PIV analysis should be conducted to characterize the flow structures under those conditions. Furthermore, an optimal jet velocity should be found for better heat transfer by using IR thermography. The effects of angle of air injection should be also studied.

REFERENCES

[1] Hewitt, G. F., Shires, G. L. and Bott, T. R. (1994). *Process Heat Transfer CRC Press*, Boca Raton, FL

[2] Jacobi, A. M., & Shah, R. K. (1995). Heat transfer surface enhancement through the use of longitudinal vortices: a review of recent progress. *Experimental Thermal and Fluid Science*, 11(3), 295-309

[3] Reeder, M. F., & Samimy, M. (1996). The evolution of a jet with vortex-generating tabs: real-time visualization and quantitative measurements. *Journal of Fluid Mechanics*, 311, 73-118

[4] Foss, J. K., & Zaman, K. B. M. Q. (1999). Large-and small-scale vortical motions in a shear layer perturbed by tabs. *Journal of Fluid Mechanics*, 382, 307-329

[5] Rahmani, R. K., Keith, T. G., & Ayasoufi, A. (2008). Numerical simulation of turbulent flow in an industrial helical static mixer. *International Journal of Numerical Methods for Heat & Fluid Flow*, 18(6), 675-696

[6] Siddiqui, M. K. (2007). Heat transfer augmentation in a heat exchanger tube using a baffle. *International Journal of Heat and Fluid Flow*, 28(2), 318-328

[7] Hemida, H., Spehr, F., & Krajnović, S. (2008). Local heat transfer enhancement around a matrix of wall-mounted cubes using passive flow control: large-eddy simulations. *International Journal of Heat and Fluid Flow*, 29(5), 1258-1267

[8] Fiebig, M. (1998). Vortices, generators and heat transfer. *Chemical Engineering Research and Design*, 76(2), 108-123

[9] Lin, J. C. (2002). Review of research on low-profile vortex generators to control boundary-layer separation. *Progress in Aerospace Sciences*, 38(4), 389-420

[10] Eibeck, P. A., & Eaton, J. K. (1987). Heat transfer effects of a longitudinal vortex embedded in a turbulent boundary layer. *ASME J. Heat Transfer*, 109(1), 16-24

[11] Turk, A. Y., & Junkhan, G. H. (1984). Heat transfer enhancement downstream of vortex generators on a flat plate (Doctoral dissertation, Iowa State University)

[12] Pearcey H.H., 1961, "Boundary Layer and Flow Control Vol. 2: Shock Induced Separation and Its Prevention by Design and Boundary-Layer Control," Pergamon Press, New York. pp. 1166–1344

[13] Robinson, S. K. (1991). Coherent motions in the turbulent boundary layer. *Annual Review of Fluid Mechanics*, *23*(1), 601-639

[14] Torii, K., & Yanagihara, J. I. (1989). The effects of longitudinal vortices on heat transfer of laminar boundary layers. *JSME international journal. Ser. 2, Fluids engineering, heat transfer, power, combustion, thermophysical properties*, 32(3), 395-402

[15] Jones, J. P. (1957). The Calculation of the Paths of Vortices from a System of Vortex Generators, and a Comparison with Experiment. Tech Rep., C. P. No. 361, Aeronautical Research Council

[16] Habchi, C., Lemenand, T., Valle, D. D., & Peerhossaini, H. (2010). Turbulence behavior of artificially generated vorticity. *Journal of Turbulence*, (11), N36

[17] Lögdberg, O., Fransson, J. H., & Alfredsson, P. H. (2009). Streamwise evolution of longitudinal vortices in a turbulent boundary layer. *Journal of Fluid Mechanics*, 623, 27-58

[18] Park, J., Pagan-Vazquez, A., Alvarado, J. L., Chamorro, L. P., Lux, S. M., & Marsh, C. P. (2017). Characterization of Tab-Induced Counter-Rotating Vortex Pair for Mixing Applications. *Journal of Fluids Engineering*, 139(3), 031102

[19] Park, J., Pagan-Vazquez, A., Alvarado, J. L., Chamorro, L. P., Lux, S., & Marsh, C. (2016). Experimental and Numerical Visualization of Counter Rotating Vortices. *Journal of Heat Transfer*, 138(8), 080908

[20] Pauley, W. R., & Eaton, J. K. (1988). Experimental study of the development of longitudinal vortex pairs embedded in a turbulent boundary layer. *AIAA journal*, 26(7), 816-823

[21] Westphal, R. V., Eaton, J. K., & Pauley, W. R. (2012, December). Interaction between a vortex and a turbulent boundary layer. *In Turbulent Shear Flows 5: Selected Papers from the Fifth International Symposium on Turbulent Shear Flows*, Cornell University, Ithaca, New York, USA, August 7–9, 1985 (p. 266). Springer Science & Business Media

[22] Fiebig, M., Kallweit, P., Mitra, N., & Tiggelbeck, S. (1991). Heat transfer enhancement and drag by longitudinal vortex generators in channel flow. *Experimental Thermal and Fluid Science*, 4(1), 103-114

[23] Tiggelbeck, S., Mitra, N., & Fiebig, M. (1994). Comparison of wing-type vortex generators for heat transfer enhancement in channel flows. *Journal of heat transfer*, 116(4), 880-885

[24] Liou, T. M., Chen, C. C., & Tsai, T. W. (1999, June). Heat transfer and fluid flow in a square duct with 12 different shaped vortex generators. *In ASME 1999 International Gas Turbine and Aeroengine Congress and Exhibition.* pp. V003T01A073-V003T01A073

[25] Elavarasan, R., & Meng, H. (2000). Flow visualization study of role of coherent structures in a tab wake. *Fluid Dynamics Research*, 27(3), 183-197

[26] Yang, W., Meng, H., & Sheng, J. (2001). Dynamics of hairpin vortices generated by a mixing tab in a channel flow. *Experiments in Fluids*, 30(6), 705-722

[27] Dong, S., & Meng, H. U. I. (2004). Flow past a trapezoidal tab. *Journal of Fluid Mechanics*, 510, 219-242

[28] Gretta, W. J., & Smith, C. R. (1993). The flow structure and statistics of a passive mixing tab. *Transactions-American Society of Mechanical Engineers, Journal of Fluid Engineering*, 115, 255-255

[29] Habchi, C., Lemenand, T., Della Valle, D., & Peerhossaini, H. (2010, January). On the correlation between vorticity strength and convective heat transfer. *In 2010 14th International Heat Transfer Conference* (pp. 377-382). American Society of Mechanical Engineers

[30] Hamed, A. M., Pagan-Vazquez, A., Khovalyg, D., Zhang, Z., & Chamorro, L. P. (2017). Vortical structures in the near wake of tabs with various geometries. *Journal of Fluid Mechanics*, 825, 167-188

[32] Yanaoka, H., Inamura, T., & Kawabe, S. (2007). Turbulence and heat transfer of a hairpin vortex formed behind a cube in a laminar boundary layer. Numerical Heat Transfer, Part A: Applications, 52(11), 973-990

[33] Habchi, C., Lemenand, T., Della Valle, D., Al Shaer, A., & Peerhossaini, H. (2015). Experimental study of the turbulent field behind a perforated vortex generator. *Journal of Applied Mechanics and Technical Physics*, *56*(4), 569-579

[34] Shizawa, T., & Eaton, J. K. (1992). Turbulence measurements for a longitudinal vortex interacting with a three-dimensional turbulent boundary layer. *AIAA journal*, 30(1), 49-55

[35] Lemenand, T., Habchi, C., Della Valle, D., & Peerhossaini, H. (2018). Vorticity and convective heat transfer downstream of a vortex generator. *International Journal of Thermal Sciences*, *125*, 342-349

[36] Khanjian, A., Habchi, C., Russeil, S., Bougeard, D., & Lemenand, T. (2018). Effect of the angle of attack of a rectangular wing on the heat transfer enhancement in channel flow at low Reynolds number. *Heat and Mass Transfer*, *54*(5), 1441-1452

[37] Edwards, F. J., Alker, C. J. R., & Crompton, N. (1974). FC6. 4 The improvement of forced convection surface heat transfer using surface protrusions in the form of (A) cubes and (B) vortex generators. *Proceedings of the Fifth International Heat Transfer Conference Tokyo,* 2, 2244–2248

[38] Yanagihara, JurandirItizo, and Kahoru Torii. Heat-transfer augmentation by longitudinal vortices rows. *Experimental Thermal and Fluid Science* 7.2 (1993): 137

[39] Torii, K., Kwak, K. M., & Nishino, K. (2002). Heat transfer enhancement accompanying pressure-loss reduction with winglet-type vortex generators for fin-tube heat exchangers. *International Journal of Heat and Mass Transfer*, 45(18), 3795-3801

[40] Fiebig, M., Valencia, A., & Mitra, N. K. (1993). Wing-type vortex generators for fin-and-tube heat exchangers. *Experimental Thermal and Fluid Science*, 7(4), 287-295

[41] Kaci, H. M., Habchi, C., Lemenand, T., Della Valle, D., & Peerhossaini, H. (2010). Flow structure and heat transfer induced by embedded vorticity. *International Journal of Heat and Mass Transfer*, 53(17), 3575-3584

[42] Habchi, C., Russeil, S., Bougeard, D., Harion, J. L., Lemenand, T., Della Valle, D., & Peerhossaini, H. (2012). Enhancing heat transfer in vortex generator-type multifunctional heat exchangers. *Applied Thermal Engineering*, *38*, 14-25

[43] Dewan, A., Mahanta, P., Raju, K. S., & Kumar, P. S. (2004). Review of passive heat transfer augmentation techniques. *Proceedings of the Institution of Mechanical Engineers, Part A: Journal of Power and Energy*, *218*(7), 509-527

[44] Liu, S., & Sakr, M. (2013). A comprehensive review on passive heat transfer enhancements in pipe exchangers. *Renewable and Sustainable Energy Reviews*, *19*, 64-81

[45] Erbay, L. B., Doğan, B., & Öztürk, M. M. (2017). Comprehensive Study of Heat Exchangers with Louvered Fins. In *Heat Exchangers-Advanced Features and Applications*. InTech

[46] Sheikholeslami, M., Gorji-Bandpy, M., & Ganji, D. D. (2015). Review of heat transfer enhancement methods: Focus on passive methods using swirl flow devices. *Renewable and Sustainable Energy Reviews*, *49*, 444-469

[47] Bell, J. H. & Mehta, R. D. (1989) Design and calibration of the mixing layer wind tunnel. JIAA Rep. TR-89. Dept. of Aeronautics and Astronautics, Stanford University

[48] Merzkirch, W., 1987, "Flow Visualization Second Edition", Orlando: Academic Press. Inc., Print

[49] Lu, L., & Sick, V. (2013). High-speed particle image velocimetry near surfaces. *JoVE (Journal of Visualized Experiments)*, (76), e50559-e50559

[50] Xu, H., & Bodenschatz, E. (2008). Motion of inertial particles with size larger than Kolmogorov scale in turbulent flows. *Physica D: Nonlinear Phenomena*, 237(14), 2095-2100

[51] Thielicke, W., & Stamhuis, E. (2014). PIVlab–towards user-friendly, affordable and accurate digital particle image velocimetry in MATLAB. *Journal of Open Research Software*, 2(1)

[52] Sanchez, T., Chen, D. T., DeCamp, S. J., Heymann, M., & Dogic, Z. (2012). Spontaneous motion in hierarchically assembled active matter. *Nature*, 491(7424), 431-434

[53] Mirsepassi, A., & Rankin, D. D. (2014). Particle image velocimetry in viscoelastic fluids and particle interaction effects. *Experiments in fluids*, 55(1), 1641

[54] Leong, T., Collis, J., Manasseh, R., Ooi, A., Novell, A., Bouakaz, A., & Kentish, S. (2011). The role of surfactant headgroup, chain length, and cavitation microstreaming on the growth of bubbles by rectified diffusion. *The Journal of Physical Chemistry C*, 115(49), 24310-24316

[55] Piro, V., Piro, N., & Piro, O. (2012). Characterization of intraventricular blood flow using a microbubble-contrast tracking echo-piv technique. *Journal of the American College of Cardiology*, 59(13), E1139

[56] McVay, K. L., Park, J. H., Lee, S., Hassan, Y. A., & Anand, N. K. (2015). Preliminary tests of particle image velocimetry for the upper plenum of a scaled model of a very high temperature gas cooled reactor. *Progress in Nuclear Energy*, 83, 305-317

[57] Lazar, E., DeBlauw, B., Glumac, N., Dutton, C., & Elliott, G. (2010, July). A practical approach to PIV uncertainty analysis. *In 27th AIAA Aerodynamic Measurement Technology and Ground Testing Conference* (p. 4355)

[58] Raffel, M., Willert, C. E., Scarano, F., Kähler, C. J., Wereley, S. T., & Kompenhans, J. (2018). Particle image velocimetry: a practical guide. Springer

[59] Kline, S. J., & McClintock, F. A. (1953). Describing Uncertainties in Single-Sample Experiments,*'A SME Mechanical Engineering*, Vol. 75

[60] Benedict, L. H., & Gould, R. D. (1996). Towards better uncertainty estimates for turbulence statistics. *Experiments in fluids*, *22*(2), 129-136

[61] Ghorbani-Tari, Z., Sunden, B., & Tanda, G. (2011, May). On liquid crystal thermography for determination of heat transfer coefficient in rectangular ducts. *In Proc. 15th International Conference on Computational Methods and Experimental Measures* 51, 255-266

[62] Li, S., Ghorbani-Tari, Z., Xie, G., & Sundén, B. (2013). An Experimental and Numerical Study of Flow and Heat Transfer in Ribbed Channels with Large Rib Pitch-to-Height Ratios. *Journal of Enhanced Heat Transfer*, 20(4)

[63] Jeschke, P., Biertümpfel, R., & Beer, H. (2000). Liquid-crystal thermography for heat-transfer measurements in the presence of longitudinal vortices in a natural convection flow. *Measurement Science and Technology*, 11(5), 447

[64] Driggers, R. G. (Ed.). (2003). Encyclopedia of Optical Engineering: Las-Pho, pages 1025-2048 (Vol. 2). CRC press

[65] Kakaç, S., Shah, R. K., & Aung, W. (Eds.). (1987). Handbook of single-phase convective heat transfer (pp. 7-1). New York: Wiley.

[66] Lin, W. L., & Lin, T. F. (1996). Experimental study of unstable mixed convection of air in a bottom heated horizontal rectangular duct. *International journal of heat and mass transfer*, 39(8), 1649-1663

[67] Howell, J. R. (1982). A catalog of radiation configuration factors. McGraw-Hill Book Company

[68] Lorenz, S., Mukomilow, D., & Leiner, W. (1995). Distribution of the heat transfer coefficient in a channel with periodic transverse grooves. *Experimental Thermal and Fluid Science*, 11(3), 234-242

[69] Fischer, F. (2011). Thermoplastics: the best choice for 3D printing. *White Paper, Stratasys Inc., Edn Prairie, MN*

[70] Wu, J. Z, Ma, H. Y, and Zhou, M. D. (2007) Vorticity and Vortex Dynamics. Springer Science & Business Media, New York, NY, 383-446

[71] Currie, I. G. (2003) Fundamental Mechanics of Fluids. Taylor & Fancis Group, Boca Raton, FL, Chap. 2

[72] Bathchelor, G. K. (1967) An Introduction to Fluid Dynamics. Cambridge University Press., New York, NY, 507-588

[73] Gavrilakis, S. (1992). Numerical simulation of low-Reynolds-number turbulent flow through a straight square duct. *Journal of Fluid Mechanics*, 244, 101-129

[74] Niederschulte, M. A., Adrian, R. J., & Hanratty, T. J. (1990). Measurements of turbulent flow in a channel at low Reynolds numbers. *Experiments in Fluids*, *9*(4), 222-230

[75] Robinson, S. K. (1991). Coherent motions in the turbulent boundary layer. *Annual Review of Fluid Mechanics*, *23*(1), 601-639

[76] Blackwelder, R. F., & Kaplan, R. E. (1976). On the wall structure of the turbulent boundary layer. *Journal of Fluid Mechanics*, *76*(1), 89-112

[77] Chang, L. M., Wang, L. B., Song, K. W., Sun, D. L., & Fan, J. F. (2009). Numerical study of the relationship between heat transfer enhancement and absolute vorticity flux along main flow direction in a channel formed by a flat tube bank fin with vortex generators. *International Journal of Heat and Mass Transfer*, *52*(7-8), 1794-1801

[78] Yanagihara, J. I., & Torii, K. (1992). Enhancement of laminar boundary layer heat transfer by a vortex generator. JSME international journal. Ser. 2, *Fluids engineering, heat transfer, power, combustion, thermophysical properties*, 35(3), 400-405

[79] Kestin, J., & Richardson, P. D. (1963). Heat transfer across turbulent, incompressible boundary layers. *International Journal of Heat and Mass Transfer*, *6*(2), 147-189

[80] Nanda, P., Das, S. K., & Martin, H. (2001). Application of a new analogy for predicting heat transfer to cross rod bundle heat exchanger surfaces. *Heat transfer engineering*, *22*(3), 17-25

[81] Eaton, J. K., & Vogel, J. C. (1985). Combined heat transfer and fluid dynamic measurements downstream of a backward-facing step. *ASME J. heat transfer*, 107, 922

[82] Brodkey, R. S. (1995). *The phenomena of fluid motions*. Courier Corporation

[83] Gnielinski, V. (1976). New equations for heat and mass transfer in turbulent pipe and channel flow. *Int. Chem. Eng*., 16(2), 359-368

[84] Gnielinski, V. (1983). Forced convection in ducts. *Heat Exchanger Design Handbook*, 2, 1-2

[85] Suryanarayana, N. V. (1995). Engineering heat transfer. *West Publishing*

[86] Sparrow, E. M., Lloyd, J. R., & Hixon, C. W. (1966). Experiments on Turbulent Heat Transfer in an Asymmetrically Heated Rectangular Duct. *Journal of Heat Transfer*, 88(2), 170-174

[87] Tan, H. M., & Charters, W. W. S. (1970). An experimental investigation of forced-convective heat transfer for fully-developed turbulent flow in a rectangular duct with asymmetric heating. *Solar Energy*, 13(1), 121-125

[88] Barrow, H. (1962). An analytical and experimental study of turbulent gas flow between two smooth parallel walls with unequal heat fluxes. *International Journal of Heat and Mass Transfer*, 5(6), 469-487

[89] Ichimiya, K. (1987). Effects of several roughness elements on an insulated wall for heat transfer from the opposite smooth heated surface in a parallel plate duct. *J. Heat Transfer*., 109(1), 68-73

[90] Kurosaki, Y., & Satoh, I. (1987). Laminar heat transfer in an asymmetrically heated rectangular duct. *International journal of heat and mass transfer*, 30(6), 1201-1208

[91] Eibeck, P. A., & Eaton, J. K. (1985). An experimental investigation of the heat-transfer effects of a longitudinal vortex embedded in a turbulent boundary layer (No. DOE/ER/13081-T1). Stanford Univ., CA (USA), Thermosciences Div.

APPENDIX A

In the present study, the cross-correlation of the PIV recordings was performed using PIVLab. PIVLab is an open source Matlab-base package developed by Thielicke and Stamhuis [51] and is available at their webpage (http://william.thielicke.org/PIVlab/PIVlab.zip). PIVLab includes several subfunctions and a Matlab code for velocity calculation using cross-correlation algorithm is shown below.

```
function [xtable ytable utable vtable typevector] = piv_FFTmulti
(image1,image2,interrogationarea, step, subpixfinder, mask_inpt,
roi_inpt,passes,int2,int3,int4,imdeform)
%profile on
%this funtion performs the  PIV analysis.
warning off %#ok<*WNOFF> %MATLAB:log:logOfZero
if numel(roi_inpt)>0
   xroi=roi_inpt(1);
   yroi=roi_inpt(2);
   widthroi=roi_inpt(3);
   heightroi=roi_inpt(4);
   image1_roi=double(image1(yroi:yroi+heightroi,xroi:xroi+widthroi));
   image2_roi=double(image2(yroi:yroi+heightroi,xroi:xroi+widthroi));
else
   xroi=0;
   yroi=0;
   image1_roi=double(image1);
   image2_roi=double(image2);
end
gen_image1_roi = image1_roi;
gen_image2_roi = image2_roi;

if numel(mask_inpt)>0
   cellmask=mask_inpt;
   mask=zeros(size(image1_roi));
   for i=1:size(cellmask,1);
      masklayerx=cellmask{i,1};
      masklayery=cellmask{i,2};
      mask = mask + poly2mask(masklayerx-xroi,masklayery-
yroi,size(image1_roi,1),size(image1_roi,2)); %kleineres eingangsbild und maske geshiftet
   end
else
```

```
   mask=zeros(size(image1_roi));
end
mask(mask>1)=1;
gen_mask = mask;

miniy=1+(ceil(interrogationarea/2));
minix=1+(ceil(interrogationarea/2));
maxiy=step*(floor(size(image1_roi,1)/step))-(interrogationarea-
1)+(ceil(interrogationarea/2)); %statt size deltax von ROI nehmen
maxix=step*(floor(size(image1_roi,2)/step))-(interrogationarea-1)+(ceil(interrogationarea/2));

numelementsy=floor((maxiy-miniy)/step+1);
numelementsx=floor((maxix-minix)/step+1);

LAy=miniy;
LAx=minix;
LUy=size(image1_roi,1)-maxiy;
LUx=size(image1_roi,2)-maxix;
shift4centery=round((LUy-LAy)/2);
shift4centerx=round((LUx-LAx)/2);
if shift4centery<0 %shift4center will be negative if in the unshifted case the left border is bigger
than the right border. the vectormatrix is hence not centered on the image. the matrix cannot be
shifted more towards the left border because then image2_crop would have a negative index. The
only way to center the matrix would be to remove a column of vectors on the right side. but then
we weould have less data....
   shift4centery=0;
end
if shift4centerx<0 %shift4center will be negative if in the unshifted case the left border is bigger
than the right border. the vectormatrix is hence not centered on the image. the matrix cannot be
shifted more towards the left border because then image2_crop would have a negative index. The
only way to center the matrix would be to remove a column of vectors on the right side. but then
we weould have less data....
   shift4centerx=0;
end
miniy=miniy+shift4centery;
minix=minix+shift4centerx;
maxix=maxix+shift4centerx;
maxiy=maxiy+shift4centery;

image1_roi=padarray(image1_roi,[ceil(interrogationarea/2) ceil(interrogationarea/2)],
min(min(image1_roi)));
image2_roi=padarray(image2_roi,[ceil(interrogationarea/2) ceil(interrogationarea/2)],
min(min(image1_roi)));
mask=padarray(mask,[ceil(interrogationarea/2) ceil(interrogationarea/2)],0);

if (rem(interrogationarea,2) == 0) %for the subpixel displacement measurement
```

```
   SubPixOffset=1;
else
   SubPixOffset=0.5;
end
xtable=zeros(numelementsy,numelementsx);
ytable=xtable;
utable=xtable;
vtable=xtable;
typevector=ones(numelementsy,numelementsx);

%% MAINLOOP
try %check if used from GUI
   handles=guihandles(getappdata(0,'hgui'));
   GUI_avail=1;
catch %#ok<CTCH>
   GUI_avail=0;
end

% divide images by small pictures
% new index for image1_roi and image2_roi
s0 = (repmat((miniy:step:maxiy)'-1, 1,numelementsx) + repmat(((minix:step:maxix)-
1)*size(image1_roi, 1), numelementsy,1))';
s0 = permute(s0(:), [2 3 1]);
s1 = repmat((1:interrogationarea)',1,interrogationarea) + repmat(((1:interrogationarea)-
1)*size(image1_roi, 1),interrogationarea,1);
ss1 = repmat(s1, [1, 1, size(s0,3)])+repmat(s0, [interrogationarea, interrogationarea, 1]);

image1_cut = image1_roi(ss1);
image2_cut = image2_roi(ss1);

%do fft2
result_conv = fftshift(fftshift(real(ifft2(conj(fft2(image1_cut)).*fft2(image2_cut))), 1), 2);
minres = permute(repmat(squeeze(min(min(result_conv))), [1, size(result_conv, 1),
size(result_conv, 2)]), [2 3 1]);
deltares = permute(repmat(squeeze(max(max(result_conv))-min(min(result_conv))),[ 1,
size(result_conv, 1), size(result_conv, 2)]), [2 3 1]);
result_conv = ((result_conv-minres)./deltares)*255;

%apply mask
ii = find(mask(ss1(round(interrogationarea/2+1), round(interrogationarea/2+1), :)));
jj = find(mask((miniy:step:maxiy)+round(interrogationarea/2),
(minix:step:maxix)+round(interrogationarea/2)));
typevector(jj) = 0;
result_conv(:,:, ii) = 0;

[y, x, z] = ind2sub(size(result_conv), find(result_conv==255));
```

```
% we need only one peak from each couple pictures
[z1, zi] = sort(z);
dz1 = [z1(1); diff(z1)];
i0 = find(dz1~=0);
x1 = x(zi(i0));
y1 = y(zi(i0));
z1 = z(zi(i0));

xtable = repmat((minix:step:maxix)+interrogationarea/2, length(miniy:step:maxiy), 1);
ytable = repmat(((miniy:step:maxiy)+interrogationarea/2)', 1, length(minix:step:maxix));

if subpixfinder==1
   [vector] = SUBPIXGAUSS (result_conv,interrogationarea, x1, y1, z1, SubPixOffset);
elseif subpixfinder==2
   [vector] = SUBPIX2DGAUSS (result_conv,interrogationarea, x1, y1, z1, SubPixOffset);
end
vector = permute(reshape(vector, [size(xtable') 2]), [2 1 3]);

utable = vector(:,:,1);
vtable = vector(:,:,2);


%assignin('base','corr_results',corr_results);


%multipass
%feststellen wie viele passes
%wenn intarea=0 dann keinen pass.
for multipass=1:passes-1

   if GUI_avail==1
      set(handles.progress, 'string' , ['Frame progress: ' int2str(j/maxiy*100/passes+((multipass-
1)*(100/passes))) '%' sprintf('\n') 'Validating velocity field']);drawnow;
   else
      fprintf('.');
   end
   %multipass validation, smoothing
   %stdev test
   utable_orig=utable;
   vtable_orig=vtable;
   stdthresh=4;
   meanu=nanmean(nanmean(utable));
   meanv=nanmean(nanmean(vtable));
   std2u=nanstd(reshape(utable,size(utable,1)*size(utable,2),1));
   std2v=nanstd(reshape(vtable,size(vtable,1)*size(vtable,2),1));
```

```
minvalu=meanu-stdthresh*std2u;
maxvalu=meanu+stdthresh*std2u;
minvalv=meanv-stdthresh*std2v;
maxvalv=meanv+stdthresh*std2v;
utable(utable<minvalu)=NaN;
utable(utable>maxvalu)=NaN;
vtable(vtable<minvalv)=NaN;
vtable(vtable>maxvalv)=NaN;

%median test
%info1=[];
epsilon=0.02;
thresh=2;
[J,I]=size(utable);
%medianres=zeros(J,I);
normfluct=zeros(J,I,2);
b=1;
%eps=0.1;
for c=1:2
   if c==1;
      velcomp=utable;
   else
      velcomp=vtable;
   end

   clear neigh
   for ii = -b:b;
      for jj = -b:b;
         neigh(:, :, ii+2*b, jj+2*b)=velcomp((1+b:end-b)+ii, (1+b:end-b)+jj);
      end
   end

   neighcol = reshape(neigh, size(neigh,1), size(neigh,2), (2*b+1)^2);
   neighcol2= neighcol(:,:, [(1:(2*b+1)*b+b) ((2*b+1)*b+b+2:(2*b+1)^2)]);
   neighcol2 = permute(neighcol2, [3, 1, 2]);
   med=median(neighcol2);
   velcomp = velcomp((1+b:end-b), (1+b:end-b));
   fluct=velcomp-permute(med, [2 3 1]);
   res=neighcol2-repmat(med, [(2*b+1)^2-1, 1,1]);
   medianres=permute(median(abs(res)), [2 3 1]);
   normfluct((1+b:end-b), (1+b:end-b), c)=abs(fluct./(medianres+epsilon));
end


info1=(sqrt(normfluct(:,:,1).^2+normfluct(:,:,2).^2)>thresh);
utable(info1==1)=NaN;
```

```
    vtable(info1==1)=NaN;
    %find typevector...
    %maskedpoints=numel(find((typevector)==0));
    %amountnans=numel(find(isnan(utable)==1))-maskedpoints;
    %discarded=amountnans/(size(utable,1)*size(utable,2))*100;
    %disp(['Discarded: ' num2str(amountnans) ' vectors = ' num2str(discarded) ' %'])

    if GUI_avail==1
        if verLessThan('matlab','8.4')
            delete (findobj(getappdata(0,'hgui'),'type', 'hggroup'))
        else
            delete (findobj(getappdata(0,'hgui'),'type', 'quiver'))
        end
        hold on;
        vecscale=str2double(get(handles.vectorscale,'string'));
        %Problem: wenn colorbar an, zï¿½hlt das auch als aexes...
        colorbar('off')
        quiver ((findobj(getappdata(0,'hgui'),'type', 'axes')),xtable(isnan(utable)==0)+xroi-
interrogationarea/2,ytable(isnan(utable)==0)+yroi-
interrogationarea/2,utable_orig(isnan(utable)==0)*vecscale,vtable_orig(isnan(utable)==0)*vecsc
ale,'Color', [0.15 0.7 0.15],'autoscale','off')
        quiver ((findobj(getappdata(0,'hgui'),'type', 'axes')),xtable(isnan(utable)==1)+xroi-
interrogationarea/2,ytable(isnan(utable)==1)+yroi-
interrogationarea/2,utable_orig(isnan(utable)==1)*vecscale,vtable_orig(isnan(utable)==1)*vecsc
ale,'Color',[0.7 0.15 0.15], 'autoscale','off')
        drawnow
        hold off
    end

    %replace nans
    utable=inpaint_nans(utable,4);
    vtable=inpaint_nans(vtable,4);
    %smooth predictor
    try
        if multipass<passes-1
            utable = smoothn(utable,0.6); %stronger smoothing for first passes
            vtable = smoothn(vtable,0.6);
        else
            utable = smoothn(utable); %weaker smoothing for last pass
            vtable = smoothn(vtable);
        end
    catch

        %old matlab versions: gaussian kernel
        h=fspecial('gaussian',5,1);
        utable=imfilter(utable,h,'replicate');
```

```
    vtable=imfilter(vtable,h,'replicate');
  end

  if multipass==1
    interrogationarea=round(int2/2)*2;
  end
  if multipass==2
    interrogationarea=round(int3/2)*2;
  end
  if multipass==3
    interrogationarea=round(int4/2)*2;
  end
  step=interrogationarea/2;

  %bildkoordinaten neu errechnen:
  %roi=[];

  image1_roi = gen_image1_roi;
  image2_roi = gen_image2_roi;
  mask = gen_mask;


  miniy=1+(ceil(interrogationarea/2));
  minix=1+(ceil(interrogationarea/2));
  maxiy=step*(floor(size(image1_roi,1)/step))-(interrogationarea-
1)+(ceil(interrogationarea/2)); %statt size deltax von ROI nehmen
  maxix=step*(floor(size(image1_roi,2)/step))-(interrogationarea-1)+(ceil(interrogationarea/2));

  numelementsy=floor((maxiy-miniy)/step+1);
  numelementsx=floor((maxix-minix)/step+1);

  LAy=miniy;
  LAx=minix;
  LUy=size(image1_roi,1)-maxiy;
  LUx=size(image1_roi,2)-maxix;
  shift4centery=round((LUy-LAy)/2);
  shift4centerx=round((LUx-LAx)/2);
  if shift4centery<0 %shift4center will be negative if in the unshifted case the left border is
bigger than the right border. the vectormatrix is hence not centered on the image. the matrix
cannot be shifted more towards the left border because then image2_crop would have a negative
index. The only way to center the matrix would be to remove a column of vectors on the right
side. but then we weould have less data....
    shift4centery=0;
  end
  if shift4centerx<0 %shift4center will be negative if in the unshifted case the left border is
bigger than the right border. the vectormatrix is hence not centered on the image. the matrix
```

```
cannot be shifted more towards the left border because then image2_crop would have a negative
index. The only way to center the matrix would be to remove a column of vectors on the right
side. but then we weould have less data....
        shift4centerx=0;
    end
    miniy=miniy+shift4centery;
    minix=minix+shift4centerx;
    maxix=maxix+shift4centerx;
    maxiy=maxiy+shift4centery;

    image1_roi=padarray(image1_roi,[ceil(interrogationarea/2) ceil(interrogationarea/2)],
min(min(image1_roi)));
    image2_roi=padarray(image2_roi,[ceil(interrogationarea/2) ceil(interrogationarea/2)],
min(min(image1_roi)));
    mask=padarray(mask,[ceil(interrogationarea/2) ceil(interrogationarea/2)],0);
    if (rem(interrogationarea,2) == 0) %for the subpixel displacement measurement
        SubPixOffset=1;
    else
        SubPixOffset=0.5;
    end

    xtable_old=xtable;
    ytable_old=ytable;
    typevector=ones(numelementsy,numelementsx);
    xtable = repmat((minix:step:maxix), numelementsy, 1) + interrogationarea/2;
    ytable = repmat((miniy:step:maxiy)', 1, numelementsx) + interrogationarea/2;

    %xtable alt und neu geben koordinaten wo die vektoren herkommen.
    %d.h. u und v auf die gewï¿½nschte grï¿½ï¿½e bringen+interpolieren
    if GUI_avail==1
        set(handles.progress, 'string' , ['Frame progress: ' int2str(j/maxiy*100/passes+((multipass-
1)*(100/passes))) '%' sprintf('\n') 'Interpolating velocity field']);drawnow;
        %set(handles.progress, 'string' , 'Interpolating velocity field');drawnow;
    else
        fprintf('.');
    end

    utable=interp2(xtable_old,ytable_old,utable,xtable,ytable,'*spline');
    vtable=interp2(xtable_old,ytable_old,vtable,xtable,ytable,'*spline');

    utable_1= padarray(utable, [1,1], 'replicate');
    vtable_1= padarray(vtable, [1,1], 'replicate');

    %add 1 line around image for border regions... linear extrap

    firstlinex=xtable(1,:);
```

```
    firstlinex_intp=interp1(1:1:size(firstlinex,2),firstlinex,0:1:size(firstlinex,2)+1,'linear','extrap');
    xtable_1=repmat(firstlinex_intp,size(xtable,1)+2,1);

    firstliney=ytable(:,1);
    firstliney_intp=interp1(1:1:size(firstliney,1),firstliney,0:1:size(firstliney,1)+1,'linear','extrap')';
    ytable_1=repmat(firstliney_intp,1,size(ytable,2)+2);

    X=xtable_1; %original locations of vectors in whole image
    Y=ytable_1;
    U=utable_1; %interesting portion of u
    V=vtable_1; % "" of v

    X1=X(1,1):1:X(1,end)-1;
    Y1=(Y(1,1):1:Y(end,1)-1)';
    X1=repmat(X1,size(Y1, 1),1);
    Y1=repmat(Y1,1,size(X1, 2));

    U1 = interp2(X,Y,U,X1,Y1,'*linear');
    V1 = interp2(X,Y,V,X1,Y1,'*linear');

    image2_crop_i1 =
interp2(1:size(image2_roi,2),(1:size(image2_roi,1))',double(image2_roi),X1+U1,Y1+V1,imdefor
m); %linear is 3x faster and looks ok...

    xb = find(X1(1,:) == xtable_1(1,1));
    yb = find(Y1(:,1) == ytable_1(1,1));

    % divide images by small pictures
    % new index for image1_roi
    s0 = (repmat((miniy:step:maxiy)'-1, 1,numelementsx) + repmat(((minix:step:maxix)-
1)*size(image1_roi, 1), numelementsy,1))';
    s0 = permute(s0(:), [2 3 1]);
    s1 = repmat((1:interrogationarea)',1,interrogationarea) + repmat(((1:interrogationarea)-
1)*size(image1_roi, 1),interrogationarea,1);
    ss1 = repmat(s1, [1, 1, size(s0,3)]) + repmat(s0, [interrogationarea, interrogationarea, 1]);
    % new index for image2_crop_i1
    s0 = (repmat(yb-step+step*(1:numelementsy)'-1, 1,numelementsx) + repmat((xb-
step+step*(1:numelementsx)-1)*size(image2_crop_i1, 1), numelementsy,1))';
    s0 = permute(s0(:), [2 3 1]) - s0(1);
    s2 = repmat((1:2*step)',1,2*step) + repmat(((1:2*step)-1)*size(image2_crop_i1, 1),2*step,1);
    ss2 = repmat(s2, [1, 1, size(s0,3)]) + repmat(s0, [interrogationarea, interrogationarea, 1]);

    image1_cut = image1_roi(ss1);
    image2_cut = image2_crop_i1(ss2);

    %do fft2
```

```
    result_conv = fftshift(fftshift(real(ifft2(conj(fft2(image1_cut)).*fft2(image2_cut))), 1), 2);
    minres = permute(repmat(squeeze(min(min(result_conv))), [1, size(result_conv, 1),
size(result_conv, 2)]), [2 3 1]);
    deltares = permute(repmat(squeeze(max(max(result_conv))-min(min(result_conv))), [1,
size(result_conv, 1), size(result_conv, 2)]), [2 3 1]);
    result_conv = ((result_conv-minres)./deltares)*255;

    %apply mask
    ii = find(mask(ss1(round(interrogationarea/2+1), round(interrogationarea/2+1), :)));
    jj = find(mask((miniy:step:maxiy)+round(interrogationarea/2),
(minix:step:maxix)+round(interrogationarea/2)));
    typevector(jj) = 0;
    result_conv(:,:, ii) = 0;

    [y, x, z] = ind2sub(size(result_conv), find(result_conv==255));
    [z1, zi] = sort(z);
    % we need only one peak from each couple pictures
    dz1 = [z1(1); diff(z1)];
    i0 = find(dz1~=0);
    x1 = x(zi(i0));
    y1 = y(zi(i0));
    z1 = z(zi(i0));

    %new xtable and ytable
    xtable = repmat((minix:step:maxix)+interrogationarea/2, length(miniy:step:maxiy), 1);
    ytable = repmat(((miniy:step:maxiy)+interrogationarea/2)', 1, length(minix:step:maxix));

    if subpixfinder==1
       [vector] = SUBPIXGAUSS (result_conv,interrogationarea, x1, y1, z1,SubPixOffset);
    elseif subpixfinder==2
       [vector] = SUBPIX2DGAUSS (result_conv,interrogationarea, x1, y1, z1,SubPixOffset);
    end
    vector = permute(reshape(vector, [size(xtable') 2]), [2 1 3]);

    utable = utable+vector(:,:,1);
    vtable = vtable+vector(:,:,2);

end

%assignin('base','pass_result',pass_result);
%_____________________________________________________________________


xtable=xtable-ceil(interrogationarea/2);
ytable=ytable-ceil(interrogationarea/2);
```

```
xtable=xtable+xroi;
ytable=ytable+yroi;


%profile viewer
%p = profile('info');
%profsave(p,'profile_results')

function [vector] = SUBPIXGAUSS(result_conv, interrogationarea, x, y, z, SubPixOffset)
xi = find(~((x <= (size(result_conv,2)-1)) & (y <= (size(result_conv,1)-1)) & (x >= 2) & (y >=
2)));
x(xi) = [];
y(xi) = [];
z(xi) = [];
xmax = size(result_conv, 2);
vector = NaN(size(result_conv,3), 2);
if(numel(x)~=0)
   ip = sub2ind(size(result_conv), y, x, z);
   %the following 8 lines are copyright (c) 1998, Uri Shavit, Roi Gurka, Alex Liberzon,
Technion ï¿?Israel Institute of Technology
   %http://urapiv.wordpress.com
   f0 = log(result_conv(ip));
   f1 = log(result_conv(ip-1));
   f2 = log(result_conv(ip+1));
   peaky = y + (f1-f2)./(2*f1-4*f0+2*f2);
   f0 = log(result_conv(ip));
   f1 = log(result_conv(ip-xmax));
   f2 = log(result_conv(ip+xmax));
   peakx = x + (f1-f2)./(2*f1-4*f0+2*f2);

   SubpixelX=peakx-(interrogationarea/2)-SubPixOffset;
   SubpixelY=peaky-(interrogationarea/2)-SubPixOffset;
   vector(z, :) = [SubpixelX, SubpixelY];
end

function [vector] = SUBPIX2DGAUSS(result_conv, interrogationarea, x, y, z, SubPixOffset)
xi = find(~((x <= (size(result_conv,2)-1)) & (y <= (size(result_conv,1)-1)) & (x >= 2) & (y >=
2)));
x(xi) = [];
y(xi) = [];
z(xi) = [];
xmax = size(result_conv, 2);
vector = NaN(size(result_conv,3), 2);
if(numel(x)~=0)
   c10 = zeros(3,3, length(z));
   c01 = c10;
```

```
    c11 = c10;
    c20 = c10;
    c02 = c10;
    ip = sub2ind(size(result_conv), y, x, z);

    for i = -1:1
        for j = -1:1
            %following 15 lines based on
            %H. Nobach ï¿?M. Honkanen (2005)
            %Two-dimensional Gaussian regression for sub-pixel displacement
            %estimation in particle image velocimetry or particle position
            %estimation in particle tracking velocimetry
            %Experiments in Fluids (2005) 38: 511ï¿?15
            c10(j+2,i+2, :) = i*log(result_conv(ip+xmax*i+j));
            c01(j+2,i+2, :) = j*log(result_conv(ip+xmax*i+j));
            c11(j+2,i+2, :) = i*j*log(result_conv(ip+xmax*i+j));
            c20(j+2,i+2, :) = (3*i^2-2)*log(result_conv(ip+xmax*i+j));
            c02(j+2,i+2, :) = (3*j^2-2)*log(result_conv(ip+xmax*i+j));
            %c00(j+2,i+2)=(5-3*i^2-3*j^2)*log(result_conv_norm(maxY+j, maxX+i));
        end
    end
    c10 = (1/6)*sum(sum(c10));
    c01 = (1/6)*sum(sum(c01));
    c11 = (1/4)*sum(sum(c11));
    c20 = (1/6)*sum(sum(c20));
    c02 = (1/6)*sum(sum(c02));
    %c00=(1/9)*sum(sum(c00));

    deltax = squeeze((c11.*c01-2*c10.*c02)./(4*c20.*c02-c11.^2));
    deltay = squeeze((c11.*c10-2*c01.*c20)./(4*c20.*c02-c11.^2));
    peakx = x+deltax;
    peaky = y+deltay;

    SubpixelX = peakx-(interrogationarea/2)-SubPixOffset;
    SubpixelY = peaky-(interrogationarea/2)-SubPixOffset;

    vector(z, :) = [SubpixelX, SubpixelY];
end
```